Dynamics of bright solitons in Bose–Einstein condensates: investigations of soliton behaviour in the vector Gross–Pitaevskii equation and applications to enhanced matter-wave interferometry

CALLUM LEWIS GRIMSHAW

Dynamics of bright solitons in Bose–Einstein condensates: investigations of soliton behaviour in the vector Gross–Pitaevskii equation and applications to enhanced matter-wave interferometry

Callum Grimshaw

Abstract

Bright solitons in a quasi-1D Bose–Einstein condensate can be used to enhance precision in matter-wave interferometry, due to their inherent robustness and support against dispersion. Such a soliton interferometer typically relies on a potential barrier used to split a single soliton into two smaller coherent solitons which can then be recombined on the same barrier. In this thesis we examine two extensions to this scheme. Firstly, we investigate a binary BEC system consisting of two bright solitons which are coupled through a mutual nonlinear interaction term. We derive a set of conditions under which the two components can be separated on a potential barrier and use numerical simulations to probe the regimes beyond which this mathematical treatment is applicable. We then use the numerical simulations to look at the effect of the nonlinear coupling on the dynamics of the binary solitons interacting with the barrier. We also look at the interference behaviour found by doubling the simulation time in either a ring trap or a harmonic trapping potential (to ensure recombination on the barrier); as well as the case where the solitons start spatially separated on either side of the barrier in order to find conditions under which the solitons will combine on the barrier. We find a good agreement between the analytical predictions and the results of simulations. Beyond the regions of parameter space where the predictions are expected to hold, we find complex transmission and interference behaviour as a result of nonlinear effects. The second part of this thesis consists of an examination of the prospect of using a subwavelength barrier scheme in a soliton interferometry experiment. This involves using two resonant coupling beams in a Λ-system with a spatially varying intensity. Under certain conditions, this can be used to form an effective potential barrier with a width which is not diffraction-limited. We look at suitable parameter regimes for such a barrier to split and recombine solitons in an interferometer and probe the effects of possible complications such as misalignment in the beams and different scattering lengths in the different states. We simulate the soliton interferometer using the full three component GPE as well as the single component analogue with the effective potential in order to characterise the soliton behaviour and the dependence of the interferometer sensitivity on the system parameters. We find a trend towards an idealised soliton interferometer with a decreasing value of the parameter, w, controlling the barrier characteristics. Also, we demonstrate an agreement between the relevant three component GPE and the analogous single component GPE, in the limit of strong coupling fields.

Dynamics of bright solitons in Bose–Einstein condensates: investigations of soliton behaviour in the vector Gross–Pitaevskii equation and applications to enhanced matter-wave interferometry

Callum Grimshaw

A thesis submitted in partial fulfilment
of the requirements for the degree of
Doctor of Philosophy

Department of Physics
Durham University

August 2021

Contents

List of Figures

List of Tables

Commonly Used Abbreviations

BEC - Bose–Einstein condensate
GPE - Gross–Pitaevskii equation
(O)DLRO - (off-)diagonal long-range order
BCS - Bardeen–Cooper–Schrieffer
FFT - fast Fourier transform
FSSM - Fourier split-step method

Declaration

I confirm that no part of the material offered has previously been submitted by myself for a degree in this or any other University. Where material has been generated through joint work, the work of others has been indicated.

Callum Grimshaw

Durham, August 2021

Acknowledgements

Firstly, I would like to thank my supervisor, Simon Gardiner, for his guidance throughout my postgraduate studies in Durham.

Thanks to Nick Spong for his assistance with technology during my first year in Ph140 and also Ben Beswick on the occasional trip into the office. Thanks to Sofia Ribeiro for company and guidance in the Ph332 office.

Furthermore, I would like to thank the social side of the Quantum Light and Matter/Atomic and Molecular Physics (QLM/AtMol) group. Tom Cutler for his commitment to organising the many (digital) Friday evening seminars, Clare Higgins for organising running outings on Thursday afternoons as well as Will Hamlyn, Joschka Roffe and Liam Gallagher for company on various cycling trips (as well as Jack Segal). I would also like to thank Ifan Hughes for sharing his wisdom on many a Friday evening; as well as Vincent Brooks, Lucy Downes and Jake Blackmore.

Many thanks to my friend in astronomy, Atreya Acharyya, for the support throughout my eight (or seven) years at Durham. I wish him luck in his further endeavours. Lastly, I would like to thank my parents for their support throughout my education.

To my family for their support and encouragement.

Chapter 1

Introduction

1.1 Matter-wave interferometry

Interferometry has for a long time been a powerful technique for measurement as a means to better understand the physical world. It consists of a range of techniques relying on wave interference which can be used to provide a route to extremely high precision measurements required at the forefront of modern physics. Well-known examples include: LIGO (Laser Interferometer Gravitational wave Observatory) which combines long, high finesse cavities with interferometry to enable the experimental precision necessary to observe the perturbations of space resulting from the passage of gravitational waves; and the use of long baseline radio interferometry, which utilies well separated detectors to increase the signal to noise ratio, to detect distant cosmic objects. Fundamentally, an interferometer uses the interference property of waves in order to extract information. We can further classify interferometers by the specific scheme and type of waves used. Interferometers which rely on the wave properties of matter are known as matter-wave interferometers.

The initial appeal of matter-wave interferometers relates directly to what they have that light does not, namely, mass. This allows them to be used in order to probe fundamental physics such as the equivalence principle, the nature of antimatter and the precision measurement of fundamental constants (both to constrain and to attempt to disprove theories in accordance with the scientific method) [1]. The mass property also contributes to slower speeds which

can offer advantages. Molecules up to the size of biologically active molecules (polypeptide consisting of 15 amino acid linear chain) can undergo matter-wave interferometry which can be used in order to probe the interface between quantum and classical descriptions of nature as well as the interface between scientific domains [2].

When bosonic matter is cooled to below a certain critical temperature, a significant proportion of the indistinguishable constituent particles inhabit the lowest available quantum state. This state is known as the Bose–Einstein condensate (BEC) and has potential uses for precision measurement in inertial sensing as well as probes of the gravitational interaction. The advantage offered by the BEC state arises from the occupation of a single quantum state by many massive particles, their long coherence times and their high momentum-space density. Massive waves offer an advantage of lowering the uncertainty relative to the measurement - analogous to the early measurements conducted to measure the magnitude of the gravitational force first using the mountain *Schiehallion* (known to be isolated from other mountains and fairly spatially uniform) and then using the apparatus operated by Henry Cavendish and devised by John Michell using heavy spheres and a torsion balance.

The first BECs formed in the laboratory consisted of dilute alkali metal atomic gases with a quantum state defined by the hyperfine coupling between the outermost electron angular momentum and the nuclear spin. The attraction of these atomic BECs for interferometry is the amount of control offered by interactions between atoms and laser light. This control is utilised in the formation of optical potential traps and barriers and is also employed in the laser cooling used to form the BEC. Another reason is the ability to tune the interatomic interaction direction and magnitude using Feshbach resonances. Many different species can be condensed offering variability in the mass and polarisability as well as different sizes of magnetic moment. Condensed species with large magnetic moments give the possibility of BECs where the dipolar interactions become important [3], such as is the case for chromium [4] and dysprosium [5].

For the above reasons, the atomic BECs are widely employed as quantum simulators and in searches for and demonstrations of novel physical concepts such as topological defects, vortex dynamics and pattern formation [6]. Furthermore, the dilute atomic gases are commonly used in experiments on exotic

quantum states of matter such as ultracold molecule formation [7, 8] as well as the BEC–BCS crossover [9] and the unitary Fermi gas [10].

1.2 Soliton-based matter-wave interferometry

When considering interferometry with matter, a complication is the effect of interactions on the system. The collisions of many atoms impart a phase coherence loss and thus a limit on the interrogation time of the interferometer. For dilute atomic BECs in the low energy limit, the interaction term manifests as a nonlinear wave term with the direction and magnitude determined by the atomic mass and the s-wave scattering length. Using the powerful experimental technique of the Feshbach resonance, the s-wave scattering length can be manipulated to a point where it has a negligible effect. An alternative is to adjust the nonlinear term so that a soliton interferometer can be formed. If the interaction term represents an attractive force (leading to a self-focussing effect) then this can be used to reinforce the wavepacket against dispersion and form a bright soliton. The soliton, by definition, travels as a permanent waveform and is long-lived and so gives the benefit of increasing the phase accumulation time.

Therefore, solitons can offer advantages to atomic interferometry. In order to construct a soliton interferometer, one needs to be able to form solitons in a BEC and then from this generate two coherent daughter solitons. These then traverse different paths accumulating a phase difference and are then recombined on a potential barrier. There are various ways to obtain two coherent solitons. One can employ Bragg diffraction momentum transfer in order to separate the soliton into equally sized states of different momentum or one can use a potential barrier.

When using a potential barrier to split solitons, it is known that narrower barriers offer the best conditions for soliton interferometry. This is due to the fact that it is desirable for the outcome of the collision to be two equally sized solitons with equal and opposite velocities. We want them to interact with the barrier for only a small amount of time in order to minimise nonlinear effects. Using a sufficiently narrow barrier means that one can be in the tunnelling re-

gime wherein a portion of the incident soliton tunnels through the barrier. A bright soliton has a finite width momentum distribution and so one must ensure that splitting occurs through tunnelling rather than a velocity filtering effect which would result in outgoing solitons with different speeds.

1.3 Publications

Publications of research contained in this thesis are:

i. Splitting of two-component solitary waves from collisions with narrow potential barriers, Callum L. Grimshaw, Simon A. Gardiner, and Boris A. Malomed Phys. Rev. A 101, 043623 —- Published 28 April 2020

ii. Soliton interferometry with very narrow barriers obtained from spatially dependent dressed states, Callum L. Grimshaw, Thomas P. Billam, and Simon A. Gardiner — Pending publication

1.4 Thesis outline

Chapter 2 will cover the relevant underlying physics including: Bose–Einstein condensates; atomic physics; the Gross–Pitaevskii equation; solitons, in various forms and areas of physics (as well as the more specific types found in BEC systems), and then the numerical techniques utilised in the research.

In chapter 3 I will outline the research conducted on the interaction, in the low energy limit, of two component solitons with potential barriers developed using perturbation theory and then examined using computational simulations. This work was published as a collaboration with B. A. Malomed of Tel Aviv University.

In chapter 4 I will discuss work done on the use of geometric potentials as a means to provide a very narrow barrier to split solitons in an interferometry scheme and examine the feasibility and imperfections of the scheme in the specific context of soliton interferometry. This work was is currently under the publication review process and was conducted as a collaboration with T. P. Billam of Newcastle University.

Chapter 2

Theory

2.1 Bose–Einstein condensates

In a famous letter to Albert Einstein in the early 1920s, Satyendra Nath Bose described his method for deriving the constant in Planck's law independently of using classical electrodynamics. He did this by considering the phase-space density of quantum (indistinguishable) particles. Einstein translated Bose's letter into German for publication in the journal *Zeitschrift für Physik* [11]. Einstein understood the significance of this result and published a further three papers of his own on the subject [12–14]. In these works, he described what is now known as Bose–Einstein condensation and also defended the work of Bose against criticism (particularly from Paul Ehrenfest). The main point of argument was the principle and statistical implications of indistinguishable particles (which affects the system entropy and enables wave interference). The importance of quantum distributions to particles according to their spin characteristics is now well understood. A classical (Maxwell–Boltzmann) distribution is recovered as a limiting case.

The similarity between a Bose–Einstein condensate and liquid helium-4 was noted in 1938 by London who pointed out the similarities between the Λ-transition and the onset of condensation in idealised Bose particles. The absence of the Λ-transition in helium-3 corroborated this view; however, it was unclear how to reconcile the concept of BEC in an ideal gas with a strongly interacting fluid. In 1947 Tisza elaborated on the shared characteristics by

presenting a two-fluid hydrodynamical model for liquid helium-4 [15]. Bogolyubov explored the theory of condensation for weakly interacting particles [16]. In 1956, a more general statement of the BEC condition was presented by Penrose and Onsager [17] which proposed that one is formed when the proportional occupation of a single state takes on a "finite"fraction, i.e. on the order of 1. Thus the definition applies to interacting particles and does not necessarily have to constitute the ground state. The exclusion of fermions from the possibility that they can undergo the BEC transition is thus implied as they cannot host multiple occupation of a single state.

Indeed an ideal Fermi gas cannot undergo condensation but interactions between the fermions can form composite bosonic particles which can be condensed. This phenomenon offers an explanation for superconductivity where BCS theory describes the Bose–Einstein condensation of Cooper pairs (interacting electrons mediated via the electron-phonon attraction). One can alter the scattering lengths in order to probe the BCS-BEC crossover [18]. Furthermore, one should note that this is what is what happens in the Bose–Einstein condensation of dilute gases of alkaline atomic species. The alkaline atoms consist of an extremely dense nucleus made up of protons and neutrons bound together by the strong force and is surrounded by orbitals of electrons [19]. The elemental nature of the species is determined by the number of positively charged protons [20] which are accompanied by an equal number of electrons in the neutral atomic state. The neutron number determines the nuclear stability of an isotope and is also important to the statistical behaviour of the dilute atomic gas at low temperatures as it determines the overall nuclear spin. In order for Bose–Einstein condensation to be possible, one requires the nuclear spin to be half integer (i.e. to be composed of an uneven number of fermionic nucleons) so that, when coupled to the single electron in the highest atomic state, the atom will have an overall integer spin. In a dilute gas, the atoms are well separated and the quantum state is labelled by its hyperfine state (usually denoted as $|F, M_F\rangle$ corresponding to the total angular momentum of the electron and the nucleus and its projection onto the z-axis).

In condensed matter physics, coupling between electrons and holes can form excitons and excitons coupled to cavity photons have been shown to undergo BEC (exciton-polariton systems have a lower effective mass than excitons and

can be thought of as a bosonic quasiparticle) [21, 22].

Since their initial production in dilute alkali atomic gases, BECs have been formed in various other systems including: exciton-polaritons [23], photons [24], superconductors (Cooper pairs) [25] and magnons (collective spin excitations in condensed matter physics) [26].

2.1.1 Statistical theory of BEC

A statistical theory of indistinguishable particles without a maximum occupation of a single state leads to the Bose–Einstein distribution. The distribution has the form

$$n(\epsilon_{\vec{k}}) = \frac{1}{e^{\beta(\epsilon_{\vec{k}}-\mu)}-1}, \tag{2.1}$$

where $\beta = 1/k_{\mathrm{B}}T$, T denotes the temperature, k_{B} is Boltzmann's constant, $\epsilon_{\vec{k}}$ is the energy of the state with wavevector $\vec{k}$ and $\mu \leq 0$ is the chemical potential. If the particles are fermionic and obey the Pauli exclusion principle then the corresponding distribution is known as the Fermi–Dirac distribution, given by

$$n(\epsilon_{\vec{k}}) = \frac{1}{e^{\beta(\epsilon_{\vec{k}}-\mu)}+1}. \tag{2.2}$$

In the limit of high temperature and low density, both distributions approach the classical Maxwell–Boltzmann limit. From the expression for the Bose–Einstein distribution, Eq. (2.1), one can see that with decreasing temperature, in order to keep the particle number constant one must increase the chemical potential. However, after reaching $\mu = 0$, the only way to achieve this is to macroscopically occupy the ground state. This allows one to calculate the transition temperature T_c by equating the number of excited atoms at zero chemical potential ($\langle N'(\mu = 0, T_c)\rangle$) to the number of atoms ($\langle N\rangle$). For a three-dimensional system of particles with a mass m, this gives

$$\begin{aligned}\langle N\rangle = \langle N'(\mu = 0, T_c)\rangle &= \sum_{\vec{k}\neq 0} N_{BE}(\epsilon_{\vec{k}}) = \frac{V}{2\pi^2}\int_0^\infty \frac{k^2 \mathrm{d}k}{\exp\left[\beta(T_c)\epsilon_{\vec{k}}\right]-1} \\ &= \frac{V m^{3/2}}{\sqrt{2}\pi^2\hbar^3}\int_0^\infty \frac{\sqrt{\epsilon_{\vec{k}}}\mathrm{d}\epsilon}{\exp\left[\beta(T_c)\epsilon_{\vec{k}}\right]-1}.\end{aligned} \tag{2.3}$$

The integral can be found exactly using

$$\int_0^\infty \frac{(x^{a-1})\mathrm{d}x}{e^x - 1} = \zeta(a)\Gamma(a), \tag{2.4}$$

to give

$$n = \frac{\langle N \rangle}{V} = \zeta(3/2)\left(\frac{m k_B T_c}{2\pi\hbar^2}\right)^{3/2}, \tag{2.5}$$

where $\zeta(3/2)$ is the Riemann ζ-function evaluated for the argument 3/2. For temperatures below T_c, the number density of the excited states is

$$n'(T) = \zeta(3/2)\left(\frac{m k_\mathrm{B} T}{2\pi\hbar^2}\right)^{3/2}. \tag{2.6}$$

Thus the number density of the ground state (the condensed population) is given by

$$n_0(T) = n - n'(T) = n\left[1 - \left(\frac{T}{T_c}\right)^{3/2}\right]. \tag{2.7}$$

Note that the condensation temperature is proportional to $n^{2/3}/m$. Similarly, one can calculate the average energy per particle as

$$u = \frac{3 k_\mathrm{B} T^{5/2} \zeta(5/2)}{2 T_c^{3/2} \zeta(3/2)}. \tag{2.8}$$

The (isochoric) specific heat capacity is given by

$$c_V = \left(\frac{\partial u}{\partial T}\right)_V. \tag{2.9}$$

For $T \gg T_c$, $c_V = 3k_B/2$ and for $T < T_c$

$$c_V = \frac{15 k_\mathrm{B}}{4} \frac{\zeta(5/2)}{\zeta(3/2)} \left(\frac{T}{T_c}\right)^{3/2}. \tag{2.10}$$

The two expressions for the specific heat capacity are discontinuous across the transition temperature. This implies that the free energy is not analytic at T_c and therefore the Bose–Einstein condensation is a true thermodynamic phase transition. The BEC can be further said to arise when the de Broglie waves of the constituent bosons start to overlap and quantum degeneracy is reached. The thermal de Broglie wavelength can be defined as

$$\lambda_\mathrm{th} = \frac{h}{\sqrt{2\pi m k_\mathrm{B} T}}, \tag{2.11}$$

where h is Planck's constant. This expression represents the de Broglie wavelength associated with the thermal distribution of momentum. When the average interparticle separation is less than the wavelength, one expects quantum effects to be important as wave interference becomes more prevalent. Quantum degeneracy is reached as a particle at a position $\vec{r}$ is indistinguishable from a particle another position $\vec{r}'$, in analogy with the Rayleigh criterion for angular resolution.

2.1.2 Ultracold quantum field theory of BEC

When one distinguishes between first and second quantisation in quantum theory, one is referring to different representations of the wavefunctions describing the particles in the system. The act of quantisation denotes the adaptation of a classical formulation of mechanics to a quantum formulation in which dynamical co-ordinates become operators. Naturally, the classical picture re-emerges from the quantised formulation when the action, $S = \int \mathcal{L}\,\mathrm{d}t$, is much greater than (reduced) Planck's constant, $\hbar$. Formally this is known as a group contraction [27] and can also be applied to recover classical descriptions of physics from relativistic descriptions under certain limits. In the first quantisation picture, one formulates the Hamiltonian in terms of the position and momentum operators, $\hat{x}_i$ & $\hat{p}_i$, and includes an interaction potential, $V(\hat{x}_i - \hat{x}_j)$, as

$$\hat{H} = \sum_{i=1}^{N} \left[\frac{\hat{p}_i^2}{2m} + V(\hat{x}_i) \right] + \frac{1}{2} \sum_{i \neq j=1}^{N} V\left(\hat{x}_i - \hat{x}_j\right), \tag{2.12}$$

where the operators satisfy the commutator $[\hat{x}_i, \hat{p}_j] = i\hbar\delta_{ij}$ and the factor $1/2$ preceding the interaction potential accounts for duplication in this description of the two-body interaction terms. We can try to solve this for a general case and construct the N-body wavefunction. We must first note the behaviour of the wavefunction under the exchange of two particles. If one applies the exchange twice then the wavefunction is the same as before. This implies that the wavefunction can take a phase of either 0 or π (corresponding to factors of +1 and -1 respectively), depending on whether the particles follow Bose–Einstein or Fermi–Dirac statistics, as the observable norm of the wavefunction is unaltered. Other types of particles known as anyons are possible in low-dimensional systems as a quasiparticle excitation which take on a more general phase change. These quasiparticles are known to be involved in the fractional quantum Hall effect [28, 29].

Knowing how many particles are in each mode of the system, one can find possible eigenstates of the Hamiltonian. In this case, one must sum over all possible permutations of the particle configuration and normalise accordingly. If all possible states are in a single mode then the normalisation factor is 1 and the state is unique. Whereas, if there are N_0 bosonic particles in the mode 0, N_1 particles in the mode 1 et cetera, then the normalisation factor is $\sqrt{N_0!N_1!.../N!}$

and there are $N!/N_0!N_1!...$ possible permutations. Similar state construction is achieved for fermions but accounting for the exchange factor of -1 with an antisymmetric wavefunction. This antisymmetric structure is conveniently encapsulated using a determinant. This is known as the Slater determinant.

It becomes simpler to work in the Fock or occupation basis in which, rather than denote the state in which each particle resides, one denotes the number of particles in each state. Take as an example a system of two bosons (denoting boson 1 and 2 with subscripts 1 and 2, respectively and assuming distinguishability only for purposes of explanation) in a harmonic oscillator. The ground state is

$$|2,0,...\rangle = |0\rangle_1 |0\rangle_2 , \tag{2.13}$$

meaning that in order to form a state in which both particles occupy the ground state, particle 1 and particle 2 must be in the ground state of the harmonic oscillator. The first excited state is

$$|1,1,0,...\rangle = \frac{1}{\sqrt{2}}(|0\rangle_1 |1\rangle_2 + |1\rangle_1 |0\rangle_2), \tag{2.14}$$

corresponding to a superposition of states in which either particle occupies the excited state and an exchange of the particles does not impart a phase factor. Further, let us take an example system of two fermions (fermion 1 and fermion 2) in a harmonic oscillator. The ground state is

$$|1,1,0,...\rangle = \frac{1}{\sqrt{2}}(|0\rangle_1 |1\rangle_2 - |1\rangle_1 |0\rangle_2), \tag{2.15}$$

corresponding to a superposition of states in which either particle occupies the excited state and an exchange of the particles imparts a phase factor of -1.

Extending to the general expression for N bosons gives the useful behaviours of the bosonic creation and annihilation operators (denoted by $\hat{a}_k^\dagger$ and $(\hat{a}_k)$, respectively)in this representation

$$\hat{a}_k |N_0,...,N_k,...\rangle = \sqrt{N}\,|N_0,...,N_k-1,...\rangle , \tag{2.16}$$

$$\hat{a}_k^\dagger |N_0,...,N_k,...\rangle = \sqrt{N+1}\,|N_0,...,N_k+1,...\rangle , \tag{2.17}$$

with the operators satisfying

$$[\hat{a}_k, \hat{a}_l^\dagger] = \delta_{kl}, \tag{2.18}$$

$$[\hat{a}_k, \hat{a}_l] = 0, \tag{2.19}$$

$$[\hat{a}_k^\dagger, \hat{a}_l^\dagger] = 0. \tag{2.20}$$

Correspondingly for the fermionic operators

$$\hat{b}_k |N_0, \ldots, N_k, \ldots\rangle = \sqrt{N} |N_0, \ldots, N_k - 1, \ldots\rangle, \tag{2.21}$$

$$\hat{b}_k^\dagger |N_0, \ldots, N_k, \ldots\rangle = \sqrt{1 - N} |N_0, \ldots, N_k + 1, \ldots\rangle, \tag{2.22}$$

with anti-commutators

$$\{\hat{b}_k, \hat{b}_l^\dagger\} = \delta_{kl}, \tag{2.23}$$

$$\{\hat{b}_k, \hat{b}_l\} = 0, \tag{2.24}$$

$$\{\hat{b}_k^\dagger, \hat{b}_l^\dagger\} = 0, \tag{2.25}$$

noting that this algebra ensures that for fermions $N_k \in \{0, 1\}$.

Working within this framework allows us to extend the creation and annihilation operators procedure to quantum fields. For bosonic field operators, we thus define

$$\hat{\Psi}(\vec{x}) = \sum_{\vec{k}} \hat{\Psi}_{\vec{k}}(\vec{x}) = \sum_{\vec{k}} \hat{a}_{\vec{k}} \psi_{\vec{k}}(\vec{x}), \tag{2.26a}$$

$$\hat{\Psi}^\dagger(\vec{x}) = \sum_{\vec{k}} \hat{\Psi}_{\vec{k}}^\dagger(\vec{x}) = \sum_{\vec{k}} \hat{a}_{\vec{k}}^\dagger \psi_{\vec{k}}^*(\vec{x}), \tag{2.26b}$$

which follow the commutation relations

$$[\hat{\Psi}(\vec{x}), \hat{\Psi}^\dagger(\vec{y})] = \delta(\vec{x} - \vec{y}), \tag{2.27}$$

$$[\hat{\Psi}(\vec{x}), \hat{\Psi}(\vec{y})] = 0, \tag{2.28}$$

$$[\hat{\Psi}^\dagger(\vec{x}), \hat{\Psi}^\dagger(\vec{y})] = 0. \tag{2.29}$$

The field operators can be interpreted as creating or annihilating a particle at a position, $\vec{x}$.

Considering a quantum field approach rather than a statistical one, the BEC state is categorised by its off-diagonal long-range order (ODLRO). Let us define the single particle density matrix

$$\rho_1(\vec{x}, \vec{y}) = \langle \hat{\Psi}^\dagger(\vec{x}) \hat{\Psi}(\vec{y}) \rangle. \tag{2.30}$$

Note that this definition implies that $\rho_1(\vec{x}, \vec{x}) = n(\vec{x})$, the particle number density. Bose–Einstein condensation occurs when a single quantum state has most

of the occupation. Consequently, the system remains unperturbed if a particle from position $\vec{x}$ is removed and a particle is added to $\vec{y}$ and so the single particle density matrix does not vanish over long distances. The separation between two particles is $|\vec{x}-\vec{y}|$. Normally $\rho_1(\vec{x},\vec{y})$ decays exponentially with $|\vec{x}-\vec{y}|$; however, for the BEC it does not and this signifies a maintenance of spatial coherence over a large distance. The ODLRO only exists if the system exhibits macroscopic occupation of the zero momentum state and therefore the ODLRO is a definition of the BEC state of matter. Diagonal long-range order (DLRO) is indicative of a solid phase of matter (in other words a crystalline nature). As will be shown, ODLRO implies a superfluid flow. If a system possess both ODLRO and DLRO then it has the implied properties of long-range configurational order as well as superfluidity. This phase is known as a supersolid and has been demonstrated in dipolar quantum gases [30, 31].

By definition, in the Bose–Einstein condensed system, one considers a quantum superposition of states (in the Fock representation) $|N_0,...\rangle$, where $N_0 = \langle \hat{\Psi_0}^\dagger \hat{\Psi_0}\rangle$. If the total atom number $\langle N\rangle \gg 1$ then $\hat{\Psi_0}^\dagger \hat{\Psi_0}|N_0,...\rangle$ and $\hat{\Psi_0}\hat{\Psi_0}^\dagger|N_0,...\rangle$ can be approximated by $\langle N_0\rangle|N_0,...\rangle$ noting that $[\hat{\Psi_0}(\vec{r}),\hat{\Psi_0}^\dagger(\vec{r'})] = \delta(\vec{r}-\vec{r'})$. Thus we can consider that the non-commutativity of field operators $\hat{\Psi_0}$ and $\hat{\Psi_0}^\dagger$ can be neglected for $N_0 = O(N), N \gg 1$. Thus the order parameter describing the quantum field may be written as ordinary complex numbers using the Bogoliubov substitution as

$$\Psi(\vec{x},t) = \sqrt{n(\vec{x},t)}e^{i\theta(\vec{x},t)}, \tag{2.31}$$

where $n(\vec{x},t) = |\psi(\vec{x},t)|^2$. The current $\vec{j}$ is defined as

$$\vec{j} = \frac{\hbar}{2mi}\left[\Psi^*(\nabla\Psi) - (\nabla\Psi^*)\Psi\right], \tag{2.32}$$

which satisfies the continuity equation

$$\partial_t n + \nabla\cdot\vec{j} = 0. \tag{2.33}$$

The current j is associated with a velocity, $\vec{v}$, which is found by substituting Eq. (2.31) into Eq. (2.32). Thus one arrives at the relationship between the velocity and the phase,

$$\vec{v} = \frac{\hbar}{m}\nabla\theta. \tag{2.34}$$

Importantly, Eq. (2.34) implies that the velocity is irrotational ($\nabla\times v = (\hbar/m)\nabla\times\nabla\theta = 0$ since $\nabla\times\nabla f = 0 \forall f$ if f is a smooth variable).

Note that the global phase is necessarily arbitrary and arises from the conservation of the particle number, N. The phase acts like a potential for the velocity and, clearly, if a transformation $\Psi = \sqrt{n(\vec{x},t)}e^{i\theta(\vec{x},t)} \rightarrow \Psi e^{i\theta_0}$ is made then $|\Psi|^2$ and $\nabla\theta$ and thus n and $\vec{v}$ are unchanged. It is only possible to measure the effects of phase differences between multiple carriers. When a bosonic substance reaches quantum degeneracy, it is understood to break a U(1) symmetry and acquire a random phase, θ. This is in analogy to the phase transition underlying a magnetisation process wherein the magnet spontaneously breaks a spherical symmetry and acquires a random magnetisation axis.

It can be shown mathematically [32] that the superfluid density in an ideal Bose gas is equal to the total condensate density. This implies that all of the superfluidity is a result of the Bose–Einstein condensation. However, when the same treatment is applied to an interacting system, this is not case and the superfluid is composed of a condensed and a non-condensed fraction. In ^{4}He, a strongly interacting system, at low temperatures the superfluid fraction is close to 1 whereas the condensate fraction is known to be around 0.1. Therefore the BEC and the superfluid are closely related phenomena but are not the same.

2.1.3 Experimental methods

Demonstrating the BEC state and the utility of the alkaline BEC

Experimentalists tried for many years to attempt to create a BEC using different approaches to cool down bosons to quantum degeneracy. Several physicists expressed doubt on whether such a state was possible although the existence of a condensate could be used to explain emergent properties in cold systems such as superfluids and superconductors. In superfluid helium, the presence of a condensate fraction was inferred from the nature of its excitation spectrum although the strong interactions prevent large occupation of the ground state.

Due to its weak interaction and its lack of a non-gaseous phase at absolute zero, spin-polarised (to suppress recombination) atomic hydrogen was used extensively in experimental efforts to produce a BEC. Eventually, experiments came to within a factor of five of the condensation temperature. The BEC phase of atomic hydrogen was finally reached in 1998 [33]. On the 5$^{\text{th}}$ June 1995, the first

gaseous BEC was formed in a laboratory in Colorado, USA [34]. The bosonic species used to form the BEC was ^{87}Rb, a dilute atomic gas. Alkaline BECs of other species (sodium and lithium) were soon realised [35, 36]. Dilute atomic gases would seem to be undesirable candidates for a BEC due to their composite nature, large mass and low density. However, the alkali gases have an atomic structure which can be easy to understand due to their having one electron in the outer shell (the inner electrons contribute zero overall spin and angular momentum to the overall quantum state). Furthermore, the simple atomic structure of the alkali atoms enables them to be laser cooled and trapped magnetically using non-contact forces. After laser cooling, the sample of atoms can be placed into a magnetic trap which is then lowered in depth so that only the least energetic atoms are retained. This is known as evaporative cooling. The dilute nature of the alkali gases means that their interactions are long-range scattering processes and at low temperatures are dominated by *s*-wave scattering. The *s*-wave scattering therefore dictates the strength of the interaction and can be varied using Feshbach resonances. The less naturally abundant isotope of rubidium with 87 nucleons has a positive scattering length at low temperatures (as opposed to ^{85}Rb) and possesses convenient properties pertinent to evaporative cooling. In addition to these convenient properties, it also has near equal singlet and triplet scattering lengths which allows the formation of a stable two component condensate consisting of two hyperfine states of ^{87}Rb due to a suppression of three-body loss [37].

Laser cooling

The most important experimental development in the route to the creation of the first laboratory BEC was laser cooling. Lasers can be used to cool dilute alkali atomic gases down to temperatures where quantum degeneracy can be realised using the various approaches of laser cooling. The principle of laser cooling was proposed in 1975 by Theodor Hänsch and Arthur Schawlow [38]. The method works by utilising the dissipative force imparted by the laser to slow down the gas. There are also the popular Doppler cooling mechanism and various sub-Doppler cooling mechanisms (such as grey molasses and Sisyphus cooling). In addition to laser cooling, experimentalists can use evaporative cooling to further decrease the temperature of the gas by decreasing the

trap depth so that the atoms with the highest kinetic energy leave the trap.

Trapping of neutral atoms

In order to study the properties of alkaline atomic BECs, one needs to be able to readily cool and trap the constituent atoms. Neutral atoms are often trapped using either magnetic traps or optical traps. The former trap atoms depending on the magnetic moments of the outer single electron (for alkaline gases) whereas the optical dipole traps impart a restoring force onto the atoms depending on the electric moment and thus independently of the Zeeman sublevels, denoted conventionally by M_F, of which there are $2F+1$ where $|S-I| \leq F \leq S+I$ is the hyperfine spin and S and I denote the electronic and nuclear spins, respectively. Note that F is even here by definition since we are concerned with species which can form BECs. It became apparent that the combination of magnetic trapping and evaporative cooling and subsequently transfer into an optical trap is often the easiest route to realising a BEC. An exception to this is the case of caesium for which this was difficult to achieve owing to the enhancement of two-body losses from the magnetically trappable states [39]. The ability to form a Cs BEC as well as to form a spinor BEC therefore motivated the search for a route to create a BEC using only optical trapping processes. This was achieved for ^{87}Rb in 2001 [40] and for ^{133}Cs in 2003 [41]. Further advantages of the optical traps are the higher degree of control afforded through the lasers such as the control over the beam profile as well as over the detuning which is to be large so as to reduce spontaneous emission and can be positive or negative corresponding to repulsive or attractive potentials. Stabilisation can be achieved through feedback methods and standing waves can be formed in order to produce optical lattices.

The potential formed by a far-detuned laser ($\Delta \gg \Gamma, \Omega$) is [42]

$$U(\vec{r}) = \frac{\hbar\Gamma^2}{8I_s}\frac{I(\vec{r})}{\Delta} = \frac{3\pi c^2}{2\omega_0^3}\frac{\Gamma}{\Delta}I(\vec{r}), \tag{2.35}$$

where Γ is the natural linewidth of the excited state of the atom, Ω is the Rabi frequency, ω_0 is the atomic transition frequency, $\Delta = \omega - \omega_0$ is the detuning from the resonance, I_s is the saturation intensity and I is the laser intensity.

The scattering rate is given by

$$\Gamma_{sc} = \frac{\Gamma}{\hbar\Delta}, \tag{2.36}$$

and so increasing the detuning whilst also increasing the intensity maintains U but lowers Γ_{sc}.

2.2 Quantum scattering of bosons

Solitons emerge as a phenomenon in nonlinear physics. In the BEC, the nonlinearity arises from the interactions between atoms which in the limit of low energy are dominated by isotropic s-wave scattering. In this limit, and also when the interatomic distance is much larger than the interaction range, it becomes unnecessary to know the details of the short distance behaviour of the the interaction potential. Thus one may model the interaction potential between the atoms using the pseudopotential

$$U(\vec{r}-\vec{r}') = g\delta(\vec{r}-\vec{r}') = \frac{4\pi\hbar^2 a_s}{m}\delta(\vec{r}-\vec{r}'), \tag{2.37}$$

where a_s is the s-wave scattering length and m is the mass of the atom.

Interestingly, there are other interaction regimes available, for example, in condensates with large dipole moments one must consider the dipole interaction which is anisotropic and couples different partial waves (which all contribute to the low energy scattering regime). If one tunes the s-wave scattering length to become negligible then one can engineer BECs where the dominant interactions are anisotropic.

2.2.1 Theory

The fundamental difference between the quantum scattering of bosons and fermions lies in the symmetry constraints imposed by quantum mechanics. This dictates that indistinguishable bosons can only interact via potentials with even parity. Another consequence of quantum indistinguishability on the scattering behaviour arises when considering the trajectories. For example, if two identical particles scatter off one another in a head-on collision and the result

is a deflection by a small angle, θ, then this is not distinguishable from a large deflection by an angle, $2\pi - \theta$.

Quantum scattering is described in terms of partial wave analysis. Here, one assumes a central potential, $V(\vec{r}) = V(r)$, and separates the radial and angular behaviour of the Schrödinger equation. Taking k^2 as the energy in units of $\hbar^2/2\mu$, where $\mu = m_1 m_2/(m_1 + m_2)$ is the reduced mass of the two scattering bosons of mass m_1 and m_2,

$$\psi(\vec{r}) = \sum_{l=0}^{\infty} \sum_{m=-l}^{l} c_{lm} R_l(k,r) Y_{lm}(\theta,\phi), \tag{2.38}$$

where $R(k,r)$ represents the radial part of the wavefunction and $Y_{lm}(\theta,\phi)$ are the spherical harmonics, which are simultaneously eigenfunctions of the $\hat{L}^2$ and $\hat{L}_z$ angular momentum operators, with eigenvalues $l(l+1)\hbar^2$ and $m\hbar$, respectively. This gives the radial Schrödinger equation (in dimensionless form by multiplying by $2\mu/\hbar^2$)

$$\frac{d^2R_l}{dr^2} + \frac{2}{r}\frac{dR_l}{dr} - \frac{l(l+1)}{r^2}R_l + k^2 R_l - U(r)R_l = 0, \tag{2.39}$$

where $U(r) = 2\mu/\hbar^2 V(r)$. When the interaction is short-range one looks for the phase shift, δ_l. For the short-range central potential, the long distance solution for the radial equation is

$$R_l(k,r) = A_l(k)[j_l(kr) - \tan\delta_l n_l(kr)], \tag{2.40}$$

where $A_l(k)$ takes the role of a normalisation constant and j_l and n_l are the spherical Bessel functions which are generated by

$$j_l(x) = (-x)^l \left(\frac{1}{x}\frac{d}{dx}\right)^l \frac{\sin x}{x}, \tag{2.41}$$

$$n_l(x) = -(-x)^l \left(\frac{1}{x}\frac{d}{dx}\right)^l \frac{\cos x}{x}. \tag{2.42}$$

The dominant partial waves are given by those l for which $\sqrt{\hbar^2 l(l+1)} \lesssim \hbar a k \Rightarrow l \lesssim ak$, where a is the range of the scattering potential. In the low energy regime only $\tan\delta_0$ is non-negligible and the scattering is isotropic with the differential cross section

$$\frac{d\sigma}{d\Omega} = a_s^2, \tag{2.43}$$

where a_s is the s-wave scattering length

$$a_s = -\lim_{k\to 0} \frac{\tan\delta_0(k)}{k}. \tag{2.44}$$

2.2.2 Experimental methods

As well as the use of light forces generated from lasers, another key experimental tool for the study of the physics of BECs is the widely used Feshbach resonance technique which allows control of the s-wave scattering length. A Feshbach resonance is a resonance between a scattering state in one collision channel and a bound state in another in a many-body system [32]. The presence of the intermediate bound state in a scattering process alters the energy of the scattering state. If an external magnetic field is present then the energy of the bound state relative to the open-channel threshold can be altered. Around this resonance, the s-wave scattering length (proportional to the energy shift caused by the resonance) changes as

$$a = a_{\mathrm{bg}}\left(1 - \frac{\Delta}{B - B_0}\right), \tag{2.45}$$

where Δ is the width of the resonance, a_{bg} is the background scattering length and B_0 is the value of the magnetic field where the resonance exists.

The resonance between a scattering state and a bound state can be brought about by means other than an external magnetic field. If implemented optically, then it is known as an optical Feshbach resonance and if it is caused by a quasi-bound state that is supported by an open channel potential rather than by a closed channel potential, it is known as a shape resonance. In low-dimensional systems, there are additional methods to control the effective 1D nonlinearity magnitude. Varying the transverse confinement frequency can also induce a resonance. In this case, the confinement-induced resonance is brought about by the coincidence of the scattering length with the characteristic transverse trapping potential lengthscale, $a_r = \sqrt{\hbar/m\omega_r}$. One can interpret this as a Feshbach resonance between a bound state and the lowest energy transverse mode. This has been observed in a 1D Fermi gas [43].

Thus the Feshbach resonance allows one to directly control the collisional properties of the BEC by varying the s-wave scattering length. This technique can be used to rapidly change the BEC from repulsively interacting to attractively interacting. Also, Feshbach resonances can be used to spatially vary the collisional properties of a BEC. Similar to the Feshbach resonance, the nature of the dipolar interaction can be varied between repulsive and attractive using time-varying electromagnetic fields.

Experimentally, it is necessary to trap the condensate. This can be done using magnetic confinement or optical confinement. Purely magnetic confinement provides a harmonic trap which, in the case of strong transverse (relative to axial) trapping, results in a highly prolate trap. This environment gives the conditions that would allow one to justify using the 1DGPE. The presence of the trapping potential removes the integrability of the system and so the solutions are not true solitons (they change their shape while they move within the trap); however, they have most of the properties that are attributed to solitons and are referred to as solitary waves [44].

2.3 The Gross–Pitaevskii equation

In order to understand the formation of bright matter-wave solitons, it is worth having knowledge about the formation of Bose–Einstein condensates. The premise behind BEC is that when bosons are cooled down to sufficiently low temperatures, many particles can enter the same state and so the BEC is described by a single macroscopic wavefunction. The many-boson Hamiltonian is given by

$$\begin{aligned}\hat{H} = &\int d^3r \hat{\Psi}^\dagger(\vec{r})\Big[-\frac{\hbar^2}{2m}\nabla^2 + V(\vec{r})\Big]\hat{\Psi}(\vec{r}) \\ &+ \frac{1}{2}\iint d^3r d^3r' \hat{\Psi}^\dagger(\vec{r})\hat{\Psi}^\dagger(\vec{r}')U(\vec{r}-\vec{r}')\hat{\Psi}(\vec{r}')\hat{\Psi}(\vec{r}).\end{aligned} \tag{2.46}$$

If one considers scattering at low energy, then one may reduce the potential term by assuming a contact interaction, $U(\vec{r}-\vec{r}') = g\delta(\vec{r}-\vec{r}')$, as in Eq. (2.37). This allows one to simplify the interaction potential term to give

$$\hat{H} = \int d^3r \hat{\Psi}^\dagger(\vec{r})\Big[-\frac{\hbar^2}{2m}\nabla^2 + V(\vec{r}) + \frac{g}{2}\hat{\Psi}^\dagger(\vec{r})\hat{\Psi}(\vec{r})\Big]\hat{\Psi}(\vec{r}). \tag{2.47}$$

One then uses the equation of motion for an operator in the Heisenberg picture

$$i\hbar\frac{d}{dt}\hat{\Psi} = [\hat{\Psi}, \hat{H}]. \tag{2.48}$$

Using the fact that $\hat{\Psi}$ has no explicit time dependence, and then taking the mean-field, $\Psi = \langle\hat{\Psi}\rangle$, one arrives at the GPE

$$i\hbar\frac{\partial}{\partial t}\Psi(\vec{r},t) = \Big[-\frac{\hbar^2}{2m}\nabla^2 + V(\vec{r}) + g|\Psi(\vec{r},t)|^2\Big]\Psi(\vec{r},t). \tag{2.49}$$

This is the GPE equation for a 3-dimensional BEC.

2.3.1 Reduction to one dimension and dimensionless units

If the BEC is strongly confined in two directions, then we can assume that the trapping potential dominates over the interaction potential in these directions. This justifies the use of a Gaussian ansatz (the ground state of the harmonic potential).

The GPE for a condensate in a highly prolate trap can be simplified if one takes the following ansatz

$$\Psi(\vec{r},t) = \psi(x)\sqrt{\frac{m\omega_r}{\pi\hbar}}\exp\Big(-\frac{m\omega_r r^2}{2\hbar}\Big). \tag{2.50}$$

Integrating over the radial direction and defining $g_{1D} = 2\hbar\omega_r a_s$ gives the quasi-1D GPE

$$i\hbar\frac{\partial}{\partial t}\psi(x,t) = \Big[-\frac{\hbar^2}{2m}\frac{\partial^2}{\partial x^2} + V(x) + g_{1D}|\psi(x,t)|^2\Big]\psi(x,t). \tag{2.51}$$

When $V(x) = 0$, the 1DGPE is integrable and thus can be exactly solved using the inverse-scattering technique. The solution for $a_s < 0$ is a bright soliton which takes the form

$$\psi(x,t) = \frac{a_r}{\sqrt{2|a_s|}\kappa}\text{sech}\Big(\frac{x-vt}{\kappa}\Big)\exp\Big[\frac{imv}{\hbar}x - \frac{i}{\hbar}\Big(\frac{mv^2}{2} - \frac{\hbar^2\kappa^2}{2m}\Big)t\Big], \tag{2.52}$$

where κ is known as the soliton width and is defined as $\kappa = a_r^2/(|a_s|N)$. v is the soliton velocity.

From a theoretical perspective, when discussing the GPE, it is often best to re-write it in terms of dimensionless quantities by transforming the variables x, t & ψ into the variables $\tilde{x}, \tilde{t}$ & $\tilde{\psi}$ which are often defined using either soliton units or harmonic trap units. The units used in this thesis are soliton units which are defined as

$$\tilde{x} = \frac{m|g_{1D}|N}{\hbar^2}x \tag{2.53a}$$

$$\tilde{t} = \frac{m|g_{1D}|^2N^2}{\hbar^3}t \tag{2.53b}$$

$$\tilde{\psi} = \frac{\hbar}{\sqrt{m|g_{1D}|N}}\psi. \tag{2.53c}$$

It is also useful to define the energy and velocity in dimensionless variables

$$\tilde{E} = \frac{\hbar^2}{m|g_{1D}|^2N^2}E \tag{2.54a}$$

$$\tilde{v} = \frac{\hbar}{|g_{1D}|N} v. \tag{2.54b}$$

Using these units (with the ψ normalised to 1), and assuming $g_{1D} < 0$, the GPE takes the following form

$$i\frac{\partial \psi}{\partial t} = \Big[-\frac{1}{2}\frac{\partial^2}{\partial x^2} + V(x) - |\psi|^2 \Big]\psi. \tag{2.55}$$

The bright soliton solution for $V = 0$ in this unit system is,

$$\psi(x,t) = \frac{1}{2}\mathrm{sech}\Big(\frac{x - x_0 - vt}{2}\Big) e^{i[vx-(v^2/2-1/8)t]}. \tag{2.56}$$

Generally, a $t = 0$ solution to Eq. (2.55) is $A\mathrm{sech}[A(x-x_0)]e^{ivx}$ with a norm of $2A$; however, Eq. (2.56) is the ground state solution with a norm of 1 (all of the population of N atoms in this unit system).

2.3.2 Pseudospinor Gross–Pitaevskii equation

The GPE can be generalised to describe the motion of solitons composed of multiple BEC components. This involves considering the components as elements of a spinor. In this area of research, one generally distinguishes between "true"spinors and pseudospinors; the difference being that in "true"spinors, there are lossless spin-changing collisions which significantly influence the dynamics of the condensate [45] whereas the name pseudospinors originates from the equivalence between a two-level system and a spin-1/2 system [46].

A multiple component BEC could consist of heteronuclear mixtures or homonuclear mixtures. In the case of homonuclear mixtures, different quantum states can be considered to conserve their populations if there is no route for collisional interconversion of the different states. Also, there is the well-known stable doublet of the ^{87}Rb states $|2,1\rangle$ & $|1,-1\rangle$ [37] which have (to first order) the same magnetic moment and mass and possess highly-suppressed hyperfine state changing collisions due to coinciding values of the singlet and triplet scattering lengths in ^{87}Rb [47, 48]. This near-equivalence of the scattering lengths provides a highly stable system useful for experiments. In homonuclear mixtures, electromagnetic fields can be used to drive transitions between

the different internal states. In this system, we can consider the different components as the dressed eigenstates.

For a two-level system with resonant coupling between the two states, the 1D pseudospinor GPE (in the rotating frame) takes the form,

$$\begin{aligned} i\hbar\frac{\partial\psi_1}{\partial t} &= \Big[-\frac{\hbar^2}{2m}\frac{\partial^2}{\partial x^2} + V(x) + g_{11}^{1D}|\psi_1|^2 + g_{12}^{1D}|\psi_2|^2\Big]\psi_1 + \frac{\hbar}{2}\Omega\psi_2 \\ i\hbar\frac{\partial\psi_2}{\partial t} &= \Big[-\frac{\hbar^2}{2m}\frac{\partial^2}{\partial x^2} + V(x) + g_{21}^{1D}|\psi_1|^2 + g_{22}^{1D}|\psi_2|^2\Big]\psi_2 + \frac{\hbar}{2}\Omega\psi_1, \end{aligned} \tag{2.57}$$

where Ω denotes the Rabi frequency used to couple the states ψ_1 and ψ_2 and all states experience the same potential and chemical potential. In order to generalise the above equations to an M-component pseudospinor (again assuming resonant couplings and in the rotating frame) [49], let it be written as

$$i\hbar\frac{\partial\psi_j}{\partial t} = -\frac{\hbar^2}{2m}\frac{\partial^2\psi_j}{\partial x^2} + \sum_k\left(g_{jk}^{1D}|\psi_k|^2\psi_j + \frac{\hbar\Omega_{jk}}{2}\psi_k\right), \tag{2.58}$$

where $j,k \in \{1,2,\ldots,M\}$ and $g_{jk}^{1D} = 2\hbar\omega_r a_{jk}$ (where a_{jk} denotes the s-wave scattering length between components j and k). Importantly, when the system has $g_{jk}^{1D} = 1\forall\, j,k$ and $\Omega_{jk} = 0\forall\, j,k$ the equations are integrable. This widely studied system is known as the Manakov system [50]. One can see that in this case the nonlinearity in each component is proportional to the total density (meaning an equal sum of each individual component density). For equal nonlinearity in each component and general Ω, integrability can still be present depending on further conditions on Ω. This will discussed in Chapter 4.

The new degrees of freedom present in the pseudospinor systems accommodate the presence of types of soliton phenomena which cannot occur in the one component case. This includes two component solitons of bright-bright/dark-dark dark-bright and bright-dark type. The bright-bright and bright-dark solitons occur when the interactions are all attractive and the dark-dark and dark-bright solitons when they are all repulsive. Furthermore, when the intra- and inter-species scattering lengths are unequal other types of soliton complexes are known to exist; such as the dark-anti-dark soliton. It is worth pointing out that when the intra- and inter-species scattering lengths are unequal, one would expect width oscillations to occur [51] as a manifestation of the non-integrability. Also, beating can occur in the symmetric case of equal scattering

lengths when different solitons form in the system with different effective eigenfrequencies (chemical potentials) associated with effective potential wells [52, 53]. The beating frequency is equal to the difference in the effective eigenfrequencies.

2.3.3 The spinor Gross–Pitaevskii equation

As well as the pseudospinor BECs, there are the spinor BECs in which one can optically trap all $2F+1$ sublevels of a bosonic species and have spin-dependent as well as spin-independent collisions in the system. The equations for the $F = 1$ 1DGPE is

$$\begin{aligned} i\partial_t\psi_{\pm1} = &\left[-\frac{1}{2}\frac{\partial^2}{\partial x^2} + V(x) + \mathrm{sgn}(\lambda_s)\left(|\psi_{-1}|^2 + |\psi_0|^2 + |\psi_{+1}|^2\right)\right]\psi_{\pm1} \qquad (2.59a)\\ &+ (\lambda_a/|\lambda_s|)\left(|\psi_{\pm1}|^2 + |\psi_0|^2 - |\psi_{\mp1}|^2\right)\psi_{\pm1} + (\lambda_a/|\lambda_s|)\psi_0^2\psi_{\mp1}^*\\ i\partial_t\psi_0 = &\left[-\frac{1}{2}\frac{\partial^2}{\partial x^2} + V(x) + \mathrm{sgn}(\lambda_s)\left(|\psi_{-1}|^2 + |\psi_0|^2 + |\psi_{+1}|^2\right)\right]\psi_0 \qquad (2.59b)\\ &+ (\lambda_a/|\lambda_s|)\left(|\psi_{+1}|^2 + |\psi_{-1}|^2\right)\psi_0 + 2(\lambda_a/|\lambda_s|)\psi_{-1}\psi_0^*\psi_{+1}, \end{aligned}$$

where $\lambda_s = (a_0 + 2a_2)/3$ and $\lambda_a = (a_0 - a_2)/3$ denote the spin-independent and the spin-dependent collisions, respectively and a_F denotes the scattering length in the F total spin channel. If one assumes that $\lambda_s \gg \lambda_a$ (ie. $a_0 \approx a_2$), then the system reduces to the integrable Manakov system (for $V(x) = 0$)

$$i\partial_t\psi_m = \left[-\frac{1}{2}\frac{\partial^2}{\partial x^2} + V(x) + \mathrm{sgn}(\lambda_s)\left(|\psi_{-1}|^2 + |\psi_0|^2 + |\psi_{+1}|^2\right)\right]\psi_m, \qquad (2.60)$$

where $m \in \{+1, -1, 0\}$.

Table 2.1 shows the values of $\lambda_a/|\lambda_s|$ for different $F = 1$ alkali spinor gases from values of a_0 and a_2 taken from [45]. If $\lambda_a/|\lambda_s| < 0$ then the spinor gas is of a ferromagnetic nature and if $\lambda_a/|\lambda_s| > 0$ it is of a polar nature. If $\lambda_a/|\lambda_s|$ is sufficiently small then the system can to some extent be considered pseudospinor.

In [54] transitions between different Zeeman sublevels were induced by applying radio frequency (rf) sweeps assuming the application of a magnetic bias field. A two component BEC is formed by applying an initial pulse between $|1,-1\rangle$ and $|1,0\rangle$. Then dark-bright (DB) solitons are formed by applying a weak magnetic field gradient (as the states possess different magnetic moments).

$F=1$ species	$\lambda_a/\lvert\lambda_s\rvert$
^{7}Li	-0.45
^{23}Na	0.03
^{41}K	-0.03
^{87}Rb	-0.005

Table 2.1: The table shows the values of $\lambda_a/|\lambda_s|$ for different species of $F=1$ spinor alkali gases.

After a further rf pulse from $|1,0\rangle$ to $|1,1\rangle$, three component solitons are formed of the DBB type.

2.3.4 The non-polynomial Gross–Pitaevskii equation

The non-polynomial GPE arises as a natural way to account for the three-dimensional effects of soliton motion [55]. In order to reduce the GPE to its one-dimensional form, one assumes an ansatz where the transverse wavefunction takes the form of a Gaussian distribution. The validity of this ansatz rests on the assumption that the transverse behaviour is dominated by the harmonic confinement potential thus the trapping frequency is large and the density is low. The non-polynomial GPE can be derived by taking the width of this function as a degree of freedom and finding its dynamical equation. Therefore, the radial wavefunction is still taken to be a Gaussian but the width is allowed to become a dynamical variable which depends on the axial density of the condensate.

Let us work in the same soliton units and re-write the three-dimensional GPE, assuming a waveguide configuration ($\omega_x = 0$), in cylindrical co-ordinates (x, r, ϕ)

$$i\frac{\partial\Psi}{\partial t} = \left(-\frac{\nabla^2}{2} + V_b(x) + \frac{\omega_r^2}{2}r^2 - \frac{2\pi}{\omega_r}|\Psi|^2\right)\Psi. \tag{2.61}$$

The Lagrangian density is

$$\begin{aligned}\mathcal{L} = &\frac{i}{2}(\Psi^*\partial_t\Psi - \Psi\partial_t\Psi^*) - \frac{1}{2}|\nabla\Psi|^2 \\ &- V_b(x)|\Psi|^2 - \frac{\omega_r^2}{2}r^2|\Psi|^2 - \frac{\pi}{\omega_r}|\Psi|^4\end{aligned}$$

Inserting the following ansätze

$$\Psi(r,x) = \phi(r)\psi(x)$$
$$\phi(r) = \pi^{-1/2}\sigma^{-1}\exp(-r^2/[2\sigma^2])$$

results in, upon integrating over the radial direction, the Lagrangian density

$$\mathcal{L} = \frac{i}{2}(\psi^*\partial_t\psi - \psi\partial_t\psi^*) - \frac{1}{2}|\partial_x\psi|^2 - \frac{1}{2}\sigma^{-2}|\psi|^2$$
$$-\frac{\omega_r^2}{2}\sigma^2|\psi|^2 - V(x)|\psi|^2 + \frac{1}{2\omega_r\sigma^2}|\psi|^4.$$

Finding the resulting Euler-Lagrange equations from the above Lagrangian density gives the following equations of motion

$$i\frac{\partial\psi}{\partial t} = \left(-\frac{1}{2}\frac{\partial^2}{\partial x^2}\psi + V_b(x) + \frac{1}{\sigma^2} + \frac{\omega_r^2\sigma^2}{2} - \frac{|\psi|^2}{\omega_r\sigma^2}\right)\psi \tag{2.62}$$
$$\sigma^2 = \omega_r^{-1}\sqrt{1-\omega_r^{-1}|\psi|^2}. \tag{2.63}$$

Thus one arrives at the non-polynomial GPE

$$i\frac{\partial\psi}{\partial t} = \left[-\frac{1}{2}\frac{\partial^2}{\partial x^2}\psi + V_b(x) + \frac{\omega_r}{2}\left(\sqrt{1-\omega_r^{-1}|\psi|^2} + \frac{1}{\sqrt{1-\omega_r^{-1}|\psi|^2}}\right) - \frac{|\psi|^2}{\sqrt{1-\omega_r^{-1}|\psi|^2}}\right]\psi. \tag{2.64}$$

Thus the proximity to collapse is parameterised by ω_r. A consequence of using the soliton units system is that the dimensionless value of ω_r is inversely related to its dimensional value. This is because the units system is one in which $|g_{1D}|N = 1$ and $g_{1D} = 2\hbar\omega_r a_s$. In other words, if the radial trapping frequency is increased, then for g_{1D} to remain constant then $|a_s|$ must be accordingly decreased. The dimensionless collapse constant, k, defined as

$$k = \frac{N|a_s|}{\widetilde{a}_r} = \frac{N|g_{1D}|}{2}\sqrt{\frac{m}{\hbar^3\widetilde{\omega}_r}}, \tag{2.65}$$

gives in the soliton units

$$k = \frac{a_r}{2} = \frac{1}{2\sqrt{\omega_r}}, \tag{2.66}$$

where $a_r = 1/\sqrt{\omega_r}$ in dimensionless units. $k_c = 2/3$ is the dimensionless collapse constant for the NPGPE and so $\omega_r > 9/16$ is the condition for collapse to not occur in this formulation.

The utility of the non-polynomial is that it can extend the phenomenology encompassed by the 1DGPE by allowing a collapse of the condensate due to the attractive interactions [56]. This is important because the soliton exists in a quasi-1D limit due to the confinement in the radial directions freezing out the degrees of freedom in this domain and restricting the condensate to move freely in the axial direction under the support against dispersion arising from the nonlinear interaction. However, the bright soliton is formed when the interactions are attractive and so if the confinement is too high, the condensate is susceptible to collapse. The non-polynomial GPE is simpler to deal with than the fully three-dimensional GPE in both an analytical sense as well as for simulations of soliton motion.

This framework can be extended to the multiple component GPE [57]. Using the same approach as the 1D case, one arrives at the Lagrangian density for the quasi-1D binary condensate in dimensionless units

$$\begin{aligned}\mathcal{L} =& \frac{i}{2}\left[(\psi_1^*\partial_t\psi_1 - \psi_1\partial_t\psi_1^*) + (\psi_2^*\partial_t\psi_2 - \psi_2\partial_t\psi_2^*)\right] - \frac{1}{2}\left[|\partial_x\psi_1|^2 + |\partial_x\psi_2|^2\right] \\ &- \frac{1}{2}\left[\sigma_1^{-2}|\psi_1|^2 + \sigma_2^{-2}|\psi_2|^2\right] - \frac{\omega_r^2}{2}\left[\sigma_1^2|\psi_1|^2 + \sigma_2^2|\psi_2|^2\right] \\ &- \left(\frac{\omega_x^2x^2}{2} + V(x)\right)\left[|\psi_1|^2 + |\psi_2|^2\right] + \frac{a_r^2}{2\sigma_1^2}|\psi_1|^4 + \frac{g_b a_r^2}{2\sigma_2^2}|\psi_2|^4 + \frac{2g_a a_r^2}{(\sigma_1^2+\sigma_2^2)}|\psi_1|^2|\psi_2|^2,\end{aligned}$$

with $g_a \equiv g_{12}^{1D}/g_{11}^{1D}$, $g_b \equiv g_{22}^{1D}/g_{11}^{1D}$, $g_{11}^{1D} < 0$ and g_{11}^{1D}, g_{12}^{1D} & g_{22}^{1D} are defined in Eq. (2.57). The Euler-Lagrange equations for the four variables, ψ_1^*, ψ_2^*, σ_1 and σ_2, give:

$$\begin{aligned} i\partial_t\psi_1 =& -(\partial_{xx}/2)\psi_1 + (\omega_x^2x^2/2)\psi_1 + V(x)\psi_1 + (\omega_r^2\sigma_1^2/2)\psi_1 + (\sigma_1^{-2}/2)\psi_1 \\ &- a_r^2(\sigma_1^{-2}|\psi_1|^2 + 2(\sigma_1^2+\sigma_2^2)^{-1}g_a|\psi_2|^2)\psi_1 \qquad (2.67a) \\ i\partial_t\psi_2 =& -(\partial_{xx}/2)\psi_2 + (\omega_x^2x^2/2)\psi_2 + V(x)\psi_2 + (\omega_r^2\sigma_2^2/2)\psi_2 + (\sigma_2^{-2}/2)\psi_2 \\ &- a_r^2(\sigma_2^{-2}g_b|\psi_2|^2 + 2(\sigma_1^2+\sigma_2^2)^{-1}g_a|\psi_1|^2)\psi_2 \qquad (2.67b) \\ |\psi_1|^2 - a_r^2|\psi_1|^4 =& \sigma_1^4(\omega_r^2|\psi_1|^2 + 4(\sigma_1^2+\sigma_2^2)^{-2}g_a|\psi_1|^2|\psi_2|^2) \qquad (2.67c) \\ |\psi_2|^2 - a_r^2g_b|\psi_2|^4 =& \sigma_2^4(\omega_r^2|\psi_2|^2 + 4(\sigma_1^2+\sigma_2^2)^{-2}g_a|\psi_1|^2|\psi_2|^2) \qquad (2.67d)\end{aligned}$$

Equations (2.67c & 2.67d) can be substituted back into Eqs. (2.67a & 2.67b) for the case of $g_a = g_b = 1$ and can also be solved for two independent NPGPEs for the trivial un-coupled ($g_a = 0$) case. However, in the above form, they are difficult to implement numerically.

2.3.5 Other Gross–Pitaevskii type equations

The Gross–Pitaevskii equation proves to be very useful in the theory of ultracold quantum systems due to its relative simplicity and ability to offer insights into many different behaviours in this field. However, one must take care to bear in mind its limitations. The GPE is a non-relativistic mean field equation which describes bosonic contact interactions in the low energy limit for a system in which there is a majority occupation of a single quantum state. Therefore we expect the equation to not be applicable to systems where there is significant deviation from these assumptions. In the following equations, the term H_{GP} denotes the standard GPE Hamiltonian in units with $\hbar = m = |g|N = 1$

$$H_{\mathrm{GP}} \equiv -\frac{\nabla^2}{2} + V + \mathrm{sgn}(g)|\Psi|^2. \tag{2.68}$$

In the study of dilute atomic Bose gases, one normally assumes that interactions are dominated by s-wave collisions which effectively allows one to replace the interaction potential term, $U(\vec{r}-\vec{r}')$ in the many-body Hamiltonian Eq. (2.46) with a δ-potential. However, in some species, the dipolar moment of the electron is non-negligible (also the effect can be made dominant by tuning of the s-wave interaction) and results in a dipolar interaction term. In a polarised system, the interaction potential is of the form,

$$U(\vec{r}-\vec{r}') = c_{dd}\frac{1-3\cos^2\theta}{|\vec{r}-\vec{r}'|^3}, \tag{2.69}$$

giving a non-local form of the GPE

$$i\partial_t\Psi(\vec{r},t) = \left(H_{\mathrm{GP}} + \int \mathrm{d}\vec{r}'\, c_{dd}\frac{1-3\cos^2\theta}{|\vec{r}-\vec{r}'|^3}|\Psi(\vec{r}',t)|^2\right)\Psi(\vec{r},t). \tag{2.70}$$

Interestingly, the strength and sign of the dipole interaction can be tuned similar to the tunability of the scattering length by means of the Feshbach resonance. The method uses a time-dependent electromagnetic field to create an effective time-averaged potential dependent on a factor of a second angle, ϕ as $(3\cos^2\phi - 1)/2$ [58].

Many variations in the form of the GPE arise from attempts to incorporate the effects of the non-condensed fraction. This can be done in the form of a phenomenological damping where the Hamiltonian operator includes an imagin-

ary (thus decaying) term. The decay term term can take the form of a position-dependent or a position-independent term. Assuming some terms to be negligible, one can formulate a Langevin equation where the thermal cloud is close enough to equilibrium that it can be considered as a heat bath. In the [59] the decay term is proportional to H_{GP}, the standard GPE Hamiltonian, and the form of the GPE becomes

$$i\partial_t \Psi = (1 - i\gamma)\left(H_{\mathrm{GP}} - \mu\right)\Psi, \tag{2.71}$$

where $\gamma = i(\beta/4)\hbar\Sigma^K(\vec{r})$ and $\Sigma^K(\vec{r})$ is the time-independent Keldysh self-energy describing the effect of thermal decoherence caused by incoherent collisions between the condensate and the non-condensate atoms. Similar types of equations have been used to study dark soliton decay [60]. One can also include a phenomenological damping constant on the left hand side of the GPE [61] to give

$$(i - \gamma)\partial_t \Psi = \left(H_{\mathrm{GP}} - \mu\right)\Psi. \tag{2.72}$$

2.4 Solitons

In this section I will outline the previous research done on the subject of solitons in BECs paying particular attention to the relevant topic of bright solitons in quasi-1D condensates. Let us first reiterate the definition of the term soliton as the solution to an integrable nonlinear equation which moves with constant form and remains intact after collisions with other solitons. There are many different phenomena which are termed solitons and they occur in many different areas of the physical sciences. Wave behaviours in diverse fields such as quantum field theory, hydrodynamics, nonlinear optics and the ultracold atomic gases can be described by equations which yield solitons as possible solutions. A further pertinent distinction is the topological soliton (or topological defect) which arises in some systems and can be defined as being unremovable through continuous deformation and categorised according to its topological charge and homotopy group [62].

2.4.1 Types of soliton

In the simple model of the one-dimensional nonlinear Schrödinger equation (NLSE), there are two types of soliton arising from the different possible parities of the quadratic nonlinear term. Let the equation be written in dimensionless form as

$$i\frac{\partial\psi}{\partial t} = -\frac{1}{2}\frac{\partial^2\psi}{\partial x^2} + \kappa|\psi|^2\psi, \tag{2.73}$$

where κ takes the value of either -1 or +1. In this equation, a bright soliton can exists when $\kappa = -1$ representing an attractive and thus focussing interaction; and a dark soliton can exists when $\kappa = +1$ representing a repulsive and thus defocussing interaction. For $\kappa = -1$, the bright soliton with a norm of 1 is found as

$$\psi_B = \frac{1}{2}\text{sech}\left(\frac{x - vt - x_0}{2}\right)\exp\left(i(vx - \nu t) + \theta_0\right) \tag{2.74}$$

where $\nu = v^2/2 - 1/8$ and θ_0 is an arbitrary phase. An important property of the bright soliton in the NLSE is Galilean invariance. That is the shape of the soliton is independent of its velocity.

For $\kappa = +1$, the dark soliton is found as

$$\psi_D = \left[\cos\phi\tanh\left(\sqrt{\mu_0\beta}\cos\phi(x - vt - x_0)\right) + i\sin\phi\right]\psi_{\text{bg}} \tag{2.75}$$

where θ_0 is an arbitrary phase and $\psi_{\text{bg}} = \sqrt{\mu_0}\exp\left(i(kx - \omega t + \theta_0)\right)$ is the stable background upon which the dark soliton is an excitation. ϕ is termed the soliton phase angle ($|\phi| < \pi/2$) and describes the darkness of the soliton (a classification is sometimes applied wherein $\phi = 0$ is labelled as the dark soliton and $\phi \neq 0$ is a grey soliton).

Furthermore, it is useful to note the vector NLSE

$$i\frac{\partial\Psi}{\partial t} = -\frac{1}{2}\frac{\partial^2\Psi}{\partial x^2} + \kappa(\Psi^\dagger\Psi)\Psi, \tag{2.76}$$

where $\Psi^\dagger = (\psi_1^*, \psi_2^*, \ldots, \psi_M^*)$. Eq. (2.76) is also integrable and has SU(M) symmetry (reducing to Eq. (2.73) with U(1) symmetry for $M = 1$). For $M \geq 2$, the equation is referred to as the M-component Manakov equation and can be useful as a model for BECs consisting of multiple components where the scattering lengths take similar values. Furthermore, there is an integrable equation for $M = 2$ known as the modified Manakov equation where the nonlinear coefficients possess the relation $g_{11}^{1D} = g_{21}^{1D} = -g_{12}^{1D} = -g_{22}^{1D}$ for Eq. (2.57) [63].

2.4.2 Bright solitons in the BEC

In order to form a bright soliton in a BEC, one has to have a condensate with attractive interactions in a trap. The attractive interactions offer a problem for the formation of a BEC as they favour the collapse of the condensate. Crucially, the presence of a trapping potential can stabilise the BEC against collapse by enabling a metastable width of the cloud up to a critical number. Under the influence of a prolate trap and with attractive interactions, one can form a BEC bright soliton when the number of atoms constituting the soliton is fewer than the critical number. Bright solitons can also exist in higher dimensions although they may become unstable in certain regimes. In a dipolar condensate, it is known that, when the dipole-dipole interactions are sufficiently stronger than the s-wave interactions, then bright soliton can be stabilised such that it can move freely in two dimensions [64]. Also, bright solitons can be stabilised under the influence of an optical lattice although, in this case the solitons can only move in the free direction [65]. It is also known that bright solitons can be stabilised in higher dimensions using using rapidly oscillating interaction strengths [66].

In order to find the stability bound on the atom number for the bright soliton, one can use a variety of approaches. The critical point can be expressed in the dimensionless form as $k < k_{\mathrm{c}}$ where

$$k = \frac{N a_r}{|a_s|} \tag{2.77a}$$

$$k_c = \frac{N_c a_r}{|a_s|}. \tag{2.77b}$$

Determined from a variational analysis in mean-field theory, the critical value beyond which the bright soliton loses metastability and becomes unstable to collapse is found to be [67]

$$k_{\mathrm{c}} = \frac{1}{3^{1/4}} \approx 0.76. \tag{2.78}$$

From analysis in the NPGPE, a value of $k_{\mathrm{c}} = 2/3$ [68] is found whereas from 3D simulations of the GPE, the critical value is found as $k_{\mathrm{c}} = (0.675 \pm 0.005)$ [69].

In the single species GPE, we have two types of soliton: the bright soliton is formed when the interaction (dictated by the s-wave scattering length) is negative and the dark soliton when it is positive. The ground state for the BEC in the case of the bright soliton is the soliton itself whereas for the dark soliton, it

is an excited state of the BEC where the uniform background upon which the dark soliton manifests is the ground state. Furthermore, when one considers the addition of an optical lattice, the curvature of the band structure produced appears as an altered kinetic energy term in the BEC. This can be quantified as an effective mass where a negative effective mass, near the top of the band, implies an anomalous dispersion. This dispersion, which imparts a focussing on the wavepacket, can then be counteracted by a repulsive interaction term. This leads to the phenomenon of gap solitons of the bright type for positive scattering length and dark type for negative scattering length. Bright gap solitons have been experimentally demonstrated in ^{87}Rb [70].

Multiple component BECs which can be described by multiple component Gross–Pitaevskii equations admit (under the simplification of equal scattering lengths for the intra- and inter-species collisions) soliton solutions such as dark-bright solitons. These have been experimentally observed in two component BECs where all interactions are repulsive but the bright soliton component is supported against collapse by its repulsion from the state which constitutes the dark soliton [71].

2.4.3 Soliton interferometry

One of the applications of soliton creation is for use in soliton interferometry. Solitons are desirable for this use due to the fact that they are non-dispersive and show macroscopic coherence. Solitons are split on narrow barriers in order to separate condensates into two local matter-waves. The two matter-waves can also be recombined on the narrow barriers. Experimentally, the condensate experiments happen in a three-dimensional trap which is sufficiently asymmetrical as to have a confinement frequency in one direction which is much lower than in the other two directions. Often, this trap is magnetic but purely optically confined condensates have been experimentally realised [40]. The solitons propagate and interact with a barrier in the axial direction which has a much smaller harmonic trapping frequency than in the transverse directions where the confining potential dominates the nonlinear term leading to a transverse spatial profile which resembles a Gaussian more than a hyperbolic secant shape. The barrier is usually produced with a far blue-detuned laser which

produces a repulsive potential with a Gaussian shape (as the barrier strength is proportional to the laser intensity). The formation of a narrow barrier is then achieved by focussing the laser beam as much as is experimentally possible.

Figure 2.1 shows the axial density profile of a soliton in a toroidal trap over time with a narrow barrier positioned at $x = 0$ and an incoming velocity v which results in the soliton being split into two solitons which subsequently pass and then recombine on the barrier (over a total duration 3τ where $\tau = L/2v$ is the time taken to cover half of the trap circumference L). In each panel, a phase is imparted of (a) 0, (b) $\pi/2$, (c) π and (d) $3\pi/2$; resulting in a second transmission of (a) 0, (b) 1/2, (c) 1, (d) 1/2.

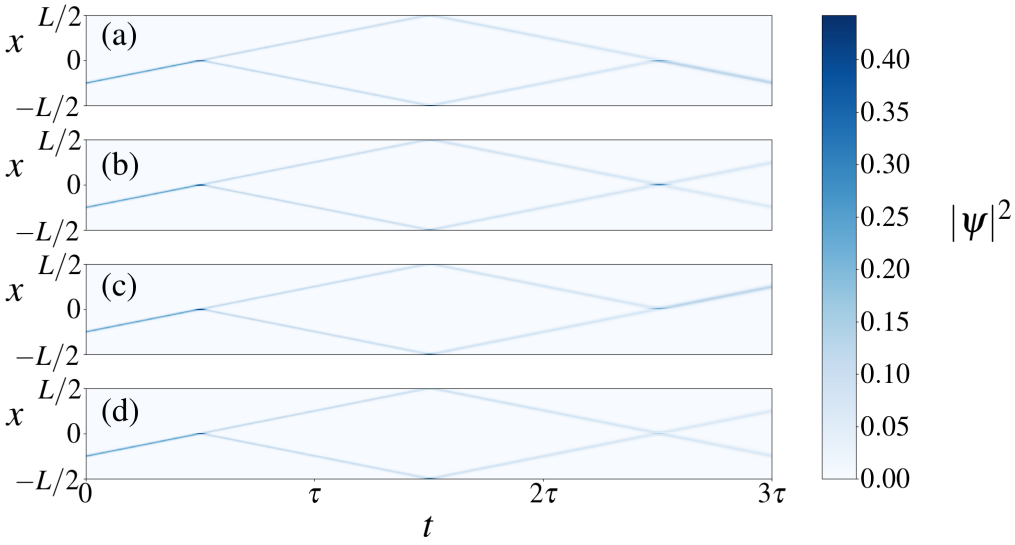

Figure 2.1: The figure shows data taken from single component simulations of the interferometry process (using the Fourier split-step method which inherently imposes a ring geometry) with an initial phase gradient of v . Each panel shows the axial density profile evolution encompassing an initial equal splitting and subsequent recombination with an imparted phase of (a) 0, (b) $\pi/2$, (c) π and (d) $3\pi/2$; resulting in a second transmission of (a) 0, (b) 1/2, (c) 1, (d) 1/2. $\tau = L/2v$ is the time taken for a soliton travelling with a velocity v to cover half of the trap circumference L.

In an experimental system, the soliton can be stabilised under sufficient transverse confinement but the dynamics in the radial direction can have an effect on the behaviour of the soliton, especially at critical times when the solitons collide on barriers, due to the high density. The issue of soliton stability be-

comes especially important for soliton collisions as there is a possibility that the overlap causes collapse or a breakdown of the 1D description - especially where the phase difference is such that interference is constructive, i.e. $-\pi/2 < \Delta\phi < \pi/2$. This could manifest as inelastic collisions (which do not occur in a fully 1D treatment). In order to model the soliton dynamics in these regimes, one can employ the non-polynomial Gross–Pitaevskii equation (see Sec. 2.3.4) or perform 3D simulations. In these cases, the transverse trapping frequency will appear as an additional parameter (in the dimensionless units). The result is that the soliton can undergo more splitting and recombination processes for a relative phase difference of $\phi = \pi$ than for $\phi = 0$ as the former results in a repulsive interaction whereas the latter results in an attractive interaction [72, 73]. Increasing the velocity of the solitons also increases their stability in barrier collisions.

2.4.4 Experimental progress

So far, experiments have produced bright solitons in ^{3}Li [74–76], ^{39}K [77], ^{85}Rb [78–80], ^{133}Cs [81]. In [79], interferometry was demonstrated using solitons which prolonged the operation of the system as an interferometer. In the Durham experiment [80] soliton interferometry was investigated for ^{85}Rb within an prolate harmonic trap with both a "narrow" and "wide" barrier, which have $1/e^2$ beam waists of 3.6 μm and 10.6 μm, respectively. In the soliton unit system, these correspond to Gaussian barriers with standard deviations of 1.9 and 5.7, respectively. In this experiment it was shown that for both widths of the barrier quantum tunnelling played a role in the transmission (of half) of the soliton population; however, the transmitted and reflected solitons possessed slight differences in their outgoing kinetic energies indicating a velocity filtering effect. This is where the two daughter solitons possess different velocities with the transmitted portion having a greater velocity. This indicates that the portion of the population which passes the barrier is taken from the higher velocity part of a finite momentum distribution rather than a quantum tunnelling process wherein a random amount of atoms passes the barrier, which is classically forbidden.

2.5 Numerical techniques

2.5.1 Fourier split step method

The equation describing the time evolution of the solitons is the Gross–Pitaevskii equation. This can be solved computationally by implementing a Fourier split step method (FSSM). The premise of the FSSM is that the Schrödinger equation can be split into two parts. The first part of the equation is the momentum term which represents a dispersion and the second term is the potential term which, in the case of the GPE contains the external potential (which often consists of a trapping potential and a barrier potential) as well as the non-linear term. The usefulness of this is that the equation can be alternately time-evolved in position and momentum space by employing a fast Fourier transform (FFT) algorithm to the momentum term. The GPE is propagated in time by applying a series of exponentials with imaginary arguments and so the norm of ψ is necessarily conserved (which is not the case when the FSSM is used to evolve in imaginary time). One must realise that, when this method is employed in order to solve a linear Schrödinger equation, the reason that solutions are not exact is that $[\hat{x}, \hat{p}] = i\hbar$ and so the operators do not commute. A time-step from t to $t + \delta t$ can be carried out by

$$\psi(t + \delta t) = e^{-i\delta t(T+V)}\psi(t),$$

where T and V denote the kinetic and potential terms, respectively, in the Hamiltonian and it is assumed that a system of units is being used in which $\hbar = 1$ and δt represents a small time increment. This is not equivalent to the following:

$$\psi(t + \delta t) = e^{-i\delta tT}e^{-i\delta tV}\psi(t).$$

A way to get around this problem is to take into account the non-commutativity of the operators and find a combination of the exponentials (which, when applied to the wavefunction at a time t, propagate the wavefunction in time by an amount δt) which minimises the error arising from this inequality. In other words, the combination of exponentials is chosen which removes the higher order terms in δt up to n^{th} order from the Baker–Campbell–Hausdorff formula for the minimum number of exponentials. This will quickly become more com-

plicated as the error is decreased from $\mathcal{O}(\delta t^n)$ to $\mathcal{O}(\delta t^{n+1})$. The simplest symmetric combination (at $\mathcal{O}(\delta t^3)$) is:

$$\psi(t+\delta t) = e^{-i\delta tT/2} e^{-i\delta tV} e^{-i\delta tT/2} \psi(t),$$

which is, in terms of minimising the error, equivalent to:

$$\psi(t+\delta t) = e^{-i\delta tV/2} e^{-i\delta tT} e^{-i\delta tV/2} \psi(t),$$

as the approach used is for any general set of operators and so the mathematical treatment is not different for $T \longleftrightarrow V$. For the $\mathcal{O}(\delta t^5)$ update, the minimum combination of exponentials which gives this error is [82]:

$$e^{-i\delta twT/2} e^{-i\delta twV} e^{-i\delta t(1-w)T/2} e^{-i\delta t(1-2w)V} e^{-i\delta t(1-w)T/2} e^{-i\delta twV} e^{-i\delta twT/2},$$

where w satisfies the conditions:

$$2w^3 + (1-2w)^3 = 0 \tag{2.79}$$
$$w \in \mathbb{R}$$

Therefore $w = (2 + 2^{\frac{1}{3}} + 2^{-\frac{1}{3}})/3$. Another factor which must be taken into consideration is whether the additional accuracy obtained from increasing n is justified by the additional computation time. For example, for short integration times, the optimal value of n may be 7 whereas for integration times which are sufficiently large, 5 could become the optimal value of n. The $\mathcal{O}(\delta t^4)$ splitting results in coefficients in the splitting which are not necessarily real (in other words, complex numbers which would not guarantee unitary time-evolution operators which ensure norm preservation) and also gives only one less exponential than the $\mathcal{O}(\delta t^5)$ splitting. Only the odd splittings are generally considered. For the study of the creation of subwavelength barriers using the spatially-varying Λ-system, the optimal value of n could also be reduced due to the extra time required to perform matrix operations.

Another consideration necessary when using the FSSM to solve the GPE is that the non-linear term is included by treating the norm of the wavefunction as a potential. An analysis has been carried out in [83] to determine that the best way to incorporate the norm of the wavefunction in the algorithm is to always use its most recent update whenever the potential energy is present. Therefore, the wavefunction can be grouped with the potential energy in the FSSM

algorithm and preserve the order of the error term which applies to the linear Schrödinger equation. This means that the best way to time evolve the wavefunction is not (using the $\mathcal{O}(\delta t^5)$ combination of exponentials),

$$\psi(t+\delta t) = e^{-i\delta t w T/2} e^{-i\delta t w V(|\psi(t)|^2,x)} e^{-i\delta t(1-w)T/2} e^{-i\delta t(1-2w)V(|\psi(t)|^2,x)} \times e^{-i\delta t(1-w)T/2} e^{-i\delta t w V(|\psi(t)|^2,x)} e^{-i\delta t w T/2} \psi(t).$$

The best way to update the wavefunction is,

$$\begin{aligned}
\psi_1 &= e^{-i\delta t w T/2}\psi(t) \\
\psi_2 &= e^{-i\delta t(1-w)T/2} e^{-i\delta t w V(|\psi_1|^2,x)}\psi_1 \\
\psi_3 &= e^{-i\delta t(1-w)T/2} e^{-i\delta t(1-2w)V(|\psi_2|^2,x)}\psi_2 \\
\psi(t+\delta t) &= e^{-i\delta t w T/2} e^{-i\delta t w V(|\psi_3|^2,x)}\psi_3.
\end{aligned}$$

As mentioned, the method can be applied to the vector GPE. For this situation, if one treats the classical fields as an M-component column vector, then one can treat the operator V as a $M \times M$ matrix (the kinetic energy is proportional to the identity matrix in this case). This does not introduce additional complexity into the scheme thus far elaborated since the operators are dealt with as if they do not commute. The added difficulty is encountered when evaluating the exponential of V. In terms of the discretised spatial grid, working in momentum and position space means that the kinetic and potential operators, respectively, are diagonal even upon the inclusion of the nonlinear term. This still holds for the case of the multiple component GPE when the couplings arise from the interaction terms. In order to evaluate the potential term, one must diagonalise the potential so that the exponential,

$$\exp(-i\delta t\hat{V}) = \sum_{n=1}^{\infty} \frac{(-i\delta t\hat{V})^n}{n!}$$

can be evaluated as

$$\exp(-i\delta t\hat{V}) = U\exp(-i\delta t\hat{V}')U^\dagger = \mathrm{diag}(\exp(-i\delta t\hat{V}'_{11}), \ldots, \exp(-i\delta t\hat{V}'_{MM})),$$

where $\hat{V}'$ is diagonal. Separating linear and nonlinear parts of the potential, $\hat{V} = \hat{V}_l + \hat{V}_{nl}$, for the special case of where the nonlinearity is equal for all components, one can diagonalise $\hat{V}$ by diagonalising $\hat{V}_l$ as $\hat{V}_{nl}$ is proportional to the identity matrix. If V_{nl} is not proportional to the identity matrix then one can resort to numerical diagonalisation. See Sec. 4.8.3 for a more thorough evaluation of the difficulty in solving the system.

2.5.2 Imaginary time propagation

For some simulations of the GPE when the initial ground state is not known, one can find it by propagating an initial appropriate ansatz in imaginary time. The numerical procedure is similar to above with the added complication that the wavefunction must be renormalised after each step. Performing what is sometimes known as the Wick rotation ($t \to -i\tau$) on the Schrödinger equation, we obtain

$$\frac{\partial \psi}{\partial \tau} = H\psi, \tag{2.80}$$

Solving for $\psi(\tau + \delta\tau)$ in terms of $\psi(\tau)$gives

$$\psi(\tau + \delta\tau) = \exp(-H\tau)\psi(\tau). \tag{2.81}$$

If we repeatedly perform this evolution in imaginary time, we will minimise the chemical potential. One can see this by decomposing the function $\psi(\tau)$ into eigenfunctions of the GPE Hamiltonian and noting that those with the highest eigenvalues will decay the most rapidly. Note that we need to continually renormalise the wavefunction when propagating in imaginary time.

Chapter 3

Splitting of two-component solitary waves on potential barriers

3.1 Overview

In this chapter, we examine the conditions for the splitting of an incident two-component soliton, governed by a system of nonlinearly coupled GPEs, from collisions with a narrow splitting barrier. The situation under consideration is one with equal atomic masses and negative scattering lengths in the two components, with variable attractive interspecies coupling between the components (with no linear coupling between them - the interconversion would make splitting of a composite soliton into single-component ones impossible). For generality, in the analysis we take three separate values for the available scattering lengths in the system but perform systematic numerical simulations with equal intraspecies scattering lengths. We take this approach for various reasons: the limited extent to which the scattering lengths can be controlled independently, the crossover between the role of the population share and the intraspecies scattering length in fixing the amplitude of the soliton and the desire to constrain the amount of system parameters.

Previous works have addressed collisions of single-component solitons with potential barriers, typically represented by the ideal δ-function or a narrow Gaussian potential barrier, aiming to identify of the collisions as functions of the velocity of the incoming soliton and the barrier's height and width [84, 85].

As concerns the dynamics of two-component solitons, their intrinsic vibrations in free space were studied [51], as well as collisions between two solitons on a narrow Gaussian barrier added to the Manakov system [86]. Also, the scattering of dark-bright solitons by impurities has been examined [87].

The objective of this work is to identify parameter regions in which the collision of the composite soliton with the barrier splits it into its single-component constituents. Control parameters considered below are the relative norm of the components, defined by the parameter f, the velocity of the incident soliton, v, the strength (area) ε of the barrier in Eq. (3.7), and the interspecies coupling (cross-attraction) strength g in Eqs. (3.8a) and (3.8b).

3.2 Coupled nonlinear Schrödinger equations in ultracold atomic physics and optical fibres – similarities and differences

In this section, I will present an overview into the types of nonlinear physics and soliton behaviour found in coupled nonlinear Schrödinger equations. Also, I will compare and contrast the likeness of nonlinear Schrödinger equations and soliton behaviour in the related system of optical fibres. The standard NLSE (previously mentioned in Sec. 2.3.2 and given by Eq. (2.73)) admits bright solitons and dark (grey) solitons depending on the signs of the nonlinearities (and also dispersion). Generalising the picture to encompass additional coupled components introduces further complexity. In these systems, again depending on the relationships between the increased number of nonlinear terms, more elaborate behaviour emerges. These new objects can take the form of symbiotic solitons; such as dark-bright solitons in a one-dimensional setting in which a bright soliton is supported against collapse by the effective potential well formed by is coupling to a dark soliton. In multiple dimensions coupled NLSE offer the possibility of solitons such as skyrmions [88].

If one replaces time in the coupled GPE by the propagation distance, z, the model applies to the bimodal light propagation in a Kerr-nonlinear waveguide with transverse coordinate x, while ψ_1 and ψ_2 are amplitudes of two com-

ponents of the electromagnetic wave, which correspond to different carrier wavelengths [89], and the potential represents transverse modulation of the refractive index. However, in this case the strength of the cross-interaction takes the single value, $g = 2$, as there is no straightforward optical counterpart of the Feshbach-resonance technique. Alternatively, if ψ_1 and ψ_2 represent the amplitudes of two waves with mutually orthogonal linear polarisations, the relevant value is $g = 2/3$, provided that rapidly oscillating four-wave-mixing terms may be neglected [89]. Interestingly, taking the case of $g = 2$, the coupled NLSE describing optical fibres with four-wave mixing terms is integrable for a special case. In a similar way to how one can generalise the NLSE (given by Eq. (2.73)) to the vector NLSE (given by Eq. (2.76)) by requiring that the field is generalised to multiple components whilst maintaining the same integrability structure (i.e. using group theory). Thus one can arrive at the pair-transition coupled NLSE

$$i\partial_t\psi_1 + (\partial_{xx}/2)\psi_1 - \kappa(|\psi_1|^2\psi_1 + 2|\psi_2|^2\psi_1 - \psi_1^*\psi_2^2) = 0 \tag{3.1}$$

$$i\partial_t\psi_2 + (\partial_{xx}/2)\psi_2 - \kappa(|\psi_2|^2\psi_2 + 2|\psi_1|^2\psi_2 - \psi_2^*\psi_1^2) = 0, \tag{3.2}$$

which is integrable [90, 91].

In atomic BECs, one can linearly couple the two components using alternating electric fields. The coupling strength is denoted by the Rabi frequency. If one has equal nonlinearities (i.e.- equal scattering lengths) then the system remains integrable in the dressed basis (the eigenbasis for the linear coupling terms). Forming a soliton in one of these dressed states, this technique can be used as an alternative to the Feshbach resonance to tune the strength of the nonlinearity by varying the Rabi frequency and detuning [92] in order to control the effective scattering properties of the mixed atomic state.

In atomic physics, a system similar to the coupled NLSE is that describing two component degenerate Fermi gases [93]. The distinction is that Pauli exclusion gives a weaker nonlinearity describing intra-species collisions, resulting in a polynomial density term of order 4/3, and with a quadratic density term for interspecies collisions. Similarly, a Bose–Fermi mixture gives similar nonlinear relationships to the coupled NLSE but with quadratic density dependent potentials for Bose–Bose and Bose–Fermi collisions and a quartic interaction potential for Fermi–Fermi collisions [94].

3.3 System details

We consider a two-component BEC system, where the components are provided by different internal states of the same atomic species, and collisions are dominated by low-energy s-wave scattering. We describe this system in terms of two coupled Gross–Pitaevskii equations, where the component atoms are radially confined by a far-off-resonant optical waveguide providing approximately harmonic trapping in the y and z directions, but are axially (x direction) relatively weakly confined, if at all. In addition, we impose an off-resonant sheet of light propagating perpendicular to the axial direction with peak beam strength E_{B} and an axial direction $1/e^2$ radius x_r, which provides a barrier potential for both components centred at $x = 0$ [80, 95]. We assume the off-resonant optical waveguide and barrier potentials to be insensitive to the atomic internal state, allowing the coupled Gross–Pitaevskii equations to take the form

$$\begin{aligned} \mathrm{i}\hbar\frac{\partial}{\partial t}\Psi_1(\vec{r}) = &\left[-\frac{\hbar^2\nabla^2}{2m} + V(x) + m\omega_r^2\frac{y^2+z^2}{2}\right]\Psi_1(\vec{r}) \\ &+ \frac{4\pi\hbar^2 N}{m}\left[a_{11}|\Psi_1(\vec{r})|^2 + a_{12}|\Psi_2(\vec{r})|^2\right]\Psi_1(\vec{r}), \qquad (3.3a) \\ \mathrm{i}\hbar\frac{\partial}{\partial t}\Psi_2(\vec{r}) = &\left[-\frac{\hbar^2\nabla^2}{2m} + V(x) + m\omega_r^2\frac{y^2+z^2}{2}\right]\Psi_2(\vec{r}) \\ &+ \frac{4\pi\hbar^2 N}{m}\left[a_{22}|\Psi_2(\vec{r})|^2 + a_{12}|\Psi_1(\vec{r})|^2\right]\Psi_2(\vec{r}), \qquad (3.3b) \end{aligned}$$

where m is the atomic mass, a_{11}, a_{22}, and a_{12} are the intra- and inter-species s-wave scattering lengths, $V(x) = m\omega_{\mathrm{T}}^2 x^2/2 + E_{\mathrm{B}}\mathrm{e}^{-2x^2/x_r^2}$ combines a weak harmonic axial trapping potential and the barrier potential, ω_{T} and ω_r are axial and radial harmonic frequencies, and N is the total particle number. Note that we have chosen the normalisation convention $\int \mathrm{d}\vec{r}\,|\Psi_1(\vec{r})|^2 = f$, $\int \mathrm{d}\vec{r}\,|\Psi_2(\vec{r})|^2 = 1-f$, such that

$$\int \mathrm{d}\vec{r}\left[|\Psi_1(\vec{r})|^2 + |\Psi_2(\vec{r})|^2\right] = 1, \qquad (3.4)$$

and the numbers of particles in the two components are given by $N_1 = fN$ and $N_2 = (1-f)N$.

Strong radial confinement then permits us to assume a Gaussian ansatz

$$\phi(y,z) = (m\omega_r/\pi\hbar)^{1/2}\exp(-m\omega_r[y^2+z^2]/2\hbar), \qquad (3.5)$$

for the radial degrees of freedom of the condensate wavefunctions $\Psi_1(\vec{r})$, $\Psi_2(\vec{r})$. We integrate over y and z, define $g_{11} \equiv 2\hbar\omega_r a_{11}$, and express the result in terms

of the previously defined soliton units system with unit position $\hbar^2/m|g_{11}|N$, unit time $\hbar^3/m(g_{11}N)^2$, and unit energy $m(g_{11}N/\hbar)^2$ [directly implying a unit velocity of $|g_{11}|N/\hbar$, and that after integration over y and z we effectively multiply the the condensate wavefunctions by $\hbar/(m|g_{11}|N)^{1/2}$ to render them dimensionless].[1] This yields

$$\mathrm{i}\frac{\partial}{\partial t}\psi_1(x) = \left[-\frac{1}{2}\frac{\partial^2}{\partial x^2} + \frac{\omega_x^2 x^2}{2} + \varepsilon\eta(x,\sigma)\right]\psi_1(x) - \left[|\psi_1(x)|^2 + g|\psi_2(x)|^2\right]\psi_1(x), \tag{3.6a}$$

$$\mathrm{i}\frac{\partial}{\partial t}\psi_2(x) = \left[-\frac{1}{2}\frac{\partial^2}{\partial x^2} + \frac{\omega_x^2 x^2}{2} + \varepsilon\eta(x,\sigma)\right]\psi_2(x) - \left[g'|\psi_2(x)|^2 + g|\psi_1(x)|^2\right]\psi_2(x), \tag{3.6b}$$

where $g = a_{12}/a_{11}$, $g' = a_{22}/a_{11}$, $\omega_x = \omega_{\mathrm{T}}\hbar^3/m|g_{11}|^2N^2$, $\varepsilon = E_{\mathrm{B}}x_r(\pi/2)^{1/2}/m^2|g_{11}|^3N^3$, $\sigma = x_r/2\hbar^2/m|g_{11}|N$, and

$$\eta(x,\sigma) = \frac{1}{\sqrt{2\pi}\sigma}\exp(-x^2/2\sigma^2), \tag{3.7}$$

such that $\lim_{\sigma\to 0}\eta(x,\sigma) = \delta(x)$, and we have assumed all the scattering lengths to be negative. Here $g \equiv a_{12}/a_{11}$ is the relative strength of the cross-attraction between the components, which can be effectively adjusted by means of the Feshbach-resonance technique [96–98], and $\varepsilon > 0$ is the strength (area) of the splitting barrier. Direct control of the properties of binary BECs has been demonstrated in [99] for a heteronuclear BEC and in [100] for a BEC consisting of different hyperfine states of the same species where the interspecies interaction was varied to probe the miscibility–immiscibility threshold. One must bear in mind that although it has become a fairly standard technique to control the scattering length in BEC systems, conventionally using magnetic Feshbach resonances, there are limitations as to what can be achieved in multicomponent BEC systems. For instance, when exploiting a magnetic Feshbach resonance, in principle all of the scattering lengths are dependent on the value of the applied magnetic field and therefore cannot be varied independently. Hence, the Feshbach resonance technique must be utilised in such a way that the three scattering lengths (in the two component system studied here) are brought as close as possible to their desired values. For the numerical results presented in Sec. 3.5 we have fixed $g' = 1$ (implying that $a_{11} = a_{22}$) and varied g. We point out

[1] This can be thought of heuristically as a units system where $\hbar = m = g_{11}N = 1$.

that in the particular case of $g = 0$, in the Gross–Pitaevskii treatment considered in this chapter, the value of g' has a role equivalent to that of f in that it defines the relative self-interaction strength of the two condensate components. Furthermore, there may be regimes where for example g can be controlled effectively independently in that the intraspecies scattering lengths remain close to their background values over relevant magnetic field strengths and $a_{11} \approx a_{22}$. The use of optical Feshbach resonance techniques may also be considered although in this case one would need to accept the large loss rates that typically accompany them [101, 102]. Another possibility is the use of laser-assisted magnetic Feshbach resonances [103]. To some extent one has a choice in the species used, with different species of atoms possessing different background scattering length values and different dependences on the applied fields for the different hyperfine states used.

To avoid duplication of results, we always assume $g'(1-f) \geq f \Rightarrow f \leq g'/(1+g')$, which effectively defines component 2 as being the component with the largest intraspecies mean-field attraction; put in terms of particle numbers and scattering lengths, we assume $N_1 a_{11} \leq N_2 a_{22}$. In the case where $g' = 1$ (i.e., $a_{22} = a_{11}$), this assumption reduces to $f \leq 1/2$ (i.e., $N_1 \leq N_2$); and in the case where $f = 1 - f = 1/2$ (i.e., $N_1 = N_2$), it reduces to $g' \geq 1$ ($a_{22} \geq a_{11}$). In our analytical treatment we choose in general to keep both f and g' as separate parameters that may be individually varied: changes in f corresponding to relative changes in the individual components' particle numbers; and changes in g' (and g) corresponding to changes in the (assumed negative) scattering lengths. We believe this to be a convenient and accurate representation of what may be altered experimentally in any practical BEC-based implementation, although we note that the core ideas presented in the next section can be straightforwardly understood in the simpler limiting case of $g' = 1$.

3.4 Analytical approach

3.4.1 Idealised system

Given that we are interested in a limit of weak axial confinement, and infinitesimally narrow barriers, we set $\omega_x = 0$ and $\sigma \to 0$ in Eq. (3.6). These combine to

produce the mathematically simpler and more tractable equations

$$\mathrm{i}\frac{\partial\psi_1}{\partial t} = \left[-\frac{1}{2}\frac{\partial^2}{\partial x^2} + \varepsilon\delta(x) - |\psi_1|^2 - g|\psi_2|^2\right]\psi_1, \tag{3.8a}$$

$$\mathrm{i}\frac{\partial\psi_2}{\partial t} = \left[-\frac{1}{2}\frac{\partial^2}{\partial x^2} + \varepsilon\delta(x) - g'|\psi_2|^2 - g|\psi_1|^2\right]\psi_2, \tag{3.8b}$$

which we assume various forms of in the remainder of this section.

Equation (3.8) can be generated from the classical field energy functional

$$\begin{aligned} H[\psi_1,\psi_1^*,\psi_2,\psi_2^*] = \int \mathrm{d}x \Bigg[& \frac{1}{2}\left(\left|\frac{\partial\psi_1}{\partial x}\right|^2 + \left|\frac{\partial\psi_2}{\partial x}\right|^2\right) \\ & - \frac{1}{2}\left(|\psi_1|^4 + g'|\psi_2|^4 + 2g|\psi_1|^2|\psi_2|^2\right) \\ & + \varepsilon\delta(x)\left(|\psi_1|^2 + |\psi_2|^2\right)\Bigg], \end{aligned} \tag{3.9}$$

which also yields the total (conserved) system energy in the mean-field treatment.

Setting aside the barrier potential (i.e., setting $\varepsilon = 0$), two exactly integrable cases present themselves. If $g = 0$, then Eq. (3.8) corresponds to two decoupled integrable NLSEs; and, if $g = g' = 1$, Eq. (3.8) then constitutes the integrable Manakov system [50]. More generally, the $g = -1$ case describing repulsive interspecies interactions is also exactly integrable, and it should also be noted that, even in the general attractive case where $g = g' = 1$ is not fulfilled, two-component bright soliton solutions, where both components have identical mode profiles proportional to $\mathrm{sech}(F[x-(x_0+vt)]/2)$ [i.e., of the same form as in Eq. (3.11)] if $f + (1-f)g = (1-f)g' + fg \equiv F$. This equality condition is equivalent to requiring $f = (g'-g)/(g'+1-2g)$, or, in terms of the more immediately physical quantities of particle numbers and (assumed negative) scattering lengths:

$$\frac{N_1}{N} = \frac{a_{12}-a_{22}}{2a_{12}-a_{11}-a_{22}}. \tag{3.10}$$

In summary, the existence of very well behaved regimes for certain parameter values provides scope for making use of perturbation theory in the regime of relatively small ε.

3.4.2 Limit of negligible interspecies interactions

We are interested in a solution of Eq. (3.8) with $g = 0$ (no interspecies interactions) consisting initially of a composite soliton of both species centred at the same point in space, i.e., such that the peak of both components of the composite soliton move according to $x_0 + vt$. Assuming the composite soliton to be located sufficiently far from the potential barrier for its influence to be considered negligible, this is given by

$$\psi_1(x,t) = \frac{f}{2}\exp\left(\mathrm{i}\left[vx - \mu_1 t\right]\right) \times \operatorname{sech}\left(\frac{f}{2}\left[x - (x_0 + vt)\right]\right), \tag{3.11a}$$

$$\psi_2(x,t) = \frac{(1-f)\sqrt{g'}}{2}\exp\left(\mathrm{i}\left[vx - \mu_2 t\right]\right) \times \operatorname{sech}\left(\frac{[1-f]g'}{2}\left[x - (x_0 + vt)\right]\right), \tag{3.11b}$$

with associated chemical potentials

$$\mu_1 = -f^2/8 + v^2/2, \tag{3.12a}$$

$$\mu_2 = -\left(1-f\right)^2 g'^2/8 + v^2/2. \tag{3.12b}$$

The centre-of-mass kinetic energies of each component (essentially half the total mass of the soliton multiplied by the square of the velocity with which it is moving) are given in terms of our unit energy $m(g_{11}N/\hbar)^2$ by:

$$(E_{\mathrm{kin}})_1 = f v^2/2, \tag{3.13a}$$

$$(E_{\mathrm{kin}})_2 = (1-f) v^2/2, \tag{3.13b}$$

and we determine the intraspecies interaction potential energies from terms on the second line of Eq. (3.9):

$$(E_{\mathrm{int}})_1 = -f^3/12, \tag{3.14a}$$

$$(E_{\mathrm{int}})_2 = -(1-f)^3 g'^2/12. \tag{3.14b}$$

The potential energy of each component associated with the weak potential barrier can be easily found in the framework of perturbation theory (with the parameter ε assumed to be sufficiently small), which neglects deformation of the soliton under the influence of the barrier potential [104]:

$$U_1(t) \equiv \varepsilon \int \mathrm{d}x\, \delta(x)\, |\psi_1(x,t)|^2$$

$$= \frac{1}{4}\varepsilon f^{\,2}\mathrm{sech}^2\left(\frac{f}{2}\left[x_0 + vt\right]\right), \tag{3.15a}$$

$$U_2(t) \equiv \varepsilon \int \mathrm{d}x\, \delta(x)\, |\psi_2(x,t)|^2$$

$$= \frac{1}{4}\varepsilon(1-f)^2 g' \mathrm{sech}^2\left(\frac{[1-f]g'}{2}\left[x_0 + vt\right]\right). \tag{3.15b}$$

The perturbation theory we have used applies (to each component) provided that the magnitudes of the interaction potential energies [Eq. (3.14)] dominate the peak values of the barrier potential energies, as determined by Eq. (3.15) when $x_0 + vt = 0$ ($\Rightarrow t = -x_0/v$). This gives the potential energy associated with the unmodified component solitons being located exactly on top of the barrier,

$$(U_{\max})_1 = \varepsilon f^2/4, \tag{3.16a}$$

$$(U_{\max})_2 = \varepsilon(1-f)^2 g'/4, \tag{3.16b}$$

which, compared with Eq. (3.14), reveals the condition for sufficiently small ε to be

$$\varepsilon \ll f/3. \tag{3.17}$$

In the $g = 0$ case we are considering, we can reasonably estimate that each component transmits through the barrier under the condition that the respective peak potential energy, as given by Eq. (3.16), is exceeded by that component's centre-of-mass kinetic energy (note that this is based on classical energy considerations). Combining the results of Eq. (3.13) and Eq. (3.16) therefore results in the conditions

$$v^2 > \varepsilon f/2, \tag{3.18a}$$

$$v^2 > \varepsilon(1-f)g'/2, \tag{3.18b}$$

for components 1 and 2, respectively, to be transmitted. We therefore predict an incident composite soliton to be split into a pair of transmitted component 1 and reflected component 2 solitons within the following interval of velocities:

$$\sqrt{\varepsilon f/2} < |v| < \sqrt{\varepsilon(1-f)g'/2} \tag{3.19}$$

[recall that we have previously assumed $f \leq (1-f)g'$ by definition]. We can reasonably expect the same prediction to be valid in the case of nonzero but weak interspecies attraction, $g \ll 1$.

3.4.3 Extension to the nonlinear splitter

It is relatively straightforward to extend the theoretical treatment to the case of a nonlinear splitter, as described in Refs. [105] and [106]. In these works this takes the form of a localized self-repulsive nonlinearity (this can be created by a tightly focused laser beam which locally applies an optical Feshbach resonance [107]). The equivalent modified system of Eq. (3.8) then becomes

$$i\frac{\partial\psi_1}{\partial t} = \left[-\frac{1}{2}\frac{\partial^2}{\partial x^2} + \varepsilon_{\rm nl}\delta(x)\left|\psi_1\right|^2 - |\psi_1|^2 - g|\psi_2|^2\right]\psi_1, \tag{3.20a}$$

$$i\frac{\partial\psi_2}{\partial t} = \left[-\frac{1}{2}\frac{\partial^2}{\partial x^2} + \varepsilon'_{\rm nl}\delta(x)\left|\psi_2\right|^2 - g'|\psi_2|^2 - g|\psi_1|^2\right]\psi_2, \tag{3.20b}$$

where $\varepsilon_{\rm nl}$ and $\varepsilon'_{\rm nl}$ both > 0 quantify the strengths of the nonlinear splitters, which in principle should be considered distinct for the two atomic species.

Similarly to the linear case, when $g \ll 0$ one can determine velocity intervals in which we predict splitting of an incident composite soliton into a lighter transmitted soliton and a heavier reflected soliton:

$$\sqrt{\varepsilon_{\rm nl} f^3}/4 < |v| < g'\sqrt{\varepsilon'_{\rm nl}(1-f)^3}/4. \tag{3.21}$$

Note that the form of this interval implicitly assumes $f^{3/2} \leq g'(1-f)^{3/2}(\varepsilon'_{\rm nl}/\varepsilon_{\rm nl})^{1/2}$, which is only automatically fulfilled by the previously assumed condition that $f \leq (1-f)g'$ when $g'(\varepsilon'_{\rm nl}/\varepsilon_{\rm nl})^{1/2} \leq 1$. In the case of $g' = 8$ and $f = 13/15$ (with $\varepsilon'_{\rm nl} = \varepsilon_{\rm nl}$), for example, the upper and lower bounds of Eq. (3.21) would need to be transposed.

We can readily determine nonlinear equivalents to Eq. (3.16)

$$(U_{\max\,\rm nl})_1 = \varepsilon_{\rm nl} f^4/32, \tag{3.22a}$$

$$(U_{\max\,\rm nl})_2 = \varepsilon'_{\rm nl}(1-f)^4 g'^2/32, \tag{3.22b}$$

which, compared with Eq. (3.14), reveals the condition for sufficiently small $\varepsilon_{\rm nl}$ is that it should be significantly less than $8/3f$, where similarly $\varepsilon'_{\rm nl}$ should be significantly less than $8/3(1-f)$. If we consider $\varepsilon_{\rm nl}$ and $\varepsilon'_{\rm nl}$ to be broadly similar in magnitude, this may be simplified to setting the minimum of $\{\varepsilon_{\rm nl}, \varepsilon'_{\rm nl}\} \ll 8/3$.

Comparing Eq. (3.21) with Eq. (3.19), we see that the nonlinear splitter manifests much stronger dependence on the norm-distribution parameter $f =$

N_1/N, as well as a stronger dependence on the relative magnitude of the intraspecies scattering lengths $g' = a_{22}/a_{11}$. In the numerical analysis presented below, however, we address solely the case of the previously described linear splitter, which we believe would be experimentally more straightforward.

3.4.4 Limit of a strongly asymmetric two-component soliton

One can also carry out a perturbative analysis, assuming sufficiently small ε, on the case when the intraspecies mean field attraction of component 1 is much smaller than the interspecies mean field attraction of component 2 on component 1, i.e., $f \ll (1-f)g$, and also the intraspecies mean field attraction of component 2 is much greater than the interspecies mean field attraction of component 1 on component 2, i.e., $fg \ll (1-f)g'$. These conditions can be summarised as

$$\frac{f}{(1-f)} \ll g \ll \frac{g'(1-f)}{f}, \tag{3.23}$$

which simplify to $f/(1-f) \ll g \ll (1-f)/f$ when $g' = 1$, and to $1 \ll g \ll g'$ when $f = 1-f = 1/2$. In this case component 2 of the incident mode is essentially the usual NLSE bright soliton, as described by Eq. (3.11b) and Eq. (3.12b). We can then seek a solution describing component 1 having the form

$$\psi_1(x,t) = \exp\left(\mathrm{i}\left\{v x - \left[\mu_1^{(0)} + v^2/2\right] t\right\}\right) u_1\left(x - [x_0 - v t]\right), \tag{3.24}$$

with, subsequent to carrying out a change of variables such that $x - (x_0 - vt) \equiv X$, u_1 determined by a stationary linear Schrödinger equation:

$$\begin{aligned} \mu_1^{(0)} u_1(X) = &-\frac{1}{2}\frac{d^2}{dX^2} u_1(X) \\ &- \frac{g(1-f)^2 g'}{4} \operatorname{sech}^2\left(\frac{[1-f]g'}{2} X\right) u_1(X). \end{aligned} \tag{3.25}$$

This simply describes a one-dimensional Schrödinger particle in a Pöschl–Teller potential, which can be generally solved in terms of special functions.[2]

The exact ground-state solution to Eq. (3.25) and its corresponding eigenvalue are given by

$$u_1(X) = A_1 \left[\operatorname{sech}\left(\frac{[1-f]g'X}{2}\right)\right]^{\alpha}, \tag{3.26a}$$

[2]This is made substantially simpler upon implementing the change of variable $Y = (1-f)g'X$.

$$(\mu_1^{(0)})_{\text{ground}} = -\frac{[\alpha(1-f)g']^2}{8}, \tag{3.26b}$$

where

$$\alpha = \sqrt{\frac{1}{4} + \frac{2g}{g'}} - \frac{1}{2}. \tag{3.27}$$

The amplitude A_1 is [with respect to Eq. (3.25)] in principle arbitrary, however as we have already set the norm of component 1 to be f, these can be related to each other via

$$f \equiv \int dX |u_1(X)|^2 = A_1^2 \frac{2\sqrt{\pi}\,\Gamma(\alpha)}{(1-f)g'\,\Gamma(\alpha+1/2)}, \tag{3.28}$$

where Γ is the Gamma function.

One can also find the first (spatially odd) excited state produced by Eq. (3.25), alias the dipole mode:

$$u_1(x) = A_1 \sinh\left(\frac{1}{2}x\right)\left[\operatorname{sech}\left(\frac{1}{2}x\right)\right]^{\alpha}, \tag{3.29}$$

$$\left(\mu_1^{(0)}\right)_{\text{excited}} = -\frac{(\alpha-1)^2}{8}. \tag{3.30}$$

Unlike the ground state, which exists at all $g > 0$, the dipole mode exists only at $\alpha > 1$, i.e., according to Eq. (3.26a), at $g > 1$.

The kinetic energy, $(E_{\text{kin}})_1$, of component 1 is given by Eq. (3.13a), while the height of the energy barrier generated by the splitter, in similar fashion to Eq. (3.15a), can be determined from Eq. (3.28) to be

$$(U_{\max})_1 = \varepsilon A_1^2 = \frac{\varepsilon f(1-f)g'\,\Gamma(\alpha+1/2)}{2\sqrt{\pi}\,\Gamma(\alpha)}. \tag{3.31}$$

Combining these expressions within the energy condition for component 1 to be transmitted through the barrier, $(E_{\text{kin}})_1 > (U_{\max})_1$ [cf. Eq. (3.18a)], yields the following result:

$$v^2 > \frac{\varepsilon(1-f)g'\,\Gamma(\alpha+1/2)}{\sqrt{\pi}\,\Gamma(\alpha)}. \tag{3.32}$$

On the other hand, the condition for the reflection of component 2 remains, in the first approximation, the same as that given by Eq. (3.18b). Hence, this condition becomes $v^2 < v_2^2 \equiv \varepsilon g'(1-f)/2$, and there are intervals of velocities defined by

$$\sqrt{\frac{\varepsilon(1-f)g'\,\Gamma(\alpha+1/2)}{\sqrt{\pi}\,\Gamma(\alpha)}} < |v| < \sqrt{\frac{\varepsilon(1-f)g'}{2}} \tag{3.33}$$

[cf. Eq. (3.19)] in which collision of the incident composite soliton with the barrier leads to splitting, with component 1 transmitted and component 2 reflected. Note that when $\alpha = 1$ [revealed from Eq. (3.27) to be when $g/g' = 1$] it follows that $\sqrt{\pi}\,\Gamma(\alpha) = 2\,\Gamma(\alpha + 1/2)$, and the interval shrinks to nil; this, in particular, applies for the Manakov system, when $g = g' = 1$. For $g/g' > 1$ the situation inverts, and there is instead a velocity interval, defined by transposing the upper and lower bounds in Eq. (3.33), in which component 1 is reflected and component 2 transmitted.

It is important to note that in the limiting case of $g' = 1$, this regime is accessed purely by control of the relative particle numbers in each component, with component 1 having a much smaller population. While this is entirely reasonable within the Gross–Pitaevskii description, in any atomic physics realisation this runs the risk of component 1 being so small that it is difficult to image, or even of the particle numbers being so low that a Gross–Pitaevskii description is no longer valid.

Strictly speaking, there is an additional condition necessary for the complete collision-induced splitting in free space. The kinetic energy of the transmitted component must exceed its binding energy in the composite soliton, determined by the cross-attraction $E_{\rm cross} \equiv -g\int \mathrm{d}x\,|\psi_1(x)|^2|\psi_2(x)|^2$ [in this analysis we assume the smallness of ε means consideration of the energy described by Eq. (3.31) can be neglected altogether], otherwise component 1 will not become a free soliton. Hence, substituting in Eq. (3.11b) and Eq. (3.26a),

$$\begin{aligned} E_{\rm cross} &= -\,g A_1^2 \frac{(1-f)^2 g'}{4} \int \mathrm{d}X \left[\mathrm{sech}\left(\frac{[1-f]g'X}{2}\right)\right]^{2(\alpha+1)} \\ &= -\,g A_1^2 \frac{(1-f)\sqrt{\pi}\,\Gamma(\alpha+1)}{2\,\Gamma(\alpha+3/2)} \\ &= -\,\frac{\alpha g f (1-f)^2 g'}{2(2\alpha+1)}, \end{aligned} \tag{3.34}$$

where we have also made use of Eq. (3.28). Comparing the expressions of Eq. (3.13) and Eq. (3.34) via $(E_{\rm kin})_1 > |E_{\rm cross}|$ yields, finally, the condition

$$|v| > \sqrt{\frac{\alpha g (1-f)^2 g'}{(2\alpha+1)}}. \tag{3.35}$$

3.4.5 Numerical simulations

In our numerical simulations, we consider a Gaussian rather than a δ-function barrier, $V(x) = \varepsilon\eta(x,\sigma)$, as defined in Eq. (3.7). The intention here is to model an experimentally relevant Gaussian-profile off-resonant sheet of light, however in a formal sense this could also be considered a regularized approximation to a "true" δ-function with finite width σ. Except for Fig. 3.11, all of our numerical results in this chapter, when considering such a Gaussian barrier, are for $\sigma = 0.4$. As argued in [84], this can generally be considered a reasonable low value when taking experimental practicalities into account.

We numerically integrated Eqs. (3.8a) and (3.8b), including the potential barrier described by Eq. (3.7), by means of the well-known Fourier-transform split-step method [108, 109]. Typical examples of collisions with the barrier leading to either the splitting of two-component solitons, or their mutual passage through the barrier, are displayed in Figs. 3.1 and 3.2, respectively. These two examples were selected with slightly different collision velocities but otherwise identical parameter values, and correspond to situations close to the boundary between the presence and absence of splitting.

We quantify the transmission of the two components through the barrier by the coefficients

$$T_1 = f^{-1}\int_0^\infty \mathrm{d}x\,|\psi_1(x,t=t_f)|^2, \tag{3.36}$$

$$T_2 = (1-f)^{-1}\int_0^\infty \mathrm{d}x\,|\psi_2(x,t=t_f)|^2, \tag{3.37}$$

which we compute at the final time t_f. This is given by $t_f \geq L/2v$ in the case where we do not consider an axial trapping potential, where v is the incoming velocity, and L is the size of the numerical spatial domain. The value of L is set to 160 and is chosen such that at the starting location ($x = -L/4$) and approximate end location of any transmitted component ($x = L/4$), the soliton components are well resolved from the splitting barrier. Note that interaction with the barrier can slow the trajectory of any transmitted components, meaning that t_f must be increased accordingly.

We have performed systematic simulations to produce $T_{1,2}$ as functions of the four control parameters, *viz.*, v, f, ε and g. The repulsive barrier cannot intrinsically trap any part of the wave functions, meaning that in the absence (or

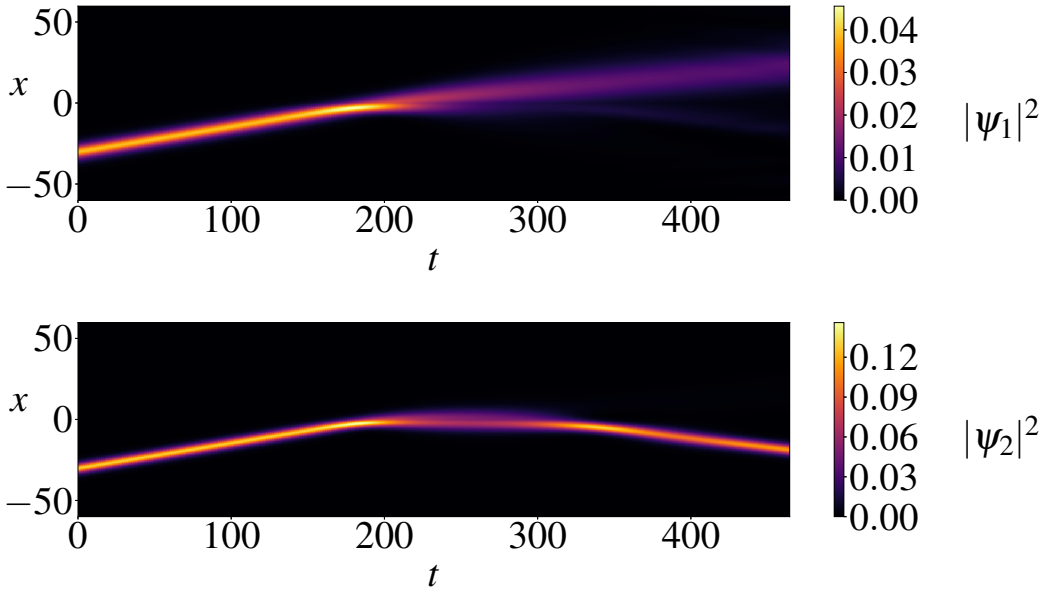

Figure 3.1: The evolution of densities of the two components, which demonstrates the splitting of the incident composite soliton into the passing lighter and bouncing heavier components close to the splitting-unsplitting boundary, at parameter values $\sigma = 0.4$, $\varepsilon = 0.07$, $f = 0.3$, $g = 0.2$, and $v = 0.155$.

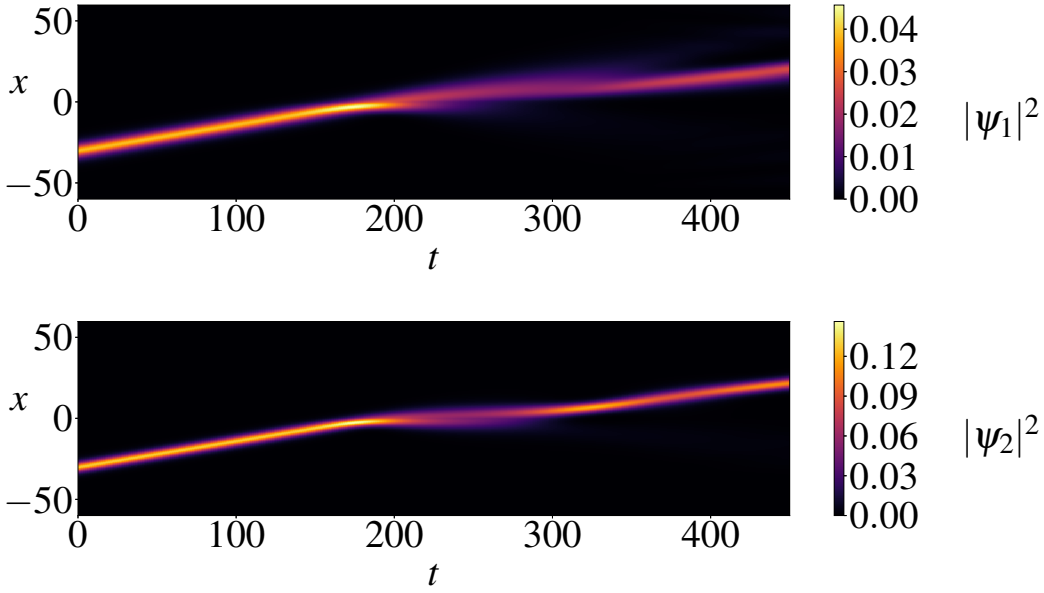

Figure 3.2: The same as in Fig. 3.1, but for the case when incident composite soliton passes the potential barrier without splitting, close to the splitting threshold. Parameters are the same as in Fig. 3.1, except for a slightly larger value of the collision velocity: $v = 0.16$.

negligibility) of axial confinement (see [84], however) the reflection coefficients for the two components are simply $R_{1,2} = 1 - T_{1,2}$. However, it must be noted that if the transmission of a component is close but not equal to 0 or 1, then the smaller portion of the component may not be large enough to form a soliton and will undergo dispersion. This is shown in the increased width of component 1 after passing the barrier in Fig. 3.2. In Fig. 3.1, however, the width of component 1 is different after passing the barrier due to the absence of focussing by component 2 (as $g > 0$), which is reflected.

3.5 Comparison of numerical results for transmission with the analytical predictions

3.5.1 Case of small interspecies interactions

In Figs. 3.3 and 3.4 we show the results of our comparison of the analytical prediction given by Eq. (3.19) with numerical simulations. In general the agreement is quite good, provided that g is small (up to about $g = 0.1$, a significant region for the value of $T_1 - T_2 = 1$ is visible), and ε is not too large (up to the regime of about $\varepsilon \approx 0.1$, as expected for $f = 0.3$ from Eq. 3.17, as shown in Fig. 3.3).

In Figs. 3.3 and 3.4, the splitting degree, as produced by the simulations, is reported in detail by plotting the difference $T_1 - T_2$ as a function of all the control parameters, (ε, v, g, f). Simultaneously, the same figures display the comparison of the analytical prediction, given by Eq. (3.19), with the numerical findings. Indeed, the analytical result implies that $T_1 = 1$ and $T_2 = 0$ in the interval Eq. (3.19) of velocities of the incident composite soliton, and, on the other hand, $T_1 = T_2$ outside of the interval, where the incident soliton does not split. It is clearly seen in Figs. 3.3 and 3.4 (as well as in Fig. 3.12, which is produced below with the alternative implementation of the δ-function) that the prediction is quite accurate for small g, gradually deteriorating with the increase of g. This is explained, in particular, by the fact that, at relatively large values of g, the attraction between the components naturally tends to suppress the collision-induced splitting, and, on the other hand, each component is only

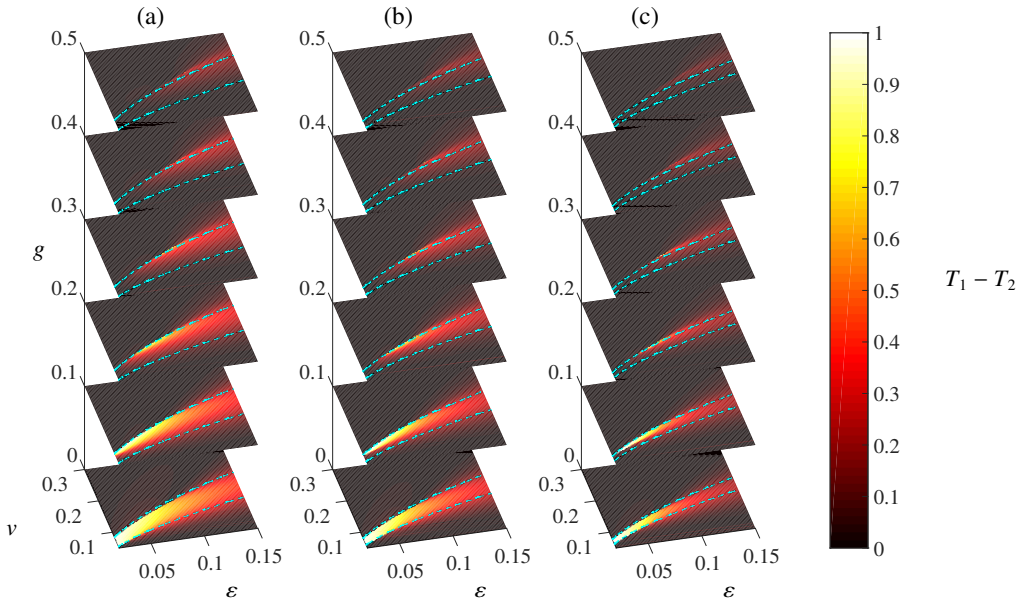

Figure 3.3: The transmission difference between the two components, $T_1 - T_2$, as produced by simulations of Eqs. (3.8a) and (3.8b), in the (v,ε) parameter plane (where v is the collision velocity and ε the strength of the Gaussian potential barrier) at different values of g and f (the cross-attraction strength and scaled population of the first component). The value of g increases along the vertical axis. (a) $f = 0.3$, (b) $f = 0.35$, and (c) $f = 0.4$. Here and in Fig. 3.4 the dashed lines display boundaries of the splitting region as analytically predicted by Eq. (3.19) in the limit of $g = 0$. The transmissions are displayed using a colour scale over a 100×100 sample size.

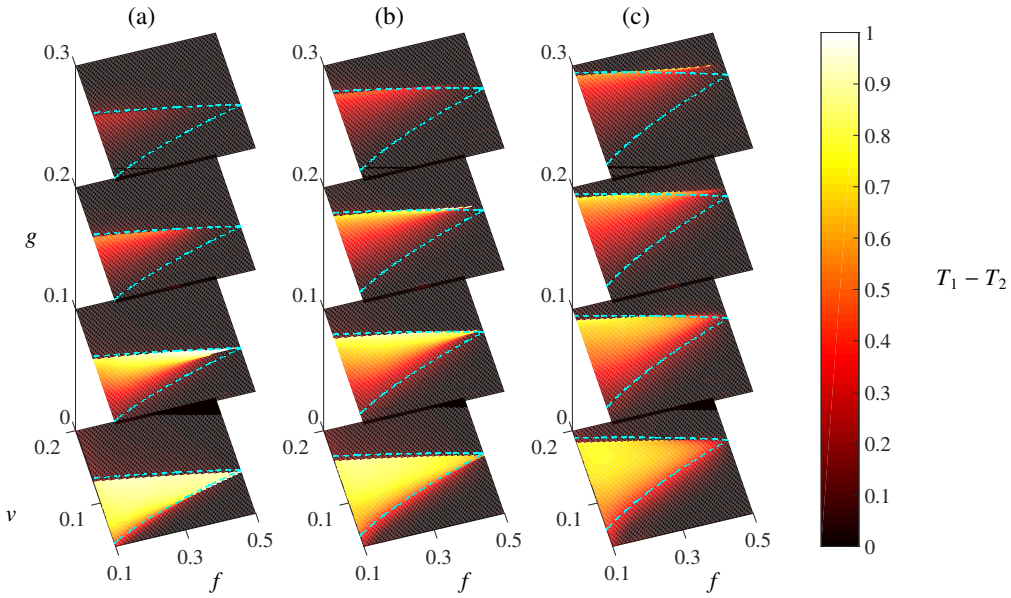

Figure 3.4: Similar to Fig. 3.3, but in the (v, f) parameter plane at different values of g and ε. (a) $\varepsilon = 0.04$, (b) $\varepsilon = 0.06$, and (c) $\varepsilon = 0.08$. The transmissions are displayed using a colour scale over a 100×100 sample size.

partly transmitted and partly reflected, i.e., T_1 and T_2 take intermediate values between 0 and 1, with the increase of the barrier's height, ε. The figures also corroborate the prediction of Eq. (3.19) that the splitting region strongly shrinks as f is approaching 1/2, i.e., the components of the incident composite solitons become nearly equal. Also, the figures agree with the condition given by Eq. (3.17) as the separation, $T_1 - T_2$, is stronger (closer to 1) for smaller values of ε and decreases (between the dotted lines marking the predictions given by Eq. (3.19)) with increasing g and ε.

3.5.2 Case of asymmetric nonlinearities

We have collected numerical results for the case of strong asymmetry between the two components of the incident composite soliton, i.e., situations satisfying Eq. (3.23), with $g' = 1$, are collected in Fig. 3.5. This figure clearly demonstrates that the analytical prediction, elaborated for this case in the form of Eq. (3.33), is quite accurate, at least up to $f = 0.05$, in sufficiently broad intervals of values of g and ε. As in the case of small interspecies interactions, we cannot expect perfect splitting (i.e. $T_1 - T_2 \neq 1$) for larger values of g. This is codified in the case

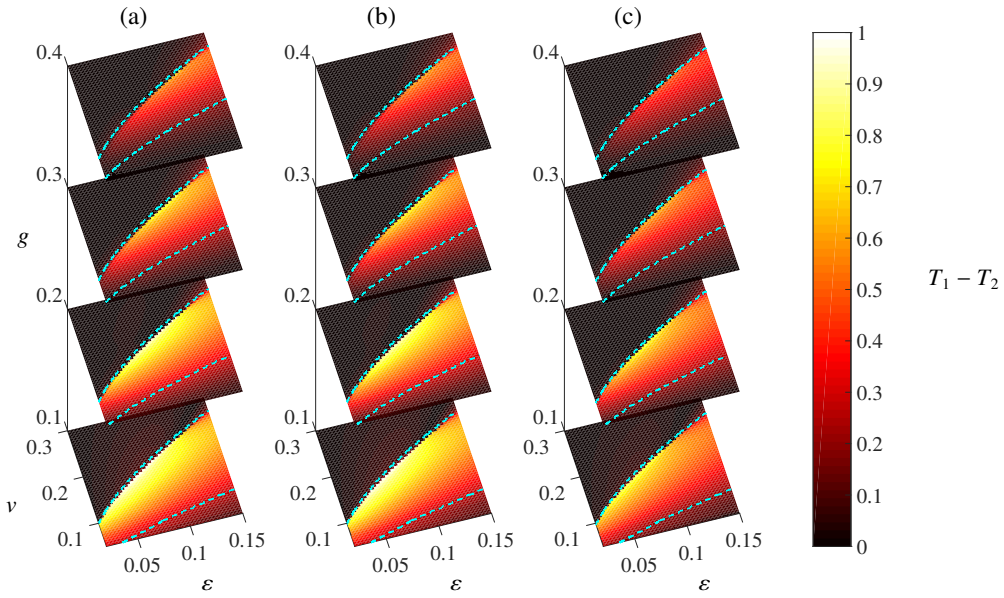

Figure 3.5: The transmission difference between the two components, $T_1 - T_2$, as produced by simulations of Eqs. (3.8a) and (3.8b), in the (v, ε) parameter space (where v is the collision velocity and ε the strength of the Gaussian potential barrier) at different values of g and f (the cross-attraction strength and scaled population of the first component). The value of g increases along the vertical axis. (a) $f = 0.01$, (b) $f = 0.02$, and (c) $f = 0.05$. Here the dashed lines display boundaries of the splitting region as analytically predicted by Eq. (3.33) in the limit of $f \ll 1$. The transmissions are displayed using a colour scale over a 100×100 sample size.

of strongly asymmetric nonlinearities in the additional condition for separation given by Eq. (3.35), although it produces only a qualitative indication. Note the difference compared to Figs. 3.3 & 3.4 in that the predictions given by Eq. (3.33) apply most accurately in Fig. 3.5 for low f and low ε.

Although we have found it simpler in our simulations to vary f only, we reiterate that it may not be experimentally practical to work with a very small atomic population in one of the components, for reasons of imaging the density profiles in the weakly populated component, and, generally speaking, validity of the mean-field theory. On the other hand, simulations performed for the alternative regime of $1 \ll g \ll g'$ with $f = 1/2$ (not shown here) yield qualitatively similar results. How best to fulfil Eq. (3.23) in a particular experimental configuration may depend on what the available values of the scattering lengths are.

3.5.3 Continuous variation of the interspecies interaction strength with and without weak axial harmonic confinement

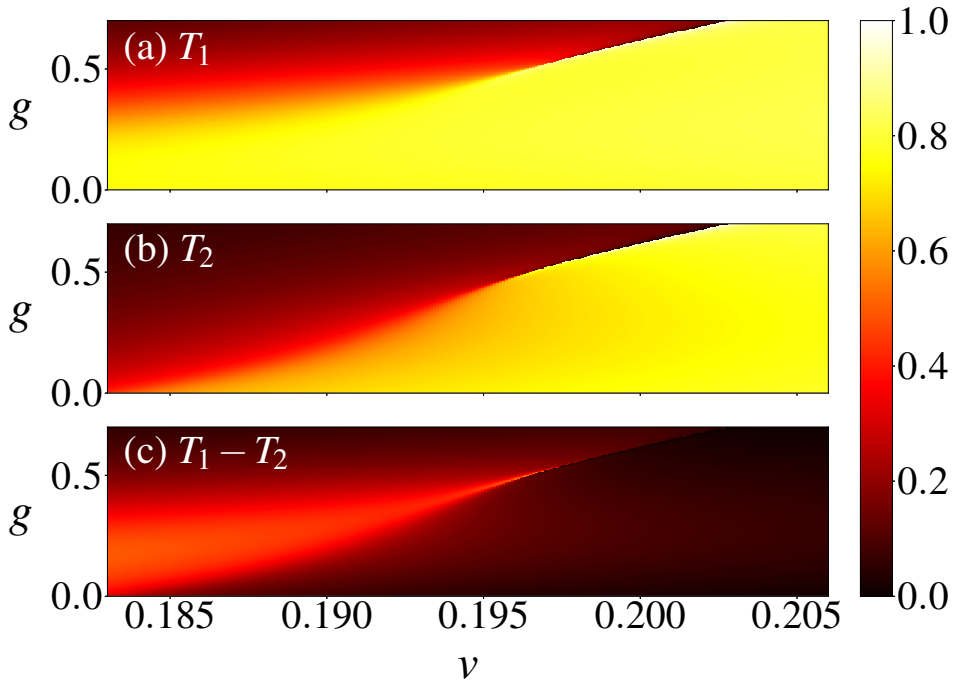

Figure 3.6: The transmission coefficients of the two components, produced by the simulations of Eqs. (3.8a) and (3.8b) for the composite soliton, with the relative norm of the first component $f = 0.3$ incident on the splitter with strength $\varepsilon = 0.1$, in the parameter plane of the collision velocity v and the interspecies attraction g. Panels (a), (b), and (c) display, severally, the transmission coefficients of the first and second components, and their difference.

In addition to considering the situation where a soliton moves with a given velocity in free space, simulations were also carried out where the soliton begins its motion from an initial position x_0 on one side of an external harmonic oscillator potential

$$U = \omega_x^2 x^2/2. \tag{3.38}$$

This setting implies that the soliton accelerates to an incident velocity

$$v = \omega_x x_0, \tag{3.39}$$

when it hits the narrow barrier placed at $x = 0$.

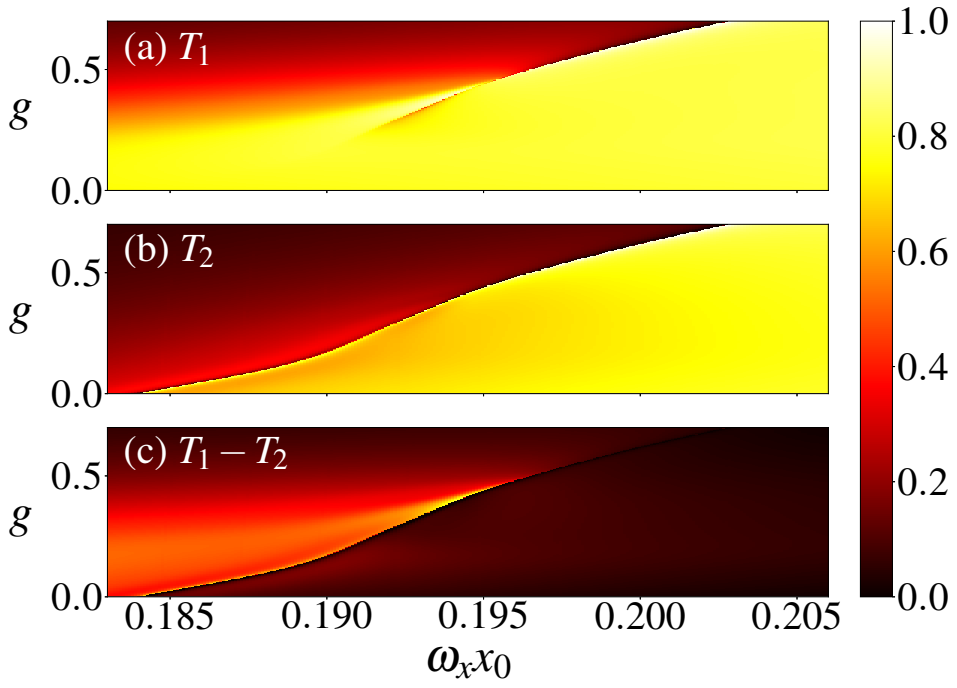

Figure 3.7: The same as in Fig. 3.6, but in the case when the collision velocity is given by $\omega_x|x_0|$ for the incident soliton accelerated from initial position x_0 by the trapping potential.

Figure 3.6 shows how the transmission in both components varies in the (v, g) parameter space for $\varepsilon = 0.1$ and $f = 0.3$ in the free-space configuration (no axial trapping). In this case, Eq. (3.19) predicts that both components of the composite soliton pass the barrier, without splitting, at $v > \sqrt{\varepsilon\left(1-f\right)/2} \approx 0.187$. The numerical findings collected in Fig. 3.6 support this prediction. This case can be compared to that when the axial harmonic oscillator confinement is present, as per Eq. (3.38). Figure 3.7 shows the results for an equivalent range of parameters with the collision velocity given by Eq. (3.39). In this figure, the axial trapping produces a sharper boundary in the (v, g) parameter space, separating the cases of component 2 being reflected and transmitted.

In Fig. 3.8, display another aspect of the results shown in Figs. 3.6 and Fig. 3.7 by means of boundaries between parameter regions where the second component is effectively reflected or transmitted for different values of the barrier's strength, ε, while fixing the proportion of the total population in this component at $1 - f = 0.7$. We define this boundary by the condition $T_2 = 0.5$. Both

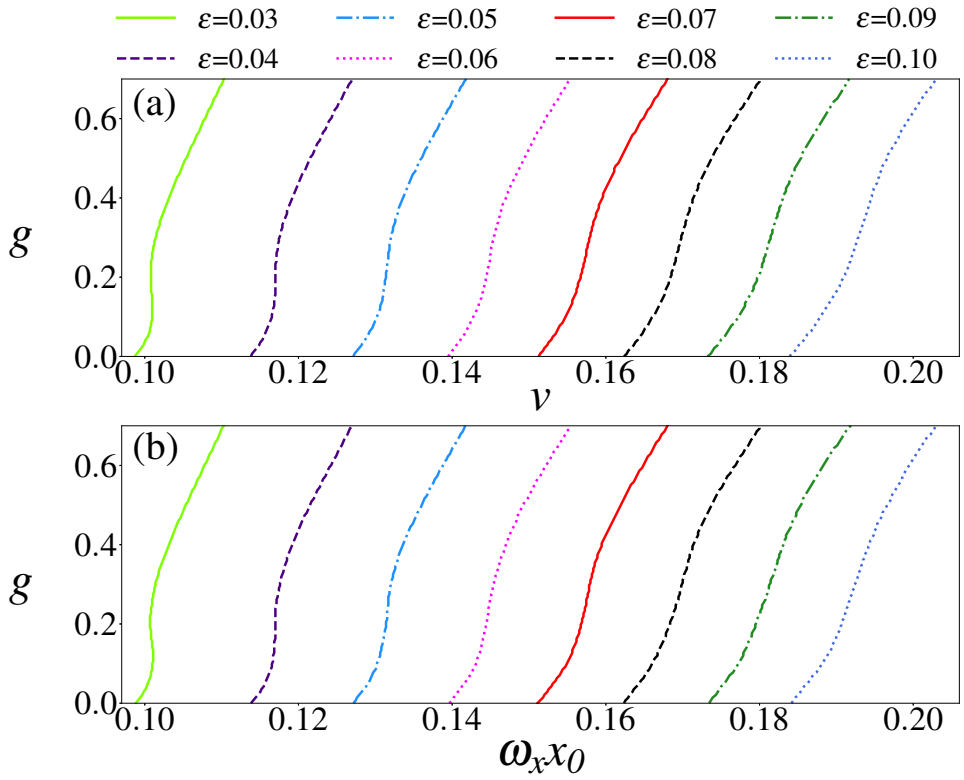

Figure 3.8: Boundaries in the (v, g) parameter plane (the collision velocity and relative cross-attraction strength) between regions where the second component of the incident composite soliton, with a fixed relative share of the total norm, $1 - f = 0.7$), effectively bounces (left of the boundary) or passes (right of the boundary), for varying values of the barrier's strength, ε. (a) The case of the incident solitons arriving with velocity v; (b) for the soliton accelerated by the trapping potential with an impact velocity of $\omega_x |x_0|$ with $|x_0| = 40$.

sets of Figs. 3.6 and 3.8(a), which pertain to the soliton-barrier collision in free space, and Figs. 3.7 and 3.8(b), that display the numerical findings for the splitter embedded in the external trapping potential [Eq. (3.38)], demonstrate that making the attraction between the two components stronger, as quantified by increasing the parameter g, while keeping other parameter values fixed (relative population f and barrier area ε), leads to oscillations in, (v, g) parameter space, between positive and negative values of the boundary's curvature.

3.6 Internal excitations in past-collision solitons

An important aspect of the numerical results is the presence of intrinsic excitations in the separated and unseparated solitons after the interaction with the barrier. In particular, for use in interferometers the solitons should keep a nearly-fundamental shape, without conspicuous internal vibrations. To this end, we define the measure of the intrinsic excitation in the j^{th} soliton ($j = 1,2$) as

$$\eta_j = \frac{\max(n_j) - \min(n_j)}{\max(n_j) + \min(n_j)}, \tag{3.40}$$

where $n_j \equiv \left|\psi_j(x_c)\right|^2$ is the density at the soliton's centre, with the maximum and minimum taken with respect to the evolution in time. It is shown in Fig. 3.9 for different values of the interspecies coupling strength, g, and $f = 0.3$, $v = 0.112$, $\varepsilon = 0.04$, which represents a situation where an increase in g causes component 1 to go from almost completely reflected (and separated from component 1) to almost completely transmitted (and not separated from component 2), in accordance with data displayed in Figs. 3.3 and 3.4. In these simulations, the initial distance from the barrier, $|x_0|$, was increased to 200 in order to clearly observe the intrinsic oscillations with a corresponding increase in propagation time. Simultaneously, Fig. 3.9 shows that the excitation degree in the passing solitons (in component 1) first increases from $\simeq 0.07$ to $\simeq 0.14$, and then decreases. The excitation in the rebounding soliton (in component 2) follows a similar trend, but remaining smaller, roughly, by an order of magnitude. These trends are explained by an effect of increasing attraction between the components on the excitation of the intrinsic vibrations in the solitons with the growth of g, as well as by the effect of the varying shape of the interaction products on the internal excitations in these products. A conclusion is that, in the case of high-quality fission of the incident compound soliton into the passing and rebounding ones, at g sufficiently small, the excitation effect remains weak. This conclusion is quite natural, as the purity of the splitting deteriorates with the increase of g, which leads to deformation of the splitting products, especially the passing soliton, and the deformation excites the intrinsic vibrations.

Figure 3.10 shows the evolution in time of $\max(n_j)$ (with the maximum taken over position here) for both components as well as the final density. One can

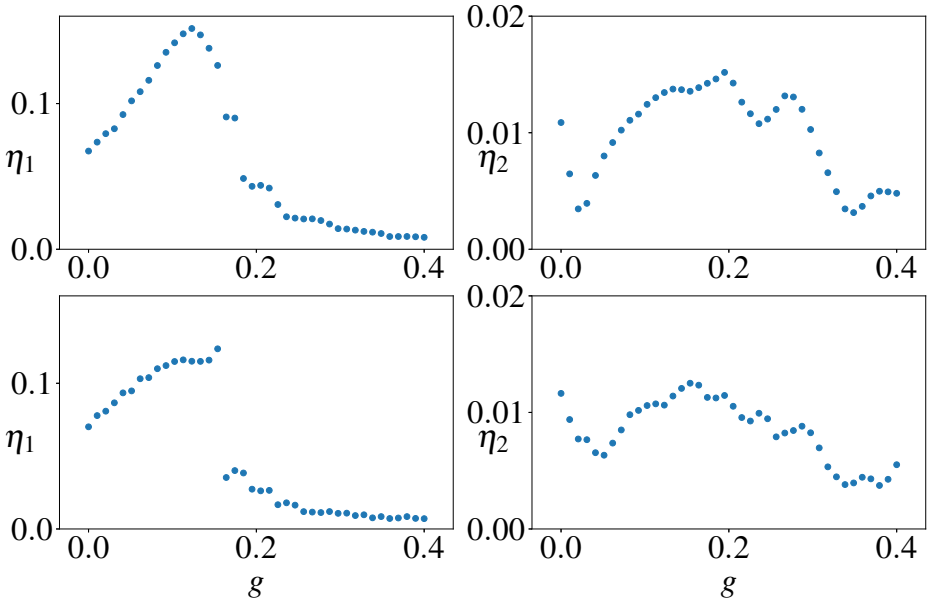

Figure 3.9: The figure shows the effect of the collision with the barrier on the amount of oscillation in height (as a measure of the stability of the solitons) for different values of coupling strength g. The top two plots show the value of η_i, defined by Eq. (3.40), where the components are not trapped in the axial direction. The bottom two plots show the values of η_j when the components are accelerated by an axial harmonic trap. In order to observe the oscillations, an initial displacement of $|x_0| = 200$ is used for both cases and the value of $\max(n_j)$ during the splitting is neglected in the determination of η_j.

see that there are various factors which will determine the value of η_j. As shown in previous results, the value of g will affect the outgoing populations in components 1 and 2. After the barrier collision, if component 1 is transmitted then its amplitude will be changed due to the lack of focussing from component 2 (assuming $g > 0$) resulting in height and width oscillations. This provides an explanation for the behaviour of $\max(n_1)$ in Fig. 3.9; as well as $\max(n_2)$, which will exhibit a less pronounced change in size due its being larger than component 1. The values of η_j against time are shown in (a) and (c) for components 1 and 2, respectively. For further clarification, the outgoing soliton profiles are shown in (b) and (d) for components 1 and 2, respectively, which show the density of both components after the collision with the splitting barrier.

It is relevant to stress that the excitation degree is much smaller than in the previously studied case of the "brute-force"splitting of a single-component funda-

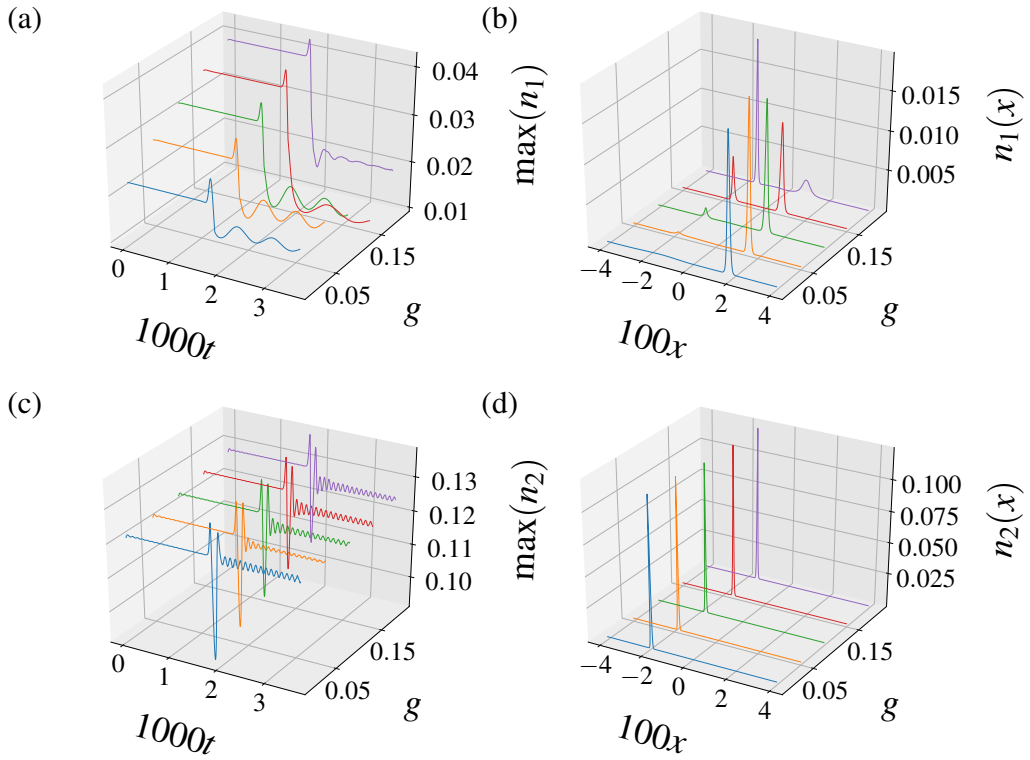

Figure 3.10: The figure shows the effect of the collision with the barrier on the heights of the solitons (which we use as a measure of the soliton stability) for different values of coupling strength g. Plots (a) and (c) show the value of $\max(n_j)$, (for the case of no axial trapping potential) for component 1 in (a) and component 2 in (c). In order to observe the height oscillations, we extend the grid size to $L = 800$ and set the time as that taken for solitons to move from $-L/4$ to $L/4$ with the barrier at $L = 0$. Plots (b) and (d) show the final density of components 1 and 2, respectively. Note that component 2 is always reflected by the barrier whereas component 1 changes from majority transmission to majority reflection upon increase of g. This explains the more complex behaviour in (a) than in (c).

mental soliton by a strong barrier [56, 110–118]. To address this point, we note that, in the case of the ideal splitting of an incident fundamental soliton with amplitude $2A$ into two separated fragments, each one, with a central coordinate x_0 and phase Φ_0, is naturally approximated by the expression

$$\psi_{\rm frag}(x) = A\exp\left(i\Phi_0\right)\mathrm{sech}\left(a[x-x_0]\right), \tag{3.41}$$

cf. Eq. (3.11), with $a = 2A$. Further evolution of the "half-soliton", initiated by this expression, can be produced by the exact Satsuma–Yajima solution [119], which is quite complicated. However, states with the largest and smallest values of the density at the centre, which define the excitation measure (3.40), are ones with zero chirp [104], which makes it possible to approximate them by ansatz (3.41) with independent values A and a, subject to the conservation of the norm,

$$\mathcal{N} \equiv \int_{-\infty}^{+\infty} \left|\psi(x)\right|^2 \mathrm{d}x = 2A^2 a^{-1} \tag{3.42}$$

(in the above analysis, normalization $\mathcal{N} = 1$ is adopted). Further, the substitution of the ansatz in the Hamiltonian of the ideal NLSE,

$$H_{\rm single} = \frac{1}{2}\int_{-\infty}^{+\infty} \left(\left|\partial_x\psi\right|^2 - |\psi|^4\right)\mathrm{d}x \tag{3.43}$$

[cf. Eq. (3.9)], yields the corresponding value of the energy,

$$E_{\rm single}(A) = \frac{1}{3}\left(A^2 a - 2A^4 a^{-1}\right) \equiv \frac{1}{3}\left(2\mathcal{N}^{-1}A^4 - \mathcal{N}A^2\right), \tag{3.44}$$

where relation (3.42) is used. Finally, equating energy (3.44) for the zero-chirp states realizing the states with maximal and minimal densities at the centre, the former one given by the split-soliton ansatz (3.41), it is easy to find the relation between them, $\min(n) = (1/2)\max(n)$ (it does not depend on $\mathcal{N}$). The respective value of the excitation measure, as given by Eq. (3.40), is $\eta_{\rm single} = 1/3$. Thus, the above-mentioned typical values of η_j for the two components of the binary system are smaller than their counterparts in the single-component model, in the case of the ideal splitting, by a factor $\simeq 3-4$,. This is because the components are coupled by the parameter $g < 1$. In the real single-component setting, numerical results yield even larger values of the excitation measure, $\eta_{\rm single} \simeq 0.5\ -0.6$ [56]. Thus, the binary system provides, as expected, essential suppression of detrimental effects of the post-collision intrinsic excitation of the fragments.

3.7 The effect of the finite barrier width

In Fig. 3.11 we show boundaries corresponding to $T_1 = 0.5$, which separate the effective reflection and transmission of the first component in the parameter space of collision velocity v and barrier area ε, for different fixed values of f, g, and the barrier width σ [see Eq. (3.7)]. Note that we have obtained the results for $\sigma = 0$ by means of the numerical method outlined in Sec. 3.8, in which we represent the "ideal" δ-functional barrier in Fourier space, and incorporate it in the split-step simulation algorithm in the same step as the kinetic energy term [see Eq. (3.46)].

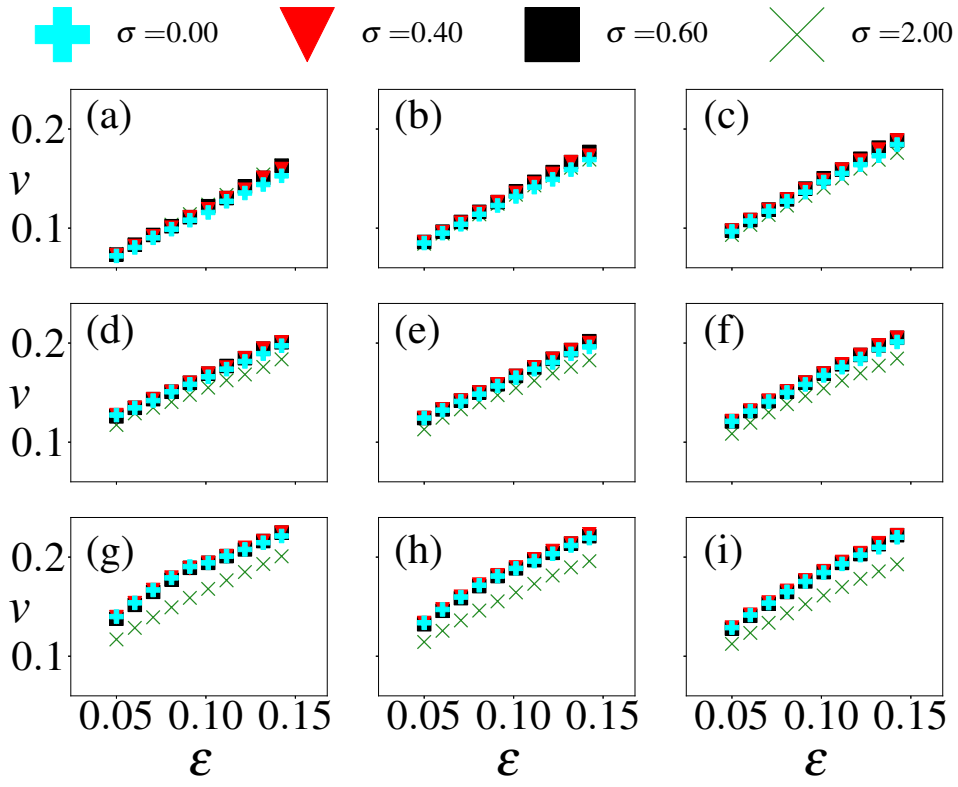

Figure 3.11: Boundaries at which the transmission coefficient for the first component is $T_1 = 0.5$ in the (ε, v) parameter plane, for different values of width σ of the Gaussian barrier (3.7), which are indicated in the panels (with $\sigma = 0$ representing the ideal δ-function). Other parameters are $f = 0.2, g = 0$ in (a), $f = 0.3, g = 0$ in (b), $f = 0.4, g = 0$ in (c), $f = 0.2, g = 0.2$ in (d), $f = 0.3, g = 0.2$ in (e), $f = 0.4, g = 0.2$ (f), $f = 0.2, g = 0.4$ in (g), $f = 0.3, g = 0.4$ in (h), and $f = 0.4, g = 0.4$ in (i).

We choose parameter ranges in Fig. 3.11 so as to make them representative for values used in Figs. 3.1–3.8. From Fig. 3.11 one can see that the location in the

(ε, ν) parameter plane where $T_1 = 0.5$ is more sensitive to width σ of the barrier when g is relatively large, and that for the range of values of f and g considered in the analysis, the dynamics are, naturally, more sensitive to the variation of g than the variation of σ. Increasing σ, while keeping other parameter values constant, may cause the value of ν at which $T_1 = 0.5$ to become either lower or higher, depending on the other parameters. In particular, a conclusion is that, for $\sigma = 0.4$, this value of ν is consistently larger than that for the ideal δ-function ($\sigma = 0$), even if this difference is never greater than 0.01.

3.8 Numerical simulations with δ-functions

The scheme for handling the exact δ-function barrier in the simulations is adapted from Ref. [120]. This incorporates the Fourier transform of the δ-function, $\hat{\delta}(k)$, into the part of the split-step method which implements the kinetic-energy term, T. The relevant expression for the split-step algorithm in the Fourier space is then

$$\mathcal{F}[T + \varepsilon\delta(x)] = \frac{1}{2}k^2 + \varepsilon\hat{\delta}(k). \tag{3.45}$$

Due to the fact that one is conflating an analytical expression for the Fourier transform and its discrete computational counterpart, one must be careful while defining the periodic domain for the Fourier transform. To use the discrete Fourier transform, in the numerical computations we choose the domain as $-L/2 \leq x < +L/2$, placing the δ-function at the centre. The corresponding operator for the kinetic energy, combined with the energy introduced by the δ-function, is then written as

$$(M_1)_{mn} = \mathcal{F}[T + \varepsilon\delta(x)]_{mn} = \frac{1}{2}k^2\delta_{mn} + \frac{\varepsilon}{L}, \tag{3.46}$$

where k is defined as a discrete variable running between $-\pi/L$ and $+\pi/L$ with N entries, indexed by integers (m, n), and δ_{mn} is the Kronecker's delta. When using standard FFT routines in the current context, they must be used in conjunction with two shifting protocols (which shift the location of zero frequency to the centre of the array) whenever they are applied, in order to run them in a way which is consistent with the physically relevant boundary conditions.

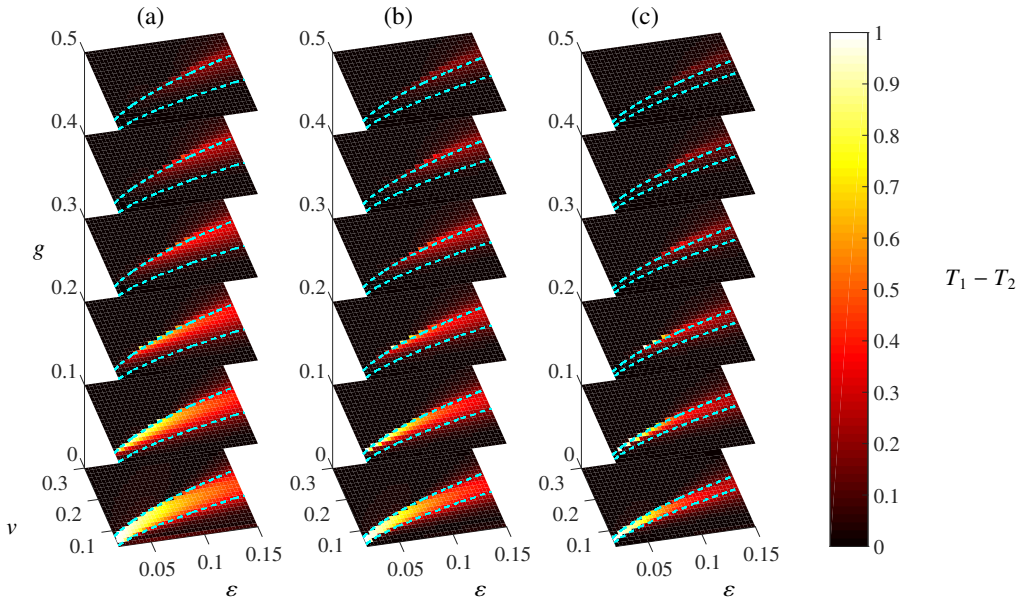

Figure 3.12: The same as in Fig. 3.3, but with a barrier produced by the numerical algorithm which implements the δ-function instead of a Gaussian barrier. The transmissions are displayed using a colour scale over a 40×40 sample size.

Alternatively, one can use only one shifting protocol by accounting for a phase offset in the resulting expression for the δ-function in the Fourier space. The expression for the sum of the kinetic energy with the energy of the δ-functional barrier is then

$$(M_2)_{mn} = \mathcal{F}[T + \varepsilon\delta(x)]_{mn} = \frac{k^2}{2}\delta_{mn} + \frac{\varepsilon}{L}\exp\left(\frac{iL}{2}[k_m - k_n]\right), \tag{3.47}$$

cf. Eq. 3.46. Note that if we were only considering the kinetic energy, this would make no difference, and it is in fact common practice to only use one shifting protocol in this case.

To execute this step in the split-step algorithm, one must diagonalise matrix M_1 or M_2 and combine the associated amount of shifts with the Fourier transforms, as mentioned above. Note that the diagonalisation need only be done once, as it is constant throughout the simulations (recalculation is required only if ε or L is altered). The need, on a grid with N spatial points, for $(N \times N)$-dimensional matrix multiplications at each timestep, in order to implement this method, increases the computational time. As a result, the resolution of parameter space, as plotted in Fig. 3.12, is reduced relative to comparable plots presented above when using the Gaussian barrier.

Figure 3.12 shows a counterpart of Fig. 3.3, produced by the numerical scheme outlined in this appendix. Comparison of the plots suggests that, for $g = 0$, the results are quite similar, and the analytical treatment gives a good indication of what to expect. Deviations of the numerical results from the analytical approximation are primarily caused by the nonlinearity and deformation of the solitons' shapes, rather than by the deviation of the numerically approximated potential barrier (as long as it is sufficiently narrow) from the ideal δ-function.

3.9 Second collision of the components on the barrier

After the splitting of the solitary waves on the barrier, an interesting question is what happens if the trajectories are continued in order to allow second collisions on the barrier. This could be either by imposing periodic boundary conditions which emulate a ring trap configuration or by imposing a harmonic trap configuration such that the components experience a restoring force which leads to repeated collisions at the barrier. In this situation the components cannot interfere with each other and the smaller component (ψ_1) is partially transmitted on the first collision. Therefore, we expect a complex transmission behaviour as a function of the parameters ($v, f, g \& \varepsilon$), corresponding to the velocity, population of component 1, interspecies scattering length and barrier area.

Figures 3.13, 3.15 & 3.17 show the transmission of component 1 resulting from a second collision in the ring trap and Figs. 3.14, 3.16 & 3.18 show those for a second collision in a harmonic trap. In each figure, (a)-(d) show the results for interspecies couplings of 0, 0.1, 0.2 & 0.3, respectively. Therefore (a) shows the system with no coupling between the components and (b)-(d) display the effects of the couplings which influence the transmission in the first instance (see Fig. 3.4) as well as the second collision on the barrier. For all figures $f = 0.3$ and for Figs. 3.13 & 3.14 $\varepsilon = 0.04$; for Figs. 3.15 & 3.16 $\varepsilon = 0.06$ and for Figs. 3.17 & 3.18 $\varepsilon = 0.08$

One can notice a complex relationship between the second transmission (population on the right side of the interferometer after two collisions with the bar-

rier) of component 1 and the parameters v, f, ε & g. The figures show the same region of (v, f) parameter space as Fig. 3.4 (with the range of f extended) which can be compared to indicate the first transmission value for different values of ε and g. Note that in these plots, we only display the behaviour of component 1; however, we extend the range of f to vary between 0 and 1. The values for $f > 0.5$ therefore correspond to the behaviour of component 2 for $f < 0.5$. Hence the line of symmetry at $f = 0.5$, which emerges with increasing g, reflects the increased coupling between the two components which leads to them following the same behaviour.

In order to predict the expected transmission when solitons meet on a barrier, one would also need the value of a phase difference between outgoing fragments of component 1 (assuming T_1 is neither 0 nor 1), which is not ascertainable from Fig. 3.4. Complexity in these figures arises from a combination of the different sizes of fragments, the different amounts of focussing arising from both inter- and intra-species interactions, as well as how the phase imparted by the barrier is affected by the nonlinear coupling to component 2 and the interaction of the barrier. The presence of a harmonic trapping potential adds additional complication as the motion (not considering the barrier) of the solitons with $g = 0$ is non-integrable in this setting. In agreement with the results shown in Sec. 3.10, the nonlinear effects which appear in Figs. 3.13-3.18 decrease with increasing barrier area.

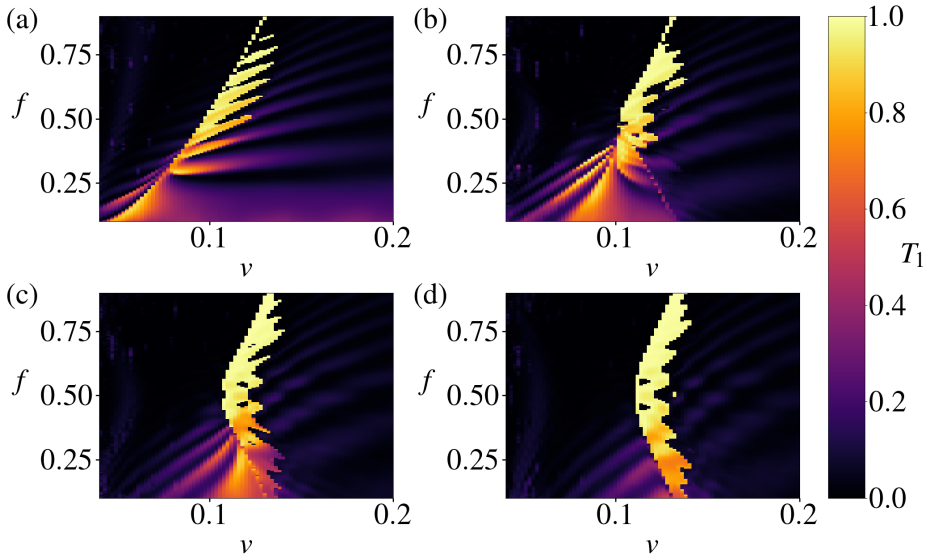

Figure 3.13: Transmission coefficients for component 1 in (v, f) parameter space for no external trapping potential after the allowing the solitons to re-collide on the potential barrier with area, $\varepsilon = 0.04$ and interspecies coupling strength, g equal to 0 in (a), 0.1 in (b), 0.1 in (c) and 0.3 in (d).

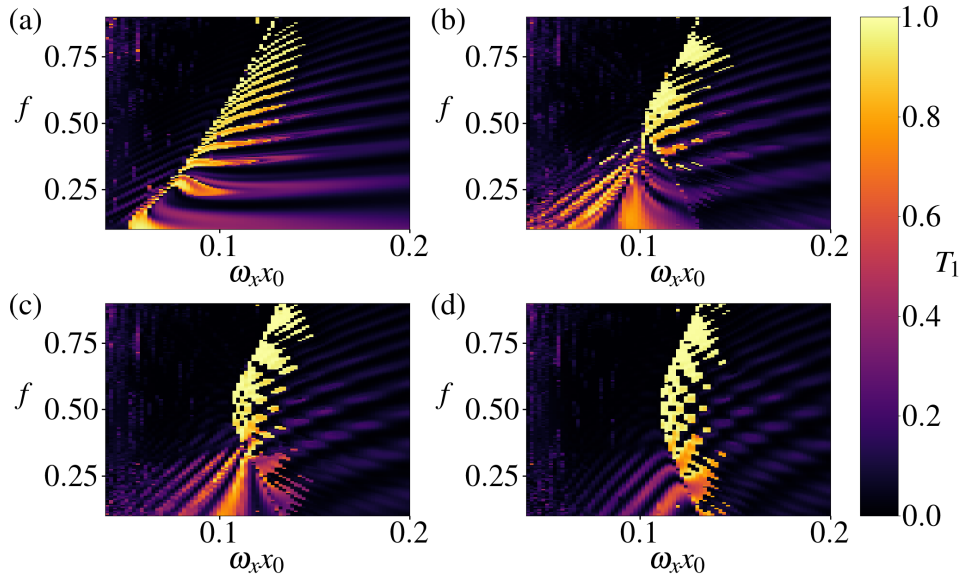

Figure 3.14: Transmission coefficients for component 1 in (v, f) parameter space for motion in a harmonic trapping potential after the allowing the solitons to re-collide on the potential barrier with area, $\varepsilon = 0.04$, and interspecies coupling strength, g, equal to 0 in (a), 0.1 in (b), 0.1 in (c) and 0.3 in (d).

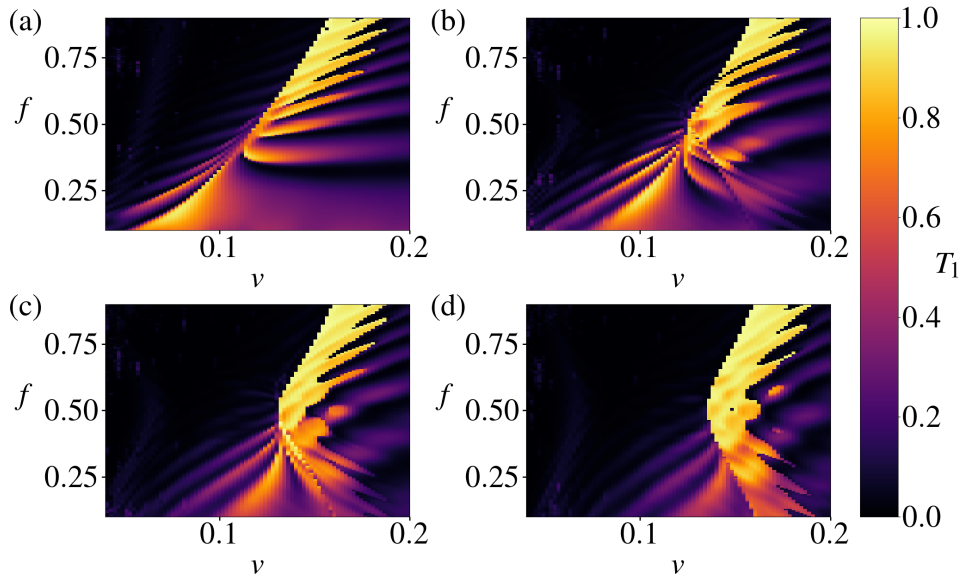

Figure 3.15: Transmission coefficients for component 1 in (v, f) parameter space for no external trapping potential after the allowing the solitons to re-collide on the potential barrier if area, $\varepsilon = 0.06$, and interspecies coupling strength, g, equal to 0 in (a), 0.1 in (b), 0.1 in (c) and 0.3 in (d).

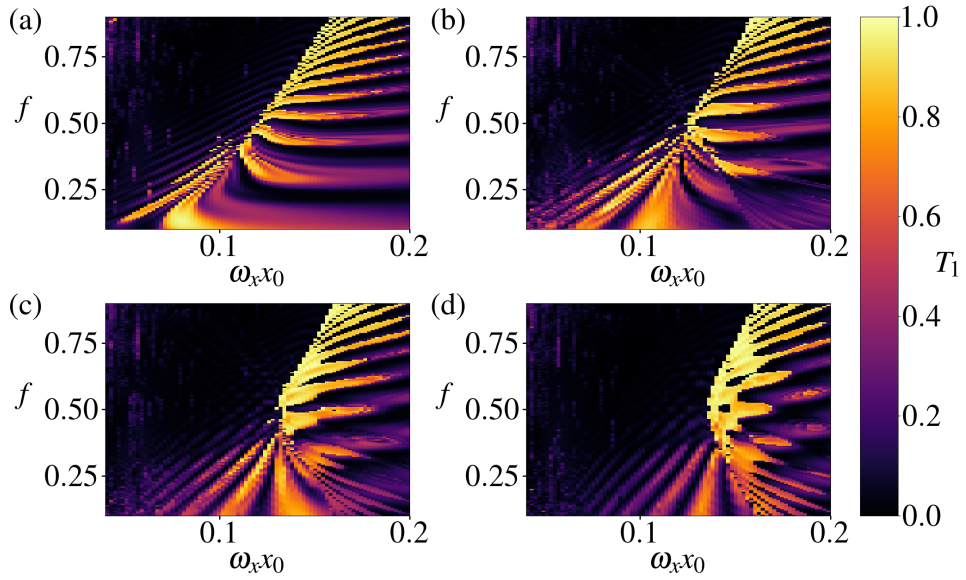

Figure 3.16: Transmission coefficients for component 1 in (v, f) parameter space for motion in a harmonic trapping potential after the allowing the solitons to re-collide on the potential barrier with area, $\varepsilon = 0.06$, and interspecies coupling strength, g, equal to 0 in (a), 0.1 in (b), 0.1 in (c) and 0.3 in (d).

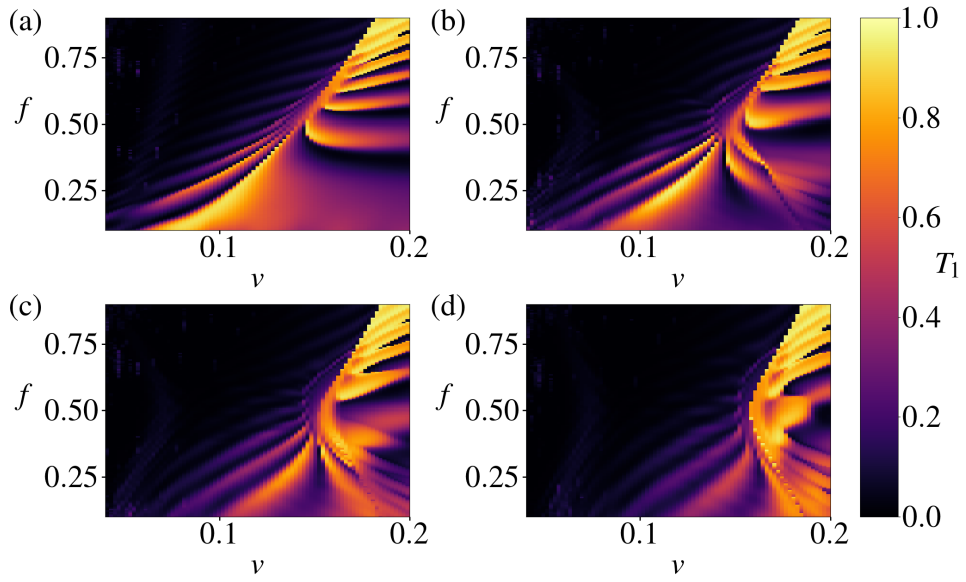

Figure 3.17: Transmission coefficients for component 1 in (v, f) parameter space for no external trapping potential after the allowing the solitons to re-collide on the potential barrier with area, $\varepsilon = 0.08$, and interspecies coupling strength, g, equal to 0 in (a), 0.1 in (b), 0.1 in (c) and 0.3 in (d).

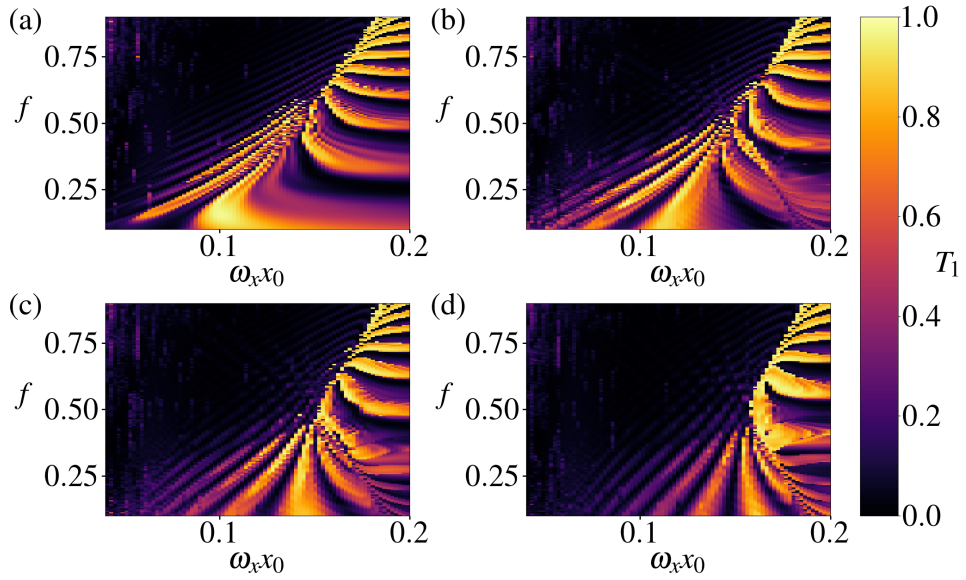

Figure 3.18: Transmission coefficients for component 1 in (v, f) parameter space for motion in a harmonic trapping potential after the allowing the solitons to re-collide on the potential barrier with area, $\varepsilon = 0.08$, and interspecies coupling strength, g, equal to 0 in (a), 0.1 in (b), 0.1 in (c) and 0.3 in (d).

3.10 Collisions of distinct species solitons on a potential barrier

As well as the investigation into the transmission of two-component solitary waves when impacted onto a narrow potential barrier, it is also possible to use the same principle of perturbation theory, in the regime of negligible g and small ε, to analyse the effect of collisions between solitons of distinct species on a narrow barrier (i.e.- meeting on a barrier with the same velocity). In this case, one has the soliton solutions (far from the barrier) even when $g \neq 0$ as the components are initially separated. The analysis then predicts the regions where the components are combined on the barrier.

The initial wavefunctions (assuming the components are well-separated) impacting on the barrier with equal and opposite velocity are then given by

$$\psi_1(x,t) = \frac{f}{2}\exp\left(\mathrm{i}\left[vx-\mu_1 t\right]\right) \times \operatorname{sech}\left(\frac{f}{2}\left[x-(x_0+vt)\right]\right), \tag{3.48a}$$

$$\psi_2(x,t) = \frac{(1-f)\sqrt{g'}}{2}\exp\left(-\mathrm{i}\left[vx+\mu_2 t\right]\right) \times \operatorname{sech}\left(\frac{[1-f]g'}{2}\left[x+(x_0+vt)\right]\right), \tag{3.48b}$$

where $v>0$ and we take $x_0=-40$ for all data below, and with associated chemical potentials

$$\mu_1 = -f^2/8 + v^2/2, \tag{3.49a}$$

$$\mu_2 = -\left(1-f\right)^2 g'^2/8 + v^2/2. \tag{3.49b}$$

We can investigate the effect on the post-collision products of a non-zero interspecies coupling, g, using simulations. The results for this are shown in Figs. 3.19 & 3.20. Figure 3.19 shows the population on the right side (positive x-axis), using the definition Eqs. (3.36 & 3.37), of the system after the collision on the barrier for continuously varied interspecies coupling g with $\varepsilon = 0.05$ and $f = 0.3$. Note that because of the change in the initial system configuration, the terminology of transmission in the figure no longer refers to transmission through the barrier for component 2. Figure 3.19 shows that increasing g causes nontrivial transmission behaviour in the components which is more

pronounced than for the case where both components start at the same location and are impacted on the barrier. In the case where we look to separate the components on the barrier, the initial wavefunctions are found through propagating in imaginary time. Whereas, in this case where the components are initially separated, the post-collision products would exhibit oscillatory behaviour and we also see this effect in the transmission behaviour because of nonlinear effects (with a coupling controlled by the parameter g) during the interaction with the barrier. For component 2, the velocity region in Fig. 3.19 between 0.12 and 0.13 has a transmission switching between 0 and 1 upon variation in g for the parameter values $f = 0.3$ and $\varepsilon = 0.05$. In Fig. 3.20 we extend this to other barrier area values and plot the boundary in (v, g) space between component 2 undergoing reflection and transmission for different values of ε with $f = 0.3$ remaining fixed. Figure 3.20 shows a decrease in the size of the velocity region across which the transmission oscillates between 0 and 1 with increasing ε.

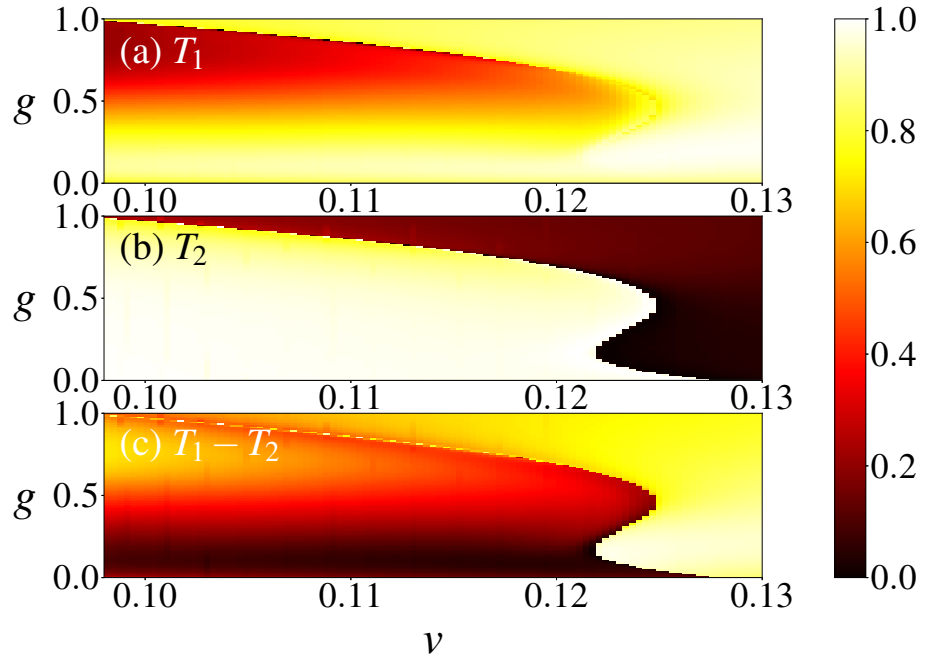

Figure 3.19: Transmission coefficients for both components in (v, g) parameter space where the components start on opposite sides of the trapping potential with parameter values of $\varepsilon = 0.05$ and $f = 0.3$ and no external trapping potential.

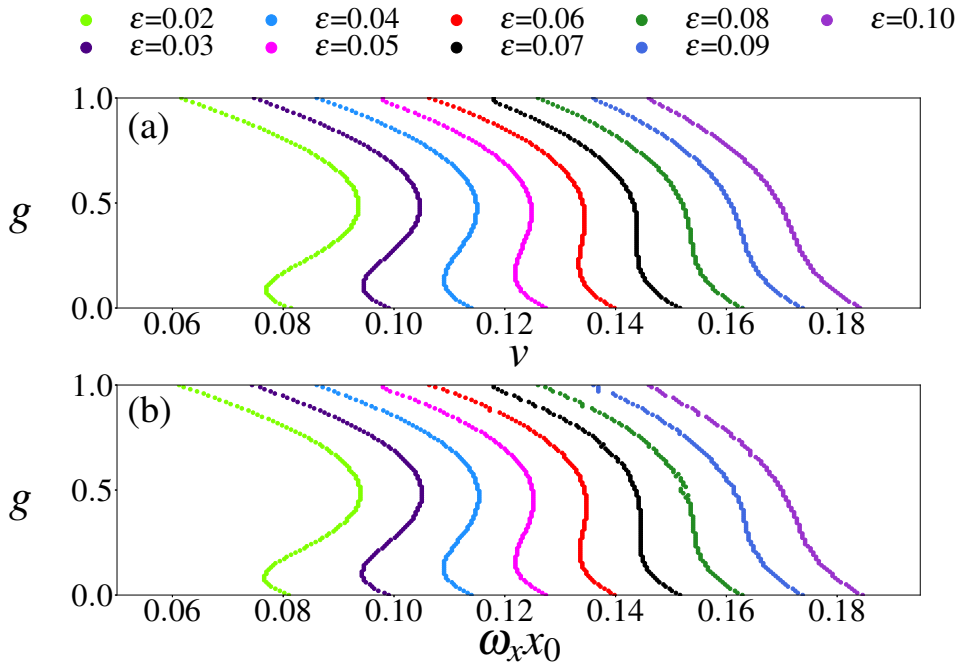

Figure 3.20: Boundaries at which the transmission coefficient for the second component, ψ_2 moves between 0 and 1 (v, g) parameter space for different values of ε with $f = 0.3$ both with and without a harmonic trap with $|x_0| = 40$ fixed.

Chapter 4

Splitting on narrow barriers using geometric potentials

4.1 Overview

In order to be able to utilise the bright soliton for matter-wave interferometry, one requires two coherent solitons which can be brought together on a barrier in a phase-dependent process. A possible scheme to obtain the two solitons is to split a single soliton into two equal parts on a potential barrier. In the limit of a high collisional velocity and a narrow barrier width, the phase imparted by this process is known to be $\pi/2$ [112]. The solitons are to then be recombined on the barrier and the populations on each side of the interferometer afterwards will be dependent on the phase difference accumulated through the different paths the solitons travel. Therefore a valid question is how to obtain very narrow potential barriers to be used for these purposes. A known method to produce subwavelength potential features is through the use of the geometric scalar potential experienced by spatially dependent dressed states. If the intensity of one of the near-resonant alternating electric fields in a Λ-system is changed quickly over a small region of space, then the kinetic energy term of the Hamiltonian acquires a correctional term known as the geometric potential [121–126].

It is known that within the vectorial GPE (VGPE) when three components have all inter- and intra-species scattering lengths equal and negative, a bright

soliton solution of the system is readily found and the population distribution amongst the components possesses an SU(3) symmetry. To see this, let us take the VGPE (in soliton units) with equal scattering lengths and an external potential which is equal for all states,

$$i\partial_t\Psi = -(1/2)\partial_{xx}\Psi + V(x)\Psi + \mathrm{sgn}(g)(\Psi^\dagger\Psi)\Psi, \tag{4.1}$$

where $\Psi^\dagger = (\psi_1^*, \psi_2^*, \psi_3^*)$. Applying a unitary transformation to Ψ gives $\Psi' = U\Psi$ and Eq.(4.1) becomes,

$$Ui\partial_t\Psi = -U(1/2)\partial_{xx}\Psi + UV(x)\Psi + \mathrm{sgn}(g)(\Psi^\dagger U^\dagger U\Psi)U\Psi, \tag{4.2}$$

which is the same as Eq. (4.1) as $U^\dagger U = I_3$, by definition (where I_3 is the 3×3 identity matrix), and we assume this U to have no explicit temporal and spatial dependence. In the scheme, this symmetry does not apply to the relevant VGPE as the unitary transformation matrix has spatial dependence. However, the symmetry is maintained for the nonlinear term which is important because when the soliton passes the barrier, the nonlinear terms will be independent of the populations of the different states (see Sec. 4.8.3).

Assuming all scattering lengths are equal, one can exactly transform the VGPE into the dressed basis, under the effect of couplings between the states. If the dressed basis is spatially dependent, then a term will arise from the kinetic energy term (manifesting as an artificial gauge field). This term depends on the spatial derivatives of the coupling frequency and can thus be tailored using appropriate shapes to form very narrow barriers.

4.2 Geometric potentials

The notion of a geometric phase in quantum physics arises from the behaviour of the Schrödinger equation under an adiabatic following of a trajectory. If a quantum particle is prepared in a state $|\lambda(\vec{R}(t_0))\rangle$, then the adiabatic theorem states that a slowly moving particle will remain in this state as the parameters, $\vec{R}(t)$, evolve. Upon the completion of a cycle, the state will have acquired a phase

$$\gamma_n(t) = i\int_0^t dt' \langle n(\vec{R}(t'))|\frac{d}{dt'}|n(\vec{R}(t'))\rangle = i\int_{\vec{R}(0)}^{\vec{R}(t)} d\vec{R}\,\langle n(\vec{R})|\nabla_{\vec{R}}|n(\vec{R})\rangle \tag{4.3}$$

which is known as the geometric phase as the phase is dependent on the path traversed and not on the dynamical properties of the system.

In atom-light interactions, one can extend this concept to the behaviour of dressed states (the eigenstates of an atom-light coupling Hamiltonian) under spatial variation. In a Λ configuration, such as in Fig. 4.1, one of the eigenstates of the Hamiltonian is a dark state and is de-coupled from the light field (as the eigenvalue is 0). This state is composed of the ground states, $|g_1\rangle$ and $|g_2\rangle$.

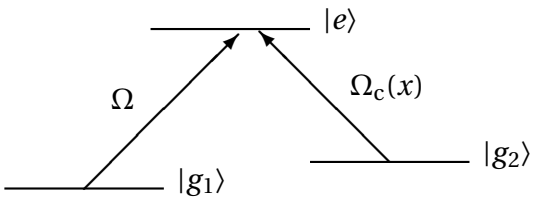

Figure 4.1: The figure shows the energy level diagram used to produce subwavelength potential features.

Let us take the Schrödinger equation in with the couplings between the atoms in the rotating frame,

$$i\frac{\partial \psi_j}{\partial t} = -\frac{1}{2}\frac{\partial^2 \psi_j}{\partial x^2} + \sum_k \frac{\Omega_{jk}}{2}\psi_k, \tag{4.4}$$

where $j,k \in \{g_1, g_2, e\}$, the probe beam Rabi frequency $\Omega_{1e} = \Omega_{e1} = \Omega'(x)$, the control beam Rabi frequency $\Omega_{2e} = \Omega_{e2} = \Omega_c(x)$, and all other $\Omega_{jk} = 0$ (i.e. all on resonance and no direct coupling between the ground states). One can proceed to diagonalise the last term. In doing so, one must bear in mind that the transformation has spatial dependence. This results in additional terms which can be classified as vector and scalar potentials. The vectors, $\psi^T = (\psi_1, \psi_2, \psi_e)$, transform as $\tilde{\vec{\psi}} = U^\dagger \vec{\psi}$ and the operators transform as $\tilde{O} = U^\dagger O U$, thus the kinetic energy transforms as

$$\frac{p^2}{2} \to \frac{\tilde{p}^2}{2} = \frac{U^\dagger p U U^\dagger p U}{2}$$

where

$$U^\dagger p U = -iU^\dagger \partial_x U = -iU^\dagger U \partial_x - iU^\dagger(\partial_x U) = -i\partial_x - A$$

and we define A as $A = iU^{\dagger}(\partial_x U)$. The Schrödinger equation becomes

$$i\frac{\partial\vec{\tilde{\psi}}}{\partial t} = -\frac{(-i\partial_x - A)^2}{2}\vec{\tilde{\psi}} + \tilde{\Omega}\vec{\tilde{\psi}}. \tag{4.5}$$

Therefore one has the possibility of engineering these potentials in multiple component quantum systems with spatially non-uniform couplings. The geometric potentials can be formed in a two component system; however, one has the complication of the decay from the excited state. In the alkali BECs, this would lead to a rapid loss from the excited state. A way around this is to form the potentials in a three-component Λ-system existing in the dark state such that the dressed state consists of the two ground state levels and is de-coupled from the excited state. If the dark state is adiabatically followed then one can form a potential which is dependent on the two Rabi profiles and avoid loss via spontaneous decay.

Extending the number of states allows for increasingly complex gauge structures. In [127] it was shown that in a system with degenerate states, non-Abelian gauge potentials could be formed. The simplest case is that of the tripod system with three degenerate ground states and a single excited level which gives rise to a $U(2)$ gauge structure with non-commuting gauge potential terms [128].

4.3 System details

We require three internal (hyperfine) atomic states, labelled $|g_1\rangle$, $|g_2\rangle$, and $|e\rangle$ in order of increasing energy, coupled in a Λ configuration by light of two frequencies. For simplicity, we consider the couplings to be on-resonant and neglect spontaneous decay from $|e\rangle$. Populating the species in the dark eigenstate of the Λ-system implies that the atomic properties of the excited energy level should have a negligible effect on the system dynamics although loss to and via this state is possible. In order to form an assessment of an experimental system, the case of ^{85}Rb with the initial ground state $|F = 2, M_F - 2\rangle$ coupled to the $|F = 2, M_F = 0\rangle$ state via the D1 line transitions with σ_- and σ_+ beams shall be taken as an example (with dipole matrix elements $\sqrt{2/9}$ and $-\sqrt{5/27}$, respectively, in units of the D1 transition matrix element, $\langle J = 1/2|er|J' = 1/2\rangle$ and a decay rate for the D1 transition of $5.7500 \times 2\pi$Hz). The $|F = 2, M_F - 2\rangle$

state has a wide Feshbach resonance centered at $B_0 = 156\,\mathrm{G}$ with a width of $\Delta = 10.5\,\mathrm{G}$ [96, 97]. The wide width facilitates accurate control of the s-wave scattering length for this state. The background value of the scattering length is $a_{\mathrm{bg}} = -441\,a_0$. The results will show how the action of the splitter (i.e. the relationship between the second transmission function and the phase imparted) is affected by the parameters used to describe the system.

For the case of soliton propagation, it is known that departing from this case of equal scattering lengths, the total density spatial profile could undergo beating effects depending on the relevant scattering lengths and the populations of each component [129]. However, one must note that the use of the dark state in this technique means that the collisional properties of only the two ground states used are relevant as long as the system remains in the dark state. There are coupling terms between the dark state and the $|\pm\rangle$ states (the two other dressed eigenstates which contain the excited level) which arise from the correctional terms. Also, in the desirable limit of a narrow crossover region as well as fast soliton collisions, the soliton spends little time in the second ground state. As the main component of the dark state changes from $|g_1\rangle$ to $|g_2\rangle$, so will the scattering length change rapidly from a_{11} to a_{22} which may affect the interaction between the soliton with the barrier.

The appropriate quasi-1D vector Gross–Pitaevskii equation (GPE) for a BEC of N mass m atoms, transversely confined by a tight harmonic trapping potential of angular frequency ω_r, is given by Eq. (2.58) with $j,k \in \{1,2,e\}$, $g_{jk}^{\mathrm{1D}} = 2\hbar\omega_r a_{jk}$, the probe beam Rabi frequency $\Omega_{1e} = \Omega_{e1} = \Omega'(x)$, the control beam Rabi frequency $\Omega_{2e} = \Omega_{e2} = \Omega_{\mathrm{c}}(x)$, and all other $\Omega_{jk} = 0$. The spatially-dependent coupling is key, as it leads to a spatially-dependent dressed-state basis in which an artificial gauge field term appears [121, 122, 130] in the form of the vector potential $A = iU^{\dagger}\partial_x U$. This results in the geometric scalar potential

$$V(x) = \langle d|\,\frac{A^2}{2}\,|d\rangle = \frac{\hbar^2}{2m}\left(\frac{\Omega'\partial_x\Omega_{\mathrm{c}} - \Omega_{\mathrm{c}}\partial_x\Omega'}{\Omega'^2 + \Omega_{\mathrm{c}}^2}\right)^2 \tag{4.6}$$

for the dark state $|d\rangle$.

In Fig. 4.2 we illustrate our single narrow barrier scheme, where we consider equal-width zeroth- and first-order Hermite–Gaussian modes for the probe and control beams, respectively. We express the widths of the beams as l and express the Rabi frequencies as

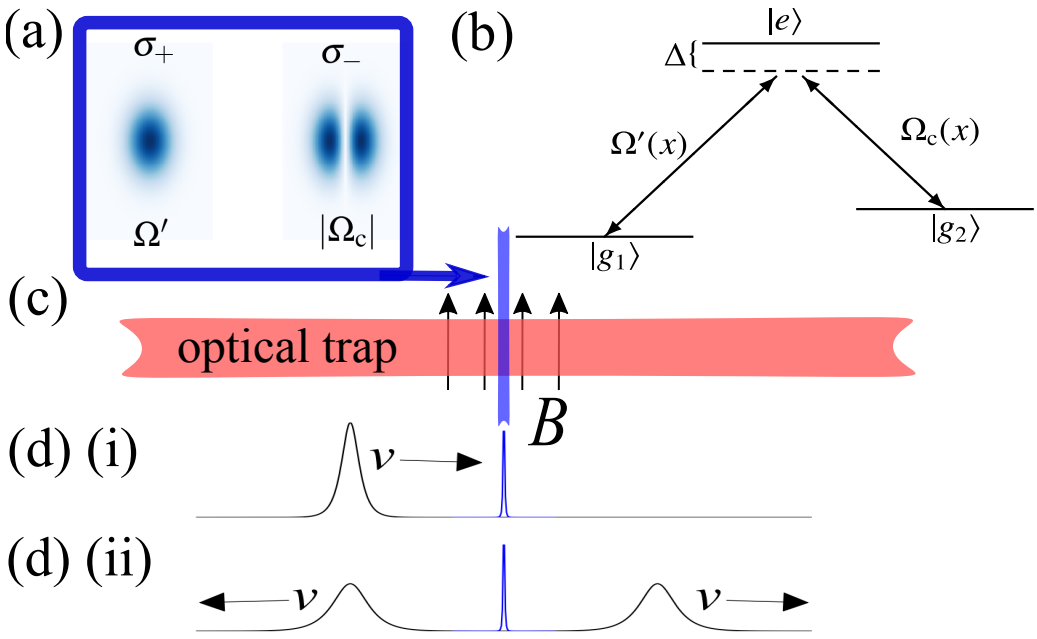

Figure 4.2: The figure shows the proposed arrangement used to coherently split the parent soliton into two equally sized daughter solitons. (a) shows the two beam profiles for Ω' and Ω_c in the x,z plane at $y=0$. (b) shows the level configuration used in the system. To consider some of the properties of this system, as an example the ground states $|g_1\rangle$ and $|g_2\rangle$ are taken to be the states $|F=2,M_F=-2\rangle$ and $|F=2,M_F=0\rangle$, respectively, of ^{85}Rb coupled to $|e\rangle=|F'=3,M_F'=1\rangle$ by the D1 line. (c) shows the optical waveguide in the x,y at $z=0$ which is to contain the solitons. It is highly anisotropic such that the solitons are strongly confined in the transverse directions. A magnetic bias field is to be applied parallel to the beams forming the barrier in order to provide a quantization axis. (d) shows the initial soliton propagating along the x direction with a velocity, v, which is subsequently split into two equally sized solitons which move apart. The solitons are considered to propagate inside a ring trap in order that they will eventually recombine on the barrier. Alternatively, the recombination can be achieved using a weak axial harmonic trapping so that the solitons undergo sinusoidal motion with the barrier at the centre.

$$\Omega' = \Omega_0 l^{1/2} \phi_0 \tag{4.7}$$

$$\Omega_c = \Omega_1 l^{1/2} \phi_1, \tag{4.8}$$

where

$$\phi_0(x;l) = \left(\frac{2}{\sqrt{\pi} l}\right)^{1/2} \exp\left(-\frac{x^2}{l^2}\right) \tag{4.9a}$$

$$\phi_1(x;l) = \left(\frac{8}{\sqrt{\pi} l}\right)^{1/2} \frac{x}{l} \exp\left(-\frac{x^2}{l^2}\right). \tag{4.9b}$$

Then

$$h(x) = \frac{\Omega_c}{\Omega'} = \frac{\Omega_1 \phi_1}{\Omega_0 \phi_0} = \frac{2\Omega_1 x}{\Omega_0 l}, \tag{4.10}$$

and thus w can be defined as

$$w = \frac{l}{2} \frac{\Omega_0}{\Omega_1}. \tag{4.11}$$

Note that l is the diffraction-limited width of the laser beams which we take to be $2\sqrt{2}$ in our numerical studies and also that we convert between $\Omega \equiv \Omega'(0)$ and Ω_0 by,

$$\Omega = \Omega_0 \sqrt{\frac{2}{\sqrt{\pi}}}. \tag{4.12}$$

By construction, the common envelope function then cancels out in the resulting dark state

$$|d\rangle = \frac{|g_1\rangle}{[1+(w/x)^2]^{1/2}} - \frac{(w/x)\,|g_2\rangle}{[1+(w/x)^2]^{1/2}}, \tag{4.13}$$

and [via Eq. (4.6)] the resulting geometric scalar potential is

$$V_h(x) = \frac{\hbar^2}{2mw^2} \frac{1}{[1+(x/w)^2]^2}. \tag{4.14}$$

In physical terms,

$$w = \frac{\delta l}{2} \sqrt{\frac{P_0}{P_1}}, \tag{4.15}$$

where δ is the (order unity) ratio between dipole transition matrix elements, and P_n represents the n^{th} order Hermite–Gaussian beam power. From Eq. (4.14), one sees that the shape of the potential formed is independent of the value of Ω but instead depends on the form of $h(x)$ defined in Eq. (4.10). However, Ω is the minimum of the energy difference between the eigenstates $|d\rangle$ and $|-\rangle$ (at $x = 0$) and could affect the loss of the population of $|g_1\rangle$ into the states $|e\rangle$ and $|g_2\rangle$ during the barrier crossing. Also note that, in terms of experimental

parameters, w depends on the relative values of the dipole matrix elements for the D1 transitions as well as the relative laser intensities.

In order to examine the effects of deviations from the idealised system, we numerically model the VGPE (Eq. (2.58)) in the soliton unit system where $\hbar = m = 2\hbar\omega_r|g_{11}^{1D}|N = 1$ (see Eqs. (2.53c)) and make the simplifications that $-a_{ij}/|a_{11}| = g$ and $\Delta = \Gamma = 0$, where Δ is the detuning and Γ is the decay rate of the excited state $|e\rangle$. Γ should have minimal effects on the system at the regimes we wish to consider due to the atoms being in the dark state. If $\Delta \neq 0$ then additional couplings between the $|d\rangle$ and $|\pm\rangle$ would appear in the equations of motion (see App. A.1). This gives the dimensionless equations

$$\begin{aligned} i\partial_t\psi_1 &= -\frac{\partial_{xx}}{2}\psi_1 - (g|\psi_2|^2 + |\psi_1|^2 + g|\psi_e|^2)\psi_1 \\ &\quad + \frac{\Omega'}{2}\psi_e, \end{aligned} \tag{4.16a}$$

$$\begin{aligned} i\partial_t\psi_2 &= -\frac{\partial_{xx}}{2}\psi_2 - g(|\psi_2|^2 + |\psi_1|^2 + |\psi_e|^2)\psi_2 \\ &\quad + \frac{\Omega_c}{2}\psi_e, \end{aligned} \tag{4.16b}$$

$$\begin{aligned} i\partial_t\psi_e &= -\frac{\partial_{xx}}{2}\psi_e - g(|\psi_2|^2 + |\psi_1|^2 + |\psi_e|^2)\psi_e \\ &\quad + \frac{\Omega_c}{2}\psi_2 + \frac{\Omega'}{2}\psi_1. \end{aligned} \tag{4.16c}$$

The relevant parameters in this model are: the length, w (defined in Eq. (4.11) - we sometimes label this quantity instead as $\Omega_1/\Omega_0 = l/(2w)$ in order to reflect the experimental picture), representing the size of the region over which the dark state changes from being dominated by $|g_1\rangle$ to being dominated by $|g_2\rangle$; Ω, the strength of the Rabi frequency coupling the $|g_1\rangle$ and $|e\rangle$ levels; and g, the ratio between the scattering length a_{11} and the other scattering lengths in the system. Henceforth, unless stated otherwise, all quantities will be presented in this unit system. We present some results found using a single component GPE. This approach assumes that the soliton remains in the dark state and so it should be stressed that the single component is not an atomic state but the dressed dark state.

4.4 The requirement of narrow barriers

In Sec. 4.7 the improvement of an interferometric sequence by decreasing the value of w is demonstrated using single component 1DGPE simulations. In this system, the width and area of the barrier are related to the value of w (which describes the relative powers of the two laser beams used to couple the two ground states to the excited state). The relationship is favourable in the sense that decreasing w increases the barrier area whilst decreasing the barrier width, however (as shown in Sec. 4.5.2), the amount of tunnelling in the system is fixed and does not approach the δ-function limit wherein all of the transmitted soliton must tunnel through the barrier. In order to understand some of the properties of solitons split on potential barriers and their suitability for interferometry, let us first examine the case of solitons incident on Gaussian barriers which, in principle, have independently controllable widths and areas. Let us meanwhile note that the purpose of the three-state scheme is that the barrier formed possesses a lower limit on the width below the diffraction limit and that the Gaussian barriers shown in Fig. 4.3 may not all adhere to this limit for some soliton experiments (use of the soliton unit scheme implies that the conversion to dimensional units depends on the values of g_{1D}, m and N).

In Fig. 4.3, the characteristics pertinent to interferometry using a Gaussian barrier are explored for different values of the width and area of the barrier, denoted by σ and q, respectively. The form of the Gaussian barrier is then

$$V_G(x;\sigma) = \frac{q}{\sqrt{2\pi}\sigma} \exp\left(-\frac{x^2}{2\sigma^2}\right). \tag{4.17}$$

4.5 Characterising the barrier

4.5.1 Analytical approach

The effective barrier produced by this scheme takes the form of a squared Lorentzian with the profile

$$V_h(x) = \frac{1}{2w^2} \frac{1}{\left[1+(x/w)^2\right]^2}, \tag{4.18}$$

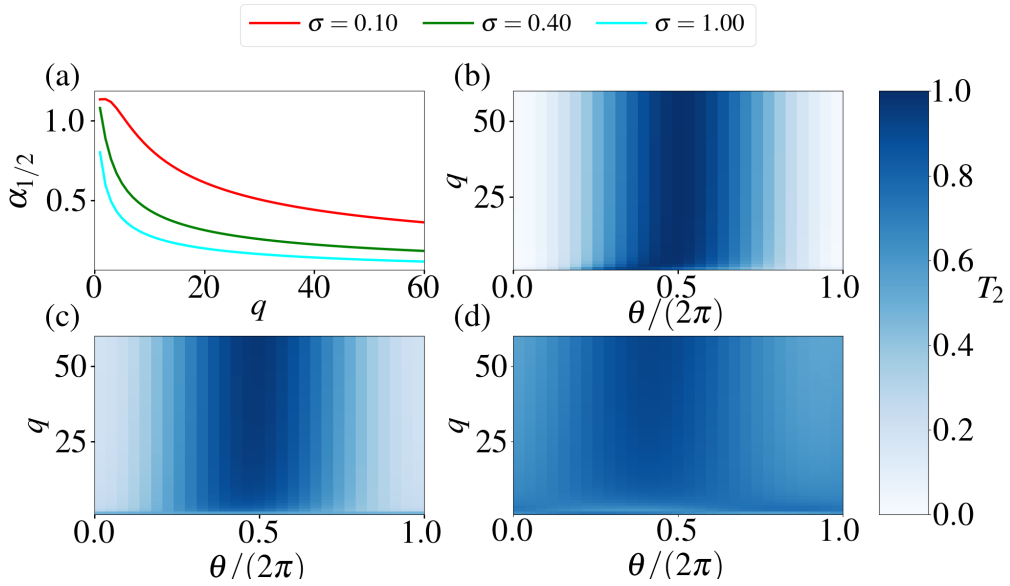

Figure 4.3: The figure shows how the interactions between the solitons and a Gaussian barrier are affected by the barrier width and the area. In (a), the ratio between the velocity and the area where the soliton is split into equal daughter solitons is plotted against the barrier area for different values of the barrier width. In (b)–(d), the plots show the how the value of T_2 varies with the imparted phase, θ for different values of q (given an initial transmission $T_1 = 1/2$) for $\sigma = 0.10$ in (b), $\sigma = 0.40$ in (c) and $\sigma = 1.00$ in (d).

with an area depending on the width, w, as $A = \pi/4w$ and a height given by $H = 1/2w^2$. We are interested in the difference in the transmission curve between a single component soliton passing through a barrier of the form $V_h(x)$ and a barrier of the form

$$V_\delta(x) = \frac{\pi}{4w}\delta(x), \tag{4.19}$$

(the δ-function with the same area as V_h). For the δ-function, the transmission curve for large velocities (in the linear interaction regime) is known to be

$$\lim_{v\to\infty}[T_\delta(\alpha)] = \frac{\alpha^2}{1+\alpha^2}, \tag{4.20}$$

where α is defined as $4vw/\pi$. In order to obtain a fitting in a similar way for the barrier, V_h, one can approximate the barrier as a sech^2 barrier (integrable Rosen–Morse potential) with the same height and area as V_h. Barriers of this shape have a known transmission curve for linear waves (which we can assume for high impact velocities where non-linear effects during the splitting will be

less pronounced). Such a barrier takes the form

$$V_{\mathrm{RM}} = \frac{1}{2w^2}\operatorname{sech}^2\left(\frac{4x}{\pi w}\right), \tag{4.21}$$

and the corresponding transmission curve is then

$$T_{\mathrm{RM}}(\alpha) = \frac{\sinh^2\left(\frac{\pi^3\alpha}{16}\right)}{\sinh^2\left(\frac{\pi^3\alpha}{16}\right) + \cosh^2\left(\frac{\pi}{2}\sqrt{\left(\frac{\pi}{2}\right)^2 - 1}\right)}. \tag{4.22}$$

In order to compare the Lorentz-squared barrier with the analytically soluble (in the fast soliton limit) Rosen–Morse barrier, we found the corresponding sech^2 barrier with the same height and area. Alternatively, one could fit the sech^2 barrier with the same area and width (FWHM) as V_h. This potential takes the form

$$V_{\mathrm{RMW}} = \frac{\pi}{8\gamma w^2}\operatorname{sech}^2\left(\frac{x}{\gamma w}\right), \tag{4.23}$$

where $\gamma \equiv \ln(\sqrt{2}+1)/\sqrt{\sqrt{2}-1} \approx 0.73$, and the corresponding transmission curve is then

$$T_{\mathrm{RMW}}(\alpha) = \frac{\sinh^2\left(\frac{\pi^2\gamma\alpha}{4}\right)}{\sinh^2\left(\frac{\pi^2\gamma\alpha}{4}\right) + \cosh^2\left(\frac{\pi}{2}\sqrt{\pi\gamma - 1}\right)}. \tag{4.24}$$

Note that Eqs. (4.22) & (4.24) imply that the transmission curve for the produced barrier can never approach the transmission curve for the δ-function, Eq. (4.20). This is ultimately due to the fact that the width and area of the barrier, Eq. (4.14) (and thus, by definition, Eqs. (4.21) & (4.23)) are both dependent on the parameter w. This is a limitation of forming narrow barriers using this scheme.

Figure 4.4 shows the transmission against α expected in the high-velocity limits for the barriers V_{RM}, V_{RMW} & V_δ (given by Eqs. (4.21), (4.23) & (4.19), respectively). Note that the transmission for V_{RM} and V_{RMW} depends only on α (the ratio between the velocity and the area) and does not change with w in the theoretical treatment. Figure 4.5, however, shows the transmission curves obtained numerically for the V_h and the V_δ barriers for different values of w and scaled so as to be plotted against the parameter, α; the ratio between velocity and area. We can see that as w decreases and the equal splitting velocity (resulting in a transmission of 1/2) increases, the the transmission curves approach the theoretical (linear) values given by Eqs. (4.20 & 4.22) shown by the dotted lines.

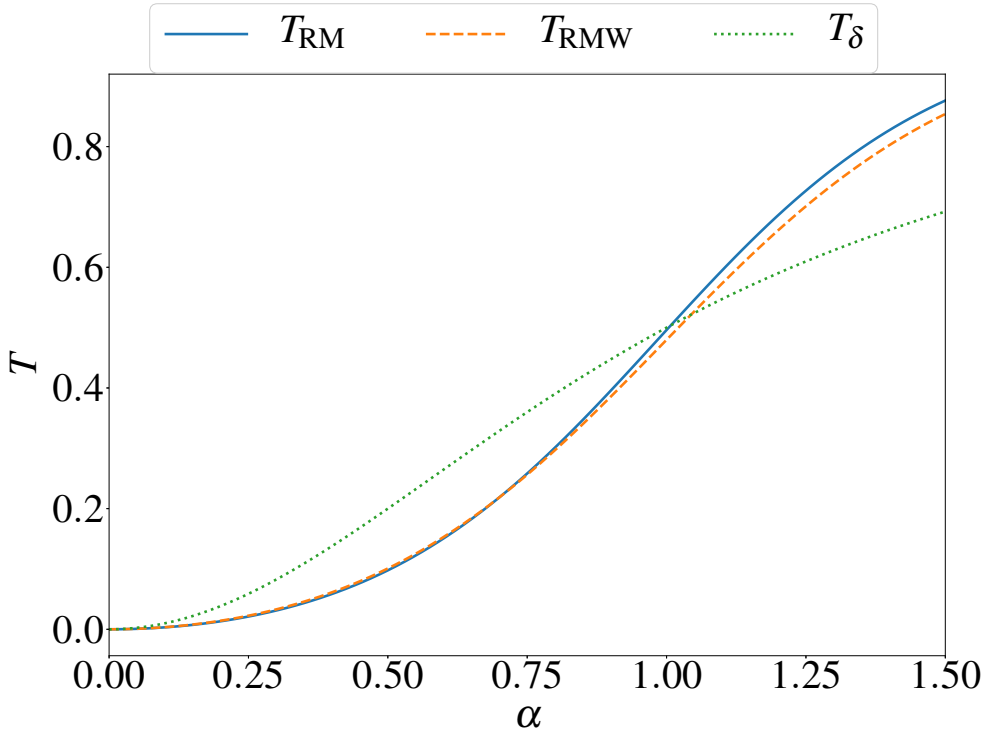

Figure 4.4: The plot shows the different theoretical transmission curves (plotted against thee ratio between the velocity and the barrier area ,α) for the V_{RM} and V_{RMW} barriers (which approximate the V_h barrier using a sech^2 function with the same area and equal height (FWHM) and width, respectively) and the δ-function barrier, V_δ.

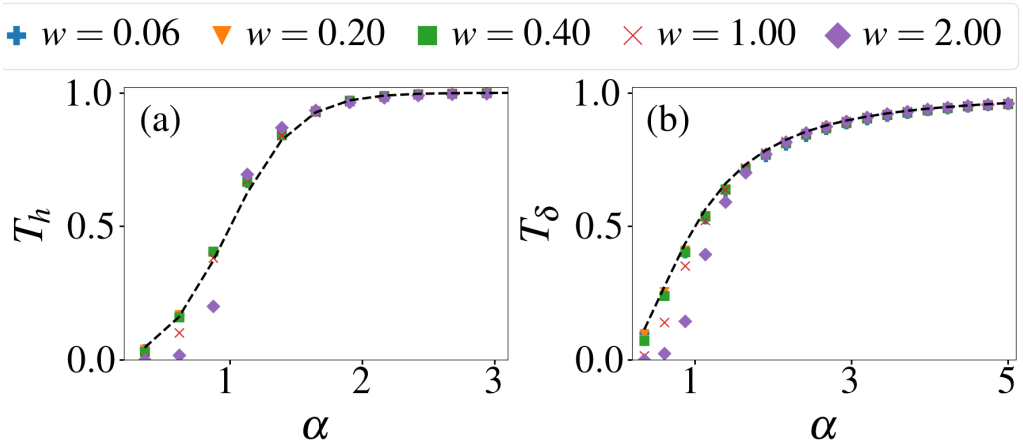

Figure 4.5: The plot shows the transmission for increasing values of α, which denotes the ratio between the velocity and the barrier area, of a bright soliton interacting with the barriers V_h (a) and V_δ (b) for different values of w in the 1DGPE. The dotted lines in (a) and (b) show the curves given by Eqs. (4.22 & 4.20), respectively. As expected, we see closer agreement with the transmission curves obtained by the theoretical analysis for both barriers with decreasing w.

4.5.2 Tunnelling and the barrier V_h

When the solitons are split into two equally sized daughter solitons by the potential barrier, we also need to ensure that the outgoing solitons do not posses different speeds. Depending on the interferometer geometry, the two different velocity daughter solitons could hinder the ability to form an interferometer scheme. As the barriers used to split the solitons become narrower, this effect should be decreased.

For increasing impact velocities, we need decreasing widths of the barrier in order to be in the tunnelling regime [114]. The V_h barrier (Eq. (4.14)) has an area of $(\pi/4w)$ and thus, as the width w is decreased, the area of the barrier must increase. The ratio between the kinetic energy and the height (barrier maximum) is given by

$$\gamma_h = (vw)^2. \tag{4.25}$$

Using the definition of $\alpha = 4vw/\pi$, this is equal to

$$\gamma_h = \left(\frac{\pi}{4}\right)^2 \alpha_{1/2}^2, \tag{4.26}$$

where $\alpha_{1/2}$ is the value of α for which the transmission is 1/2. This depends on the area of the barrier as well as the shape. For the barrier V_h with related area and height which both depend on the value of w, $\alpha_{1/2}$ was found numerically and is close to $\alpha_{1/2} \approx 0.96$ with a slight increase as w decreases. As the δ-function is defined to be infinitely high, γ_δ (the ratio between the kinetic energy and the height of the δ-function) is equal to zero, given that the soliton is partially transmitted at finite velocities. For the barrier, V_h, γ_h is then $\gamma_h \approx (\pi/4)^2(0.96)^2 \approx 0.57$ and thus cannot be lowered by decreasing w. This is an unavoidable consequence of obtaining the barrier in this way. Fundamentally, the barrier comes from the $A^2/2$ correction term in the kinetic energy (where $A = iU^\dagger(\partial_x U)$). This gives us the shape of the barrier in the form of Eq. (4.6). However, the advantage of this system is that as the width of the barrier is decreased by increasing the ratio Ω_1/Ω_0, we remain in the tunnelling regime for increasing equal splitting velocities.

Let us redefine $h(x)$ as a higher order polynomial

$$h(x) = \left(\frac{x}{w}\right)^n. \tag{4.27}$$

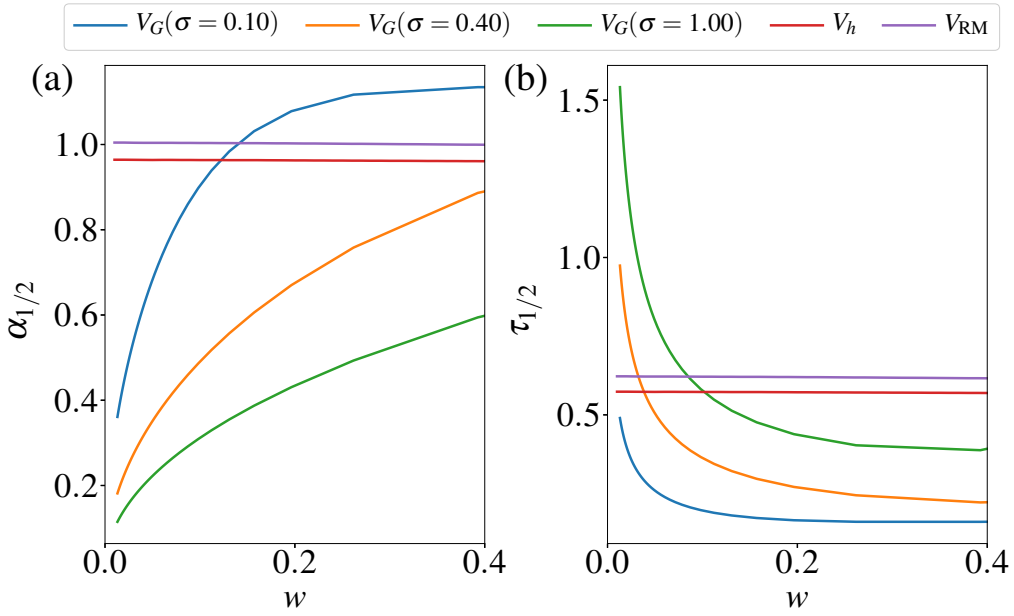

Figure 4.6: The plot shows data taken from single component GPE simulations for the splitting of bright solitons by different potential barriers. (a) shows the value of $\alpha_{1/2}$ (found numerically as the ratio between the soliton velocity and the barrier area when the soliton is split into equally sized transmitted and reflected solitons) for different barriers (three Gaussian barriers with different widths denoted by σ, V_h and V_{RM}) against w as defined in Eqs. (4.14, 4.21 & 4.17). (b) shows the tunnelling parameter, $\gamma = T/H$ against w.

Computing the area of the barrier potential gives us

$$\int_{-\infty}^{\infty} \frac{1}{2}\left(\frac{\mathrm{d}h}{\mathrm{d}x}\right)^2 \frac{1}{(1+h^2)^2}\frac{\mathrm{d}x}{\mathrm{d}h}\mathrm{d}h = \frac{n}{2w}\int_{-\infty}^{\infty}\frac{h^{1-1/n}}{(1+h^2)^2}\mathrm{d}h. \tag{4.28}$$

This integral can be evaluated using Cauchy's integral formula to give

$$A = \frac{\pi n}{4w}\cos\left(\frac{\pi}{2}\left[1-\frac{1}{n}\right]\right). \tag{4.29}$$

We can see that increasing n increases the area which is not favourable for the convergence to a δ-function. This suggests that the first order definition for $h(x)$ is optimal.

The aspects of the barrier important when discussing the barrier as a splitter for interferometry are the area and the height or width. As we want to discuss the similarity between the finite barriers and an idealised δ-function, we consider the area fixed and the height infinite or, alternatively, the width zero. The corresponding Gaussian with the same height and area as the barrier V_h is of

the form

$$V_G(x) = \frac{1}{2w^2} \exp\left(\frac{-4x^2}{\pi w^2}\right). \tag{4.30}$$

We can thus interpret σ as $\sigma = \sqrt{\pi/8}\,w$ (roughly $\sigma = 0.63\,w$) as a useful relationship between a similar Gaussian shape barrier (in the same manner as V_{RM}) to V_h in order to compare the width with the conventional barrier produced by a single beam.

Increasing the velocity of the soliton splitting is favourable as we can neglect nonlinear effects during the splitting. With this scheme, we can increase the equal splitting velocity and decrease the width of the barrier accordingly such that we remain always in the quantum tunnelling regime. However, due to the fixed relationship between the height, width and area of the barrier produced by the scheme, we cannot approach a limit wherein the soliton interacts with the barrier in the same way as it would with a δ-function. We demonstrate a different limit where the soliton interferometer, using the barrier produced by the scheme, possesses the same characteristics as it would using a δ-function.

4.6 Dynamics in the three level system

4.6.1 Analytical approach

In the basis $\{g_1, g_2, e\}$, the non-diagonal potential term appearing in the GPE is

$$\Omega = \begin{pmatrix} 0 & 0 & \Omega'/2 \\ 0 & 0 & \Omega_c/2 \\ \Omega'/2 & \Omega_c/2 & 0 \end{pmatrix}. \tag{4.31}$$

The diagonalisation of this matrix yields

$$\Omega = \begin{pmatrix} 0 & 0 & 0 \\ 0 & \bar{\Omega}/2 & 0 \\ 0 & 0 & -\bar{\Omega}/2 \end{pmatrix}, \tag{4.32}$$

where $\bar{\Omega} = \sqrt{\Omega'^2 + \Omega_c^2}$. The unitary transformation matrix, U is

$$U = \begin{pmatrix} -\Omega_c/\bar{\Omega} & \Omega'/\bar{\Omega} & 0 \\ \Omega'/\sqrt{2}\bar{\Omega} & \Omega_c/\sqrt{2}\bar{\Omega} & 1/\sqrt{2} \\ \Omega'/\sqrt{2}\bar{\Omega} & \Omega_c/\sqrt{2}\bar{\Omega} & -1/\sqrt{2} \end{pmatrix}. \tag{4.33}$$

From this we can find A as

$$A = \frac{-i\Omega'(\partial_x\Omega_c)}{\bar{\Omega}^2}\begin{pmatrix} 0 & 1/\sqrt{2} & 1/\sqrt{2} \\ -1/\sqrt{2} & 0 & 0 \\ -1/\sqrt{2} & 0 & 0 \end{pmatrix}, \tag{4.34}$$

and A^2 as

$$A^2 = \left(\frac{\Omega'(\partial_x\Omega_c)}{\bar{\Omega}^2}\right)^2\begin{pmatrix} 1 & 0 & 0 \\ 0 & 1/2 & 1/2 \\ 0 & 1/2 & 1/2 \end{pmatrix}. \tag{4.35}$$

The dressed states in terms of the atomic energy level states are

$$\psi_d = \left(\Omega_c/\bar{\Omega}\right)\psi_1 - \left(\Omega'/\bar{\Omega}\right)\psi_2, \tag{4.36}$$

$$\psi_+ = \left(\Omega'/\bar{\Omega}\right)\psi_1 + \left(\Omega_c/\bar{\Omega}\right)\psi_2 + \left(1/\sqrt{2}\right)\psi_e, \tag{4.37}$$

$$\psi_- = \left(\Omega'/\bar{\Omega}\right)\psi_1 + \left(\Omega_c/\bar{\Omega}\right)\psi_2 - \left(1/\sqrt{2}\right)\psi_e. \tag{4.38}$$

The geometric potential we are interested in is that experienced by the dark state which is the $A^2/2$ term from the kinetic energy. Assuming Ω' to be constant, this term is

$$V(x) = \frac{[\Omega'(\partial_x\Omega_c)]^2}{2\bar{\Omega}^4}. \tag{4.39}$$

Aside from the scalar potential term, there are couplings between the dark state and the other eigenstates arising from the cross terms between the operators p and A.

The coupling terms between the bright and dark states are given by

$$\frac{i}{2}(\partial_x A + A\partial_x) = \frac{i}{2}[(\partial_x A) + 2A\partial_x],$$

where A is given by

$$A = \frac{i\Omega'\partial_x\Omega_c}{\sqrt{2}\bar{\Omega}^2}\begin{pmatrix} 0 & -1 & -1 \\ 1 & 0 & 0 \\ 1 & 0 & 0 \end{pmatrix} \Rightarrow (\partial_x A) = \frac{1}{\sqrt{2}}\left(\frac{i\Omega'(\partial_{xx}\Omega_c)}{\bar{\Omega}^2} + i\Omega'(\partial_x\Omega_c)(\partial_x\bar{\Omega}^{-2})\right)\begin{pmatrix} 0 & -1 & -1 \\ 1 & 0 & 0 \\ 1 & 0 & 0 \end{pmatrix}$$

$$\Rightarrow -\frac{pA + Ap}{2} = \frac{1}{\sqrt{2}}\left(\frac{\Omega'(\partial_{xx}\Omega_c)}{2\bar{\Omega}^2} + \frac{\Omega'\Omega_c(\partial_x\Omega_c)^2}{\bar{\Omega}^4} - \frac{\Omega'(\partial_x\Omega_c)\partial_x}{\bar{\Omega}^2}\right)\begin{pmatrix} 0 & -1 & -1 \\ 1 & 0 & 0 \\ 1 & 0 & 0 \end{pmatrix}.$$

Therefore the coupling between the dark state and the bright state, $|b\rangle = \frac{1}{\sqrt{2}}(|+\rangle + |-\rangle)$, is given by

$$(|b\rangle\langle d| - |d\rangle\langle b|)\left(-\frac{\Omega(\partial_{xx}\Omega_c)}{2\bar{\Omega}^2} + \frac{\Omega'\Omega_c(\partial_x\Omega_c)^2}{\bar{\Omega}^4} - \frac{\Omega'(\partial_x\Omega_c)}{\bar{\Omega}^2}\partial_x\right).$$

When the soliton crosses the effective barrier, there is a non-zero possibility of losing some population from the soliton to the lower energy state, $|-\rangle$, due to the coupling between this state and the dark state, $|d\rangle$. This coupling is of the order, $H = 1/2w^2$ and Ω is the difference in energy between the dark state and the state $|-\rangle$ at $x = 0$. Thus the condition which is to be satisfied is that $\Omega \gg 1/2w^2$ where $1/2w^2 = H$ is the barrier height. We can define a constant of proportionality, β, as

$$\beta = \frac{\Omega}{H} = 2w^2\Omega = 4\Omega\left(\frac{\Omega_0}{\Omega_1}\right)^2. \tag{4.40}$$

Figure 4.7 shows both the values of Ω corresponding to constant β and vice versa for numerous values of Ω_1/Ω_0.

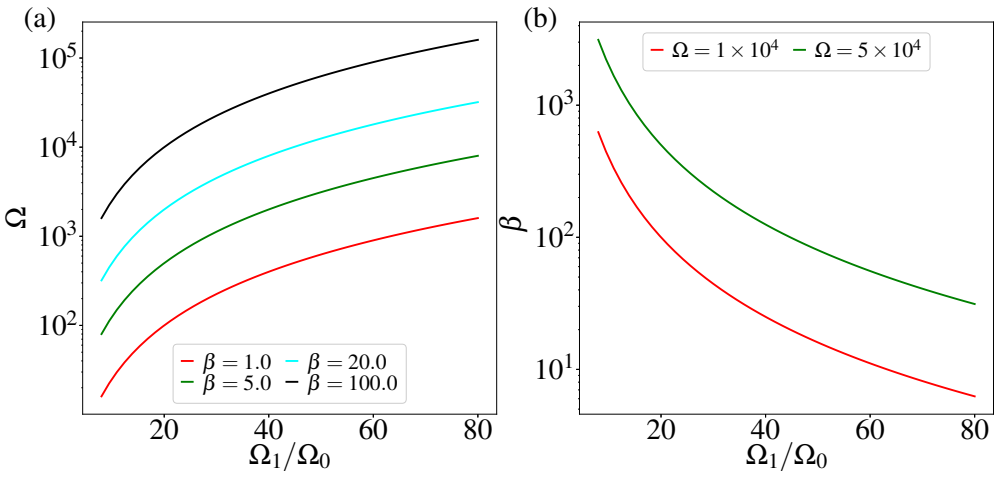

Figure 4.7: The figure shows the relationship between Ω, β and Ω_1/Ω_0. In (a), the curves show the values of Ω against Ω_1/Ω_0 for various values of fixed β whereas (b) shows the values of β corresponding the different values of Ω_1/Ω_0 for two values of fixed Ω (used in Fig. 4.15).

Thus, a higher value of Ω should be more favourable for use in a soliton interferometry sequence. In experiments, there are upper limits on what values of Ω can be achieved originating from the maximum available laser power and also limits where necessary approximations hold (i.e. the three-level system). The

results shown which were obtained from numerical simulations of the barrier scheme possess computational limitations which do not apply to an experimental system. An upper limit on Ω arises because the values of the couplings need to be small enough that the dynamics can be modelled accurately in a feasible time frame. The nature of the system requiring 3×3 matrix operations already results in long computation times. The addition of these upper limits as well as the utility of knowledge on the effect of low Ω values warrant an investigation into the relationship between Ω and the imperfections of the system.

4.6.2 Numerical results

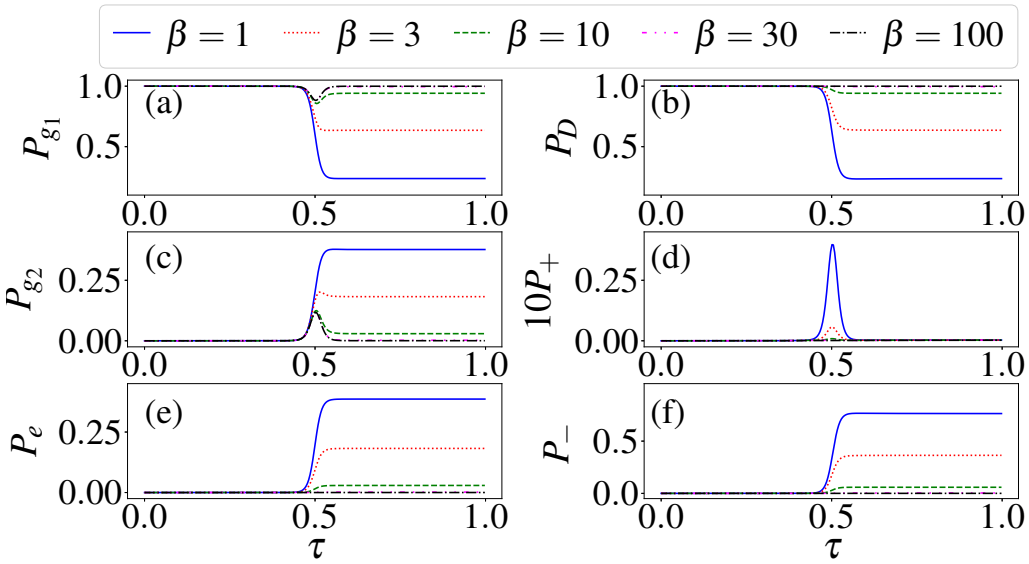

Figure 4.8: The figure shows the populations in each state during the splitting of a bright soliton on the barrier - in the left column (panels (a), (c) & (e)) the bare atomic basis $\{g_1, g_2, e\}$ and in the right column (panels (b), (d) & (f)) the dressed basis $\{d, +, -\}$ (with the $|+\rangle$ state scaled by a factor of 10) - against the scaled time, τ, for various values of β which is the ratio between the barrier height and the coupling frequency, Ω, for $\Omega_1/\Omega_0 = 10$ (with $g = 1$).

Figures 4.8 & 4.9 show the populations in the states in both the bare atomic and the dressed basis as a function of the scaled time, τ, for various values of β for $\Omega_1/\Omega_0 = 10$ and $\Omega_1/\Omega_0 = 20$, respectively. From these figures, one notices that the amount of loss depends mostly on the value of β and not on Ω_1/Ω_0. This is because the states are separated by Ω at the point of closest approach and are coupled on the order of $H = 1/2\,w^2$ during the barrier passage. Thus the ratio

between Ω and $1/2w^2$ determines how much is lost from the dark state. The maximum population of the state $|g_2\rangle$ depends only on Ω_1/Ω_0 for large values of β. This is because the dark state quickly changes from being dominated by $|g_1\rangle$ to $|g_2\rangle$ and then back to $|g_1\rangle$ and some population will transfer while the atoms remain in the dark state. However, the bright states $|\pm\rangle$ are also comprised of mostly $|g_2\rangle$ away from the barrier and so loss into these states will result in a higher value of $\max(P_{g_2})$.

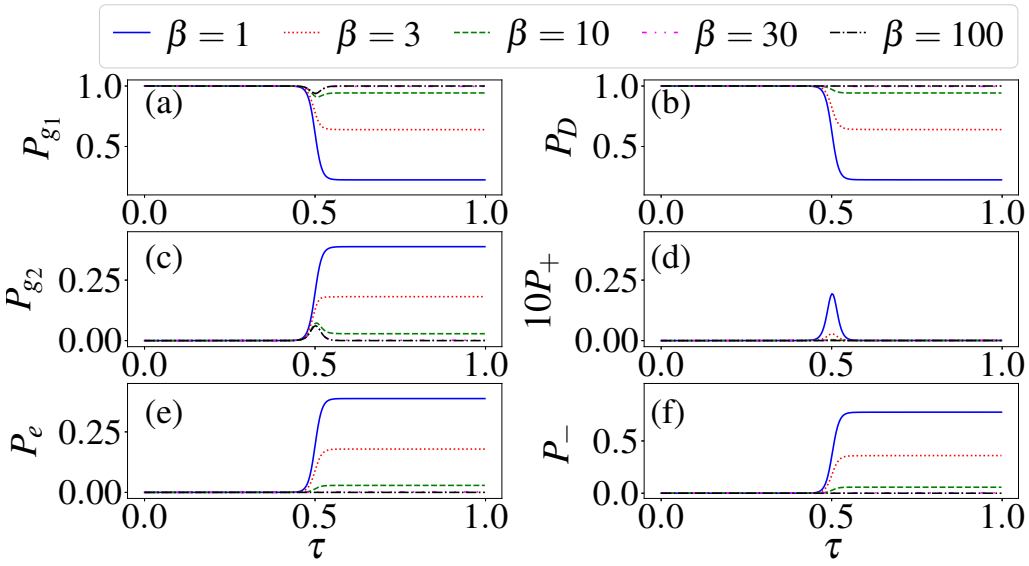

Figure 4.9: The figure shows similar data to Fig. 4.8 but with the ratio $\Omega_1/\Omega_0 = 20$ (with $g = 1$).

In Fig. 4.10, for values of Ω_1/Ω_0 of 10 and 20 we plot the maximum occupation of the state $|g_2\rangle$ in (a) and the loss from the dark state after the barrier crossing in (b) against the parameter β given by Eq. (4.40). This shows the important aspects in Figs. 4.8 & 4.9 which will influence the usefulness of the splitter in an interferometer. These are the occupation of the other ground state, $|g_2\rangle$ which may possess different scattering properties to $|g_1\rangle$ as well as the soliton remaining in $|g_1\rangle$ after the splitting. We show here that these quantities are minimised for both large β and Ω_1/Ω_0.

We anticipate that, as w decreases (and so the equal splitting velocity increases), the properties of the states $|g_2\rangle$ and $|e\rangle$ will have less influence on the interferometer output. This is because the soliton spends less time in these states due to the higher velocity when passing/reflecting off the barrier as well as the narrower region where Ω_c is larger than Ω. We have plotted the popula-

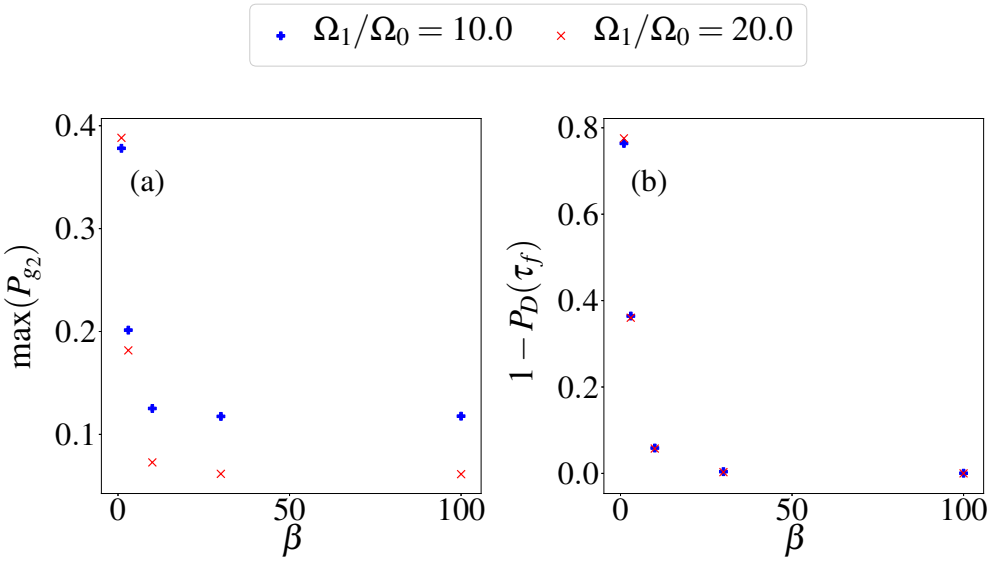

Figure 4.10: The figure shows (a) the maximum population of the state $|g_2\rangle$ over the course of the splitting of the soliton and (b) the loss from the dark state after the splitting of the soliton against β, the ratio between the barrier height and the coupling frequency, Ω, for various values of Ω_1/Ω_0.

tions in these states against time for different values of w in Fig. 4.11, as well as the total time spent in the state $|g_2\rangle$ in (d). In order that the curves line up, the x axis has been scaled to run from 0 to $L/2v$, where L is the circumference of the interferometer, for axes (a)–(c). Figure 4.11 also shows how the transmission is affected by having g (the ratio between the value of the other scattering lengths in the system and the magnitude of the scattering length of the initial ground state) not equal to 1. We note that the ideal case is for $g = 1$, which corresponds to all scattering lengths being negative and equal, as the soliton width is independent of the population distribution in the three-level system. We vary g between -40 and 40 where $|a_{bg}|/|a_{11}| \approx 40$ for ^{85}Rb and $a_{11} \approx -12a_0$ lies in the stable soliton region [78, 131, 132]. One can see that as w decreases, the effect of the difference is diminished.

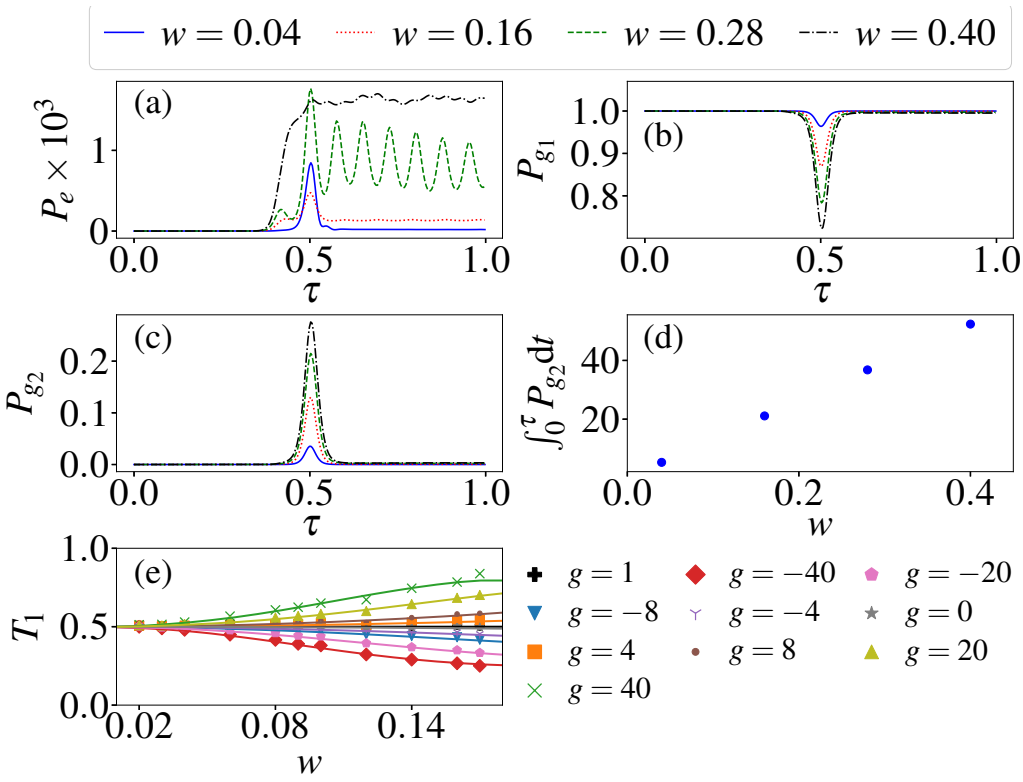

Figure 4.11: The figure shows the populations of the three atomic states against the re-scaled time, τ. (a) shows the population of state $|e\rangle$, (b) the population of $|g_1\rangle$ and (c) the population of $|g_2\rangle$. (d) shows the total time (in soliton units) spent in the second ground state, $|g_2\rangle$ during the splitting on the barrier. In (a)–(d), we set $\Omega = 10^4$ and $g = 1$. In (e) we show the transmission in simulations of the three-component 1DGPE with different values of g as defined in Eqs. (4.16) ranging from -40 to 40 where we set $\Omega = 10^6$. Note that $g = 1$ denotes the ideal situation where all of the scattering lengths are equal and negative. We use the velocity which splits the soliton into two equally sized fragments, as found numerically from the one-component GPE for various values of w. As w decreases, the value of g has a diminished effect on the value of the transmission as the soliton spends less time in these states. The solid lines show the results of one-component simulations with the barrier V_h.

4.7 Interferometry

4.7.1 Analytical approach

Regarding the use of the barrier in an interferometry experiment, various configurations are possible. One could impose an axial harmonic trap to ensure that the two equally sized solitons recombine on the barrier in a phase-

dependent process or, alternatively, one could run the experiment in a ring trap so that the solitons will pass one another and then subsequently recombine on the barrier (another possibility is to have a second antipodal barrier for the recombination). We consider the case of a ring trap for various reasons. Namely, the simpler theoretical description due to the absence of an external trapping potential (in the propagation direction) as well as the compromise between offset from the centre and the trapping frequency to accelerate the soliton from zero to the impact velocity. Consideration would need to be given to the trap anisotropy in this case [44] as the velocity at the barrier is equal to $\omega_x x_0$ and so can be increased using either a larger offset or a larger axial trapping frequency. We expect the final transmitted population to be given by the equation

$$T(\theta) = \frac{1}{2} + \frac{A}{2}\sin(\theta - \varepsilon), \tag{4.41}$$

where A represents an amplitude of the second transmission curve or the "fringe visibility"or contrast and ε denotes the phase accumulated by the passing of the barrier (as well as the mutual soliton crossing). For a δ-function barrier with high velocities, $A = 1$ and $\varepsilon = \pi/2$. We demonstrate the achievement of this with the Λ configuration in this section by considering the extension of the soliton motion past the initial splitting to after the recombination on the barrier with different values of imparted phase difference.

Eq. (4.41) fits the second transmission curve to a sinusoid. This assumes the high velocity and narrow barrier (low w here) linear limit. Where this is not satisfied, we expect a skew in the curve due to nonlinear effects. These arise due to the soliton-soliton interactions during their mutual crossing as well as the recombination on the barrier. In order to parameterise the degree of skew in the function, we can employ the (generalized) Clausen functions, which are given by,

$$S_z(\theta) = \sum_{k=1}^{\infty} \frac{\sin(k\theta)}{k^z}, \tag{4.42}$$

For Eq. (4.42), a sawtooth function is obtained for $z = 1$ and the sine function for $z \to \infty$. We can then rewrite the fit for the expected final population as,

$$T(\theta) = \frac{1}{2} + \frac{A}{2} S_z(\theta - \varepsilon). \tag{4.43}$$

For the purpose of convergence in the fitting as well as having bounded limits,

we fit and present the results as z^{-1} where a lower z^{-1} represents a less skewed function.

4.7.2 Finding the values of A and ε

An important question is: what effect does the barrier have on the relationship between the phase difference and the transmission after recombination? It is known that, for a δ-function barrier as well as high impact velocities, the soliton acquires a $\pi/2$ phase shift upon passing the barrier. In order to show the effect of having a barrier with finite width instead of a δ-function, we define the quantities A, ε & z through Eq. (4.43) relating the transmission, T, after recombination to the phase imparted, θ, on the transmitted daughter soliton.

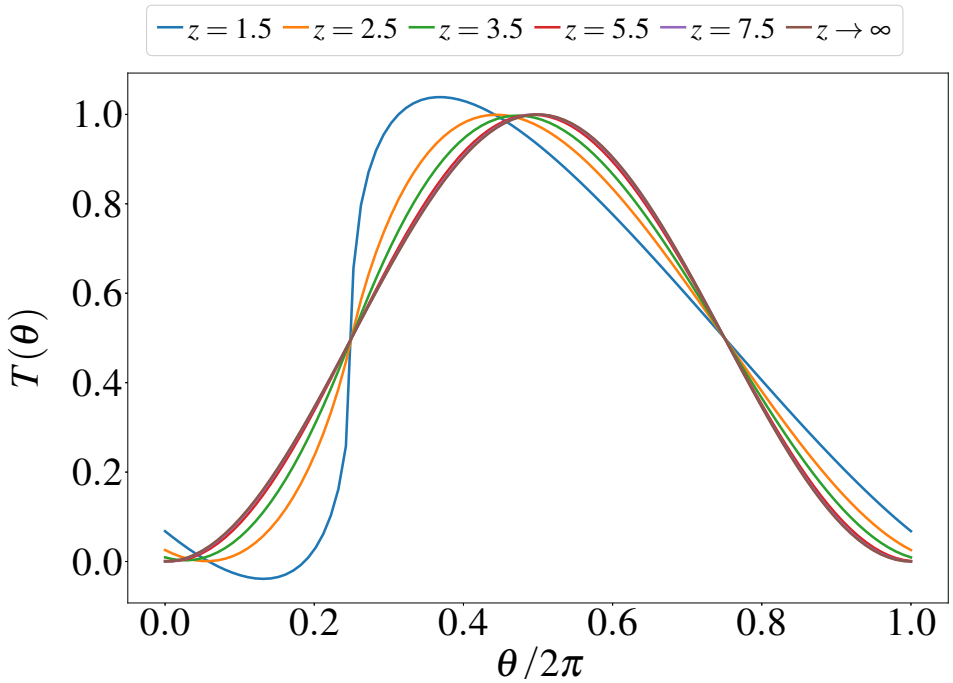

Figure 4.12: The plots shows the curve given by Eq. (4.43) for different values of z as well as the sine curve, which corresponds to $z \to \infty$.

For higher values of the parameter w, corresponding to both wider barriers and smaller splitting velocities, we expect the nonlinear effects to result in a skewed sine function for the second (phase-dependent) transmission. We parameterise the skew using the (generalised) Clausen functions, Eq. (4.42), where a higher z represents a less skewed function. Figure 4.12 shows the

curves Eq.(4.43) for increasing values of z. It can be seen that as z approaches a value of 8, it is difficult to distinguish between the skewed $T(\theta)$ fitting and the sine $T(\theta)$ fitting.

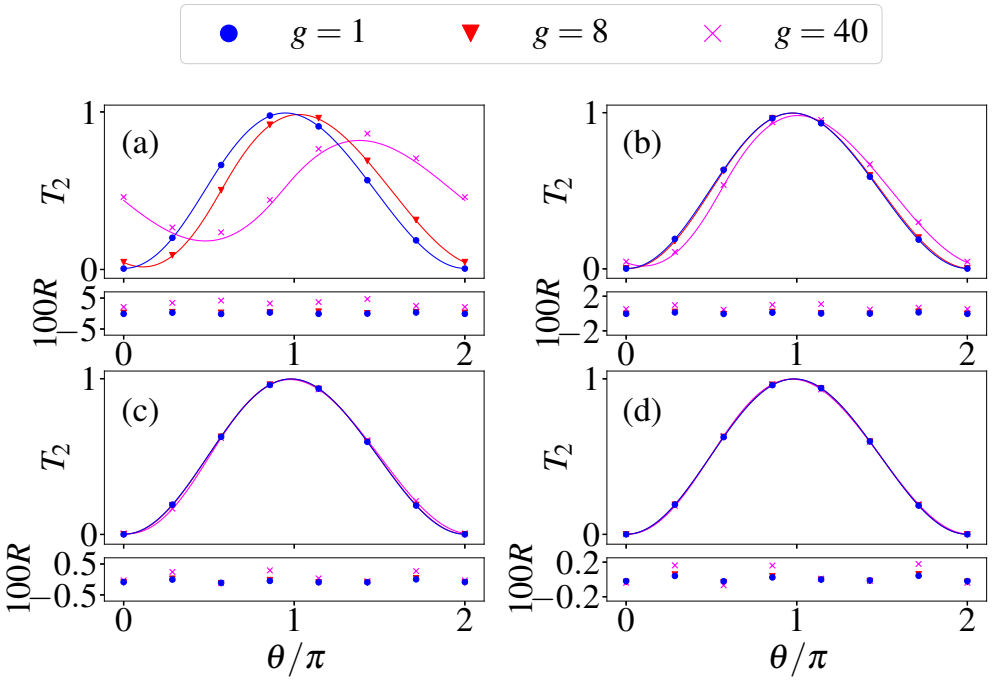

Figure 4.13: The figure shows the data points taken for T_2 for different values of the imparted phase θ for the values of g of 1, 8 and 40 and for Ω_1/Ω_0 taking values of 10, 20, 30 and 40 in (a), (b), (c) and (d), respectively. The curves show Eq. (4.43) with the best fit parameters for z^{-1}, A and ε.

Figure 4.13 shows the data taken to extract the values z^{-1}, A & ε required to produce Fig. 4.15 (for the lowest four values of Ω_1/Ω_0 of 10, 20, 30 & 40) as well as the resulting fit for Eq. (4.43). Equation (4.43) does not give a good fit for $g = 40$ in (a). This is because the fit only allows for a curve which is centred at $T = 1/2$ on the y axis. In this case, the points are consistently above the best-fit curve given by Eq. (4.43) which explains the large error bars in Fig. 4.15.

ε and A (as well as z^{-1} for the Clausen function fittings) were extracted from the simulated values of T_2 for different θ using the *curve_fit* procedure from *scipy* [133] which uses the Trust Region Reflective algorithm to find the least squares fitting. Due to the necessary compromise between the running time and the resulting precision in the determined parameter values, for Fig. 4.14

which shows the single component interferometry curve data, the number of different values of imparted phase is 32 whereas for Fig. 4.15 the number of imparted phases is 8 (20 for the corresponding single component data due to the average value of w being smaller owing to the conversion to Ω_1/Ω_0). The errors in ε and A are then obtained from the covariance (error) matrix (as the square roots of the diagonals).

4.7.3 Numerical results

In order to understand the effect of the barrier shape on the interferometer system we consider for different values of w a ring trap configuration with the barriers V_h, V_{RM}, V_δ and $V_{\mathrm{G}}(\sigma = 0.2)$ in the single component GPE. Here, V_h denotes the barrier shape produced by the narrow barrier system, V_{RM} the sech^2 barrier of comparable height and area (for which one can find the transmission properties in the high velocity limit), V_δ the δ-function with equal area to V_h (the ideal case) and $V_{\mathrm{G}}(\sigma = 0.2)$ (a narrow Gaussian barrier with a fixed width and an area the same as V_h), which takes the form,

$$V_{\mathrm{G}}(x;\sigma) = \left(\frac{\pi}{4w}\right)\left(\frac{1}{\sqrt{2\pi}\sigma}\right)\exp\left(-\frac{x^2}{2\sigma^2}\right). \tag{4.44}$$

Figure 4.14 shows the values of A and ε as well as z^{-1} extracted by means of fitting Eq. (4.43) to numerical simulations at the equal splitting velocity for a given w with varying θ. For a given value of the parameter, w, the velocity which splits the soliton into two equally sized daughter solitons is found numerically and is quoted as $\alpha = 4vw/\pi$ (the ratio between the velocity and the barrier area), which should be equal to one, in the linear limit, for a δ-function. The relationship between $\alpha_{1/2}$ and w is shown in Fig. 4.6.

In Fig. 4.14 (a) one can see the decreased presence of skew in the curve (the second transmission points increase faster than the sine curve on the left of the maximum and decrease slower than the sine curve on the right with changing θ) between the higher and lower values of w with the V_h barrier. This is an effect caused by the nonlinearity which should disappear at high velocities. We further demonstrate the decreased presence of a skew in the interferometry curve through the decreasing values of z^{-1} in (b) for the different types of barrier. We note that the Gaussian barrier with a fixed width performs better as an

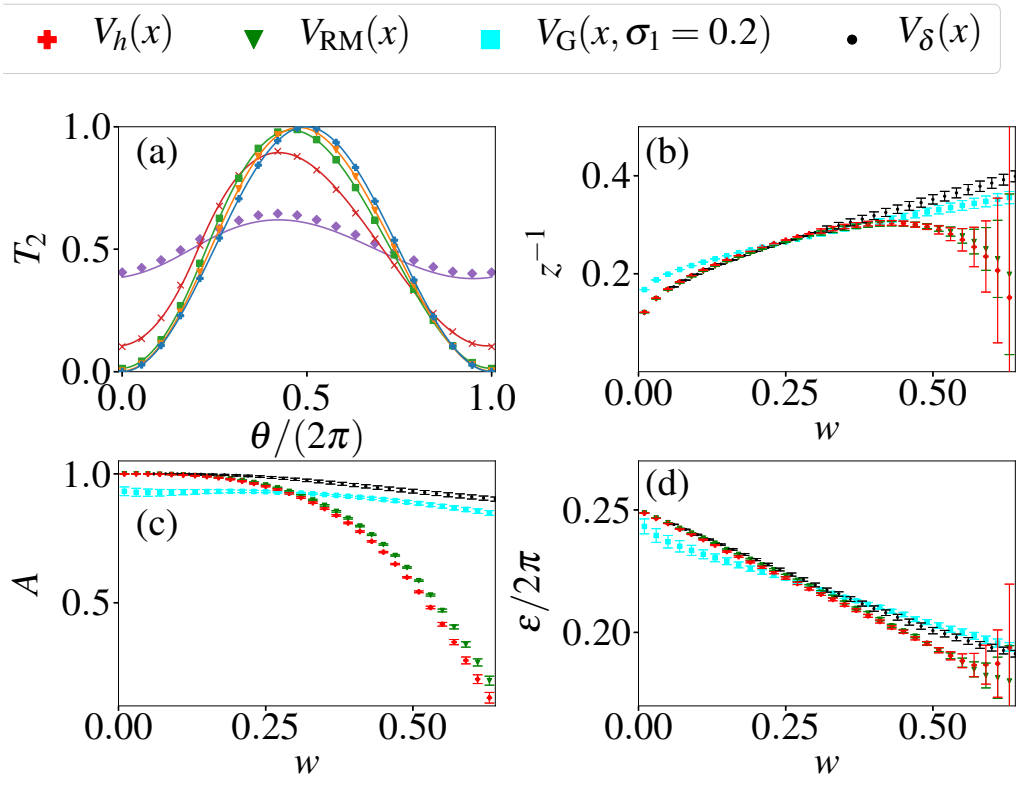

Figure 4.14: The figure shows data taken from single component simulations of the interferometry process. (a) shows the value of T_2 against the added phase for the values of $w = 0.01$ (blue plus), $w = 0.1$ (orange triangle), $w = 0.2$ (green cross), $w = 0.4$ (red square), $w = 0.6$ (purple diamond) with the barrier V_h. (b)–(d) show the values of z^{-1}, A and ε found by fitting Eq. (4.41), respectively, for the four barrier shapes V_h, V_{RM}, V_δ and $V_{\mathrm{G}}(\sigma = 0.2)$ with different values of w.

interferometer at $w \gtrsim 0.3$ and that for all of the barriers, decreasing w corresponds to increasing the velocity at which the solitons are split into two equal smaller solitons by the barrier. It is known that as the velocity is increased, narrower barriers are required to remain in the tunnelling limit rather than the velocity filtering limit. Although the scheme imposes a correlation between the equal splitting velocity and the barrier width, it should allow the barrier to bypass width limitations arising from its typical formation by an off-resonant light sheet [80]. This will allow faster soliton collisions and narrower barriers and thus improved soliton interferometry.

Figure 4.15 shows the parameters A and ε extracted from soliton interferometry simulations for the geometric barrier system with $g = 1$, $g = 8$ and $g = 40$ for

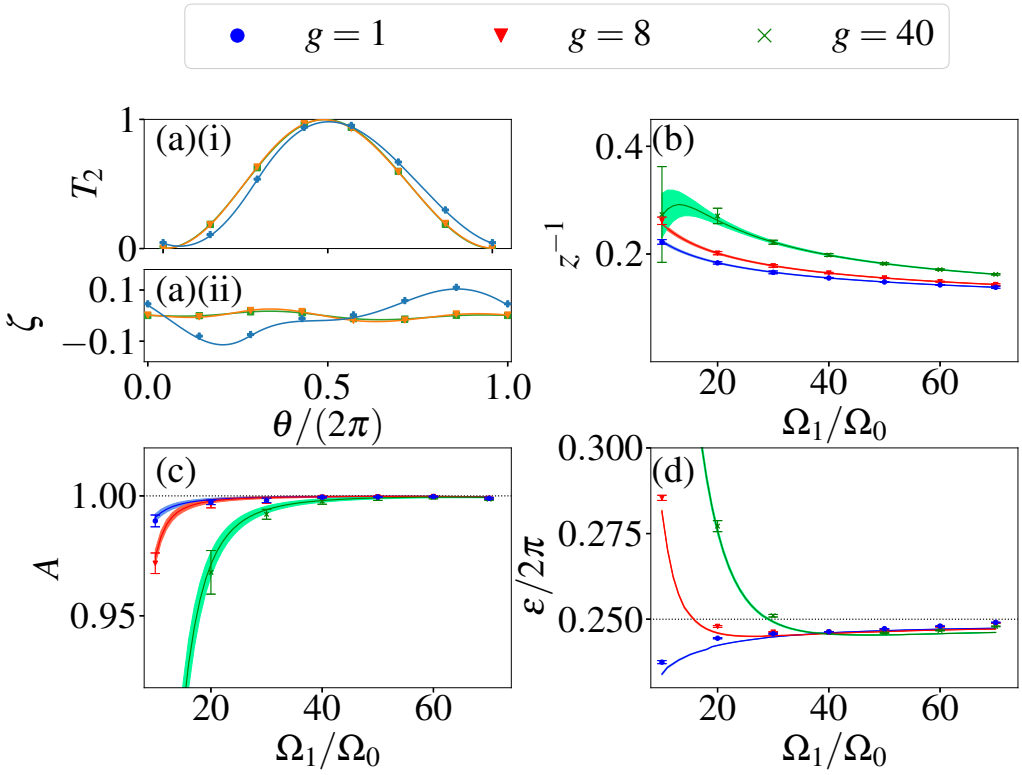

Figure 4.15: The plots show the results of simulations of the barrier system with different Ω_1/Ω_0 and g. $\Omega = 10^4$ for $\Omega_1/\Omega_0 =$ 10, 20 & 30 and $\Omega = 5\times10^4$ for $\Omega_1/\Omega_0 =$ 40, 50, 60 & 70 (related to Ω_0 and l through Eq. (4.12)) because of conflicting limitations imposed by population escape from the dark state and computational time. (a)(i) shows T_2 against θ for $\Omega_1/\Omega_0 = 20$ (blue plus), $\Omega_1/\Omega_0 = 40$ (orange triangle), $\Omega_1/\Omega_0 = 60$ (green cross); with $g = 40$. (a)(ii) shows the value of ζ against θ, where $\zeta = T_2(\theta) - 1/2(1+\sin(\theta-\pi/2))$ is the difference between the measured transmissions and the idealised sine curve. (b)–(d) show the values of z^{-1}, A and ε found by fitting Eq. (4.43), for the barrier scheme with the ideal value of $g = 1$ and also $g = 8$ and $g = 40$. The shaded areas show the error bar limits taken from single component simulations with the barrier V_h as well as the nonlinear barrier for $g \neq 1$ of Eq. (4.61).

different values of Ω_1/Ω_0. For Fig. 4.14, in order to obtain the values of α for a given value of w where the soliton is split into equal daughter solitons, we employed a root-finding procedure. For the simulations of the scheme consisting of the three components in the shown configuration, the time taken to find α directly in the three-component configuration is much longer than the single component and also the value should be the same in the desirable regions. Therefore the value of α used is the same as is found for the single component system for the V_h barrier with w and Ω_1/Ω_0 related through Eq. (4.11).

m	$1.411\,46 \times 10^{-25}\,\mathrm{kg}$
N	2500
ω_r	$40 \times 2\pi\mathrm{Hz}$

Table 4.1: The table shows the values of N, a_s and m necessary to convert between physical units and the dimensionless soliton units for the case of ^{85}Rb within the range of soliton stability. The values shown are taken from [80].

For the simulations required to produce Fig.4.15, this value of α is not changed for $g \neq 1$ which contributes to the decrease in A and ε as the transmission is affected by the change in scattering length. We show in Fig. 4.15 that this effect is diminished at high Ω_1/Ω_0.

4.8 Experimental considerations

4.8.1 Experimental values

As an example, the species ^{85}Rb with $|g_1\rangle$ the $|2,-2\rangle$ hyperfine ground state was taken. There is a wide Feshbach resonance centred at $B_0 = 156\,\mathrm{G}$ with a width of $\Delta = 10.5\,\mathrm{G}$. The wide width facilitates accurate control of the intra-species (a_{11}) scattering length. The scattering length is controlled by variation of the strength of the magnetic field, B, as Eq. (2.45) with $a_{\mathrm{bg}} = -441\,a_0$. The relevant quantities are provided in Table 4.1. Note that the value of N is not fixed but is physically constrained by factors such as the cooling mechanism used. Similarly, the value of ω_r is constrained by the need for a stable, soliton-like system. These constraints depend on the values of N, a_s and m and taken from [80]

The scattering length of the $|2,-2\rangle$ hyperfine ground state as well as the energy differences between this state and the other states in the Λ-scheme then depend on the value of the magnetic field. The values of the coupling frequencies are proportional to the energy differences between the ground states and the excited level. Let us choose the excited level as the state the ground states are coupled to by the D1 line.

We defined w in Eq. (4.11) and taking the example of ^{85}Rb, we have $m =$

1.41×10^{-25} kg. The other parameters necessary to convert between physical parameters and the units system used are N and $|g^{1D}|$. These are not fixed as m is; however, the value of $|g^{1D}|$ is controlled by the transverse trapping frequency and the magnitude of the s-wave scattering length and N is lower-bounded by the necessity to be in the many-body regime. Both $|g^{1D}|$ and N are constrained by the collapse instability [134] and the requirement for a quasi-1D soliton [44].

Taking representative values for $|g^{1D}|$ from Table 4.1 and setting $a_s = -12\,a_0$ gives 3.4×10^{-41} J m and we have the following conversions for distance and velocity:

$$\tilde{x} = x(0.94\,\mu\text{m}) \tag{4.45}$$

$$\tilde{v} = v(0.80\,\text{mm}\,\text{s}^{-1}). \tag{4.46}$$

Assuming $\alpha = 1$, for $w = 0.04$ this gives $\tilde{w} = 0.037\,\mu$m and $\tilde{v} = 16\,\text{mm}\,\text{s}^{-1}$ and for $w = 0.4$ this gives $\tilde{w} = 0.37\,\mu$m and $\tilde{v} = 1.6\,\text{mm}\,\text{s}^{-1}$. In the Λ-system, $\Omega = 10^4$ and $\Omega = 5 \times 10^4$ correspond to $\bar{\Omega} = 1.4 \times 2\pi$MHz and $\bar{\Omega} = 6.8 \times 2\pi$MHz and $l = 2\sqrt{2} = 2.7\,\mu$m is the width of the two beams.

4.8.2 Misalignment of the beams

Let us now consider some of the possible sources of error arising from the positioning of the two independent laser beams. Two simple sources of a geometrical error come from the possibility of misalignment and differences in the beam widths. In [80] the authors discuss the consequences of an un-centred barrier in a soliton interferometry system which takes place in a harmonic trap. In the results presented thus far, we have dealt with the soliton interferometry system taking place in a toroidal configuration which has the advantage of allowing for an un-centred potential barrier due to the additional circular symmetry. In this system, however, we must introduce an additional laser beam to provide the barrier and we assumed that the two beams share certain characteristics with each other. Namely, a measure of the width, l and their centres (defined as $x = 0$), as the beams are defined in Eqs. (4.9a& 4.9b). If we allow for the possibility of these properties not being fulfilled then we can re-define the profiles as

$$\Omega' = \Omega_0 \left(\frac{2}{l_0 \sqrt{\pi}} \right)^{1/2} \exp\left(- \left[\frac{x - x_0}{l_0} \right]^2 \right) \tag{4.47}$$

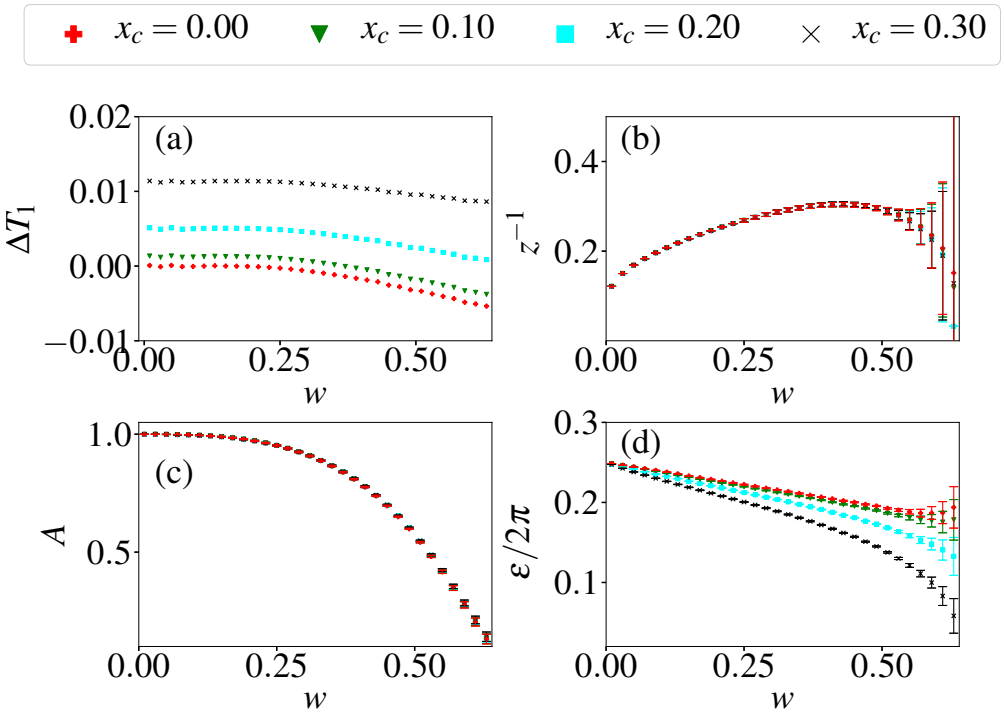

Figure 4.16: The plot shows the data obtained from fitting interferometry response curves for the splitting and subsequent recombination using the velocity-area ratio, α which gives equal splitting for the barrier V_h, with different values of w and x_c (the offset between the two barriers). (a) shows the change in T_1 relative to that obtained when the ideal values of $x_c = 0, l_1/l_0 = 1$. (b), (c) and (d) show the values of z^{-1}, A and ε, respectively.

$$\Omega_c = \Omega_1 x \left(\frac{2}{l_1 \pi^{1/6}}\right)^{3/2} \exp\left(-\left[\frac{x}{l_1}\right]^2\right) \tag{4.48}$$

We can then define h_{bad} as

$$h_{\text{bad}} = \frac{\Omega_c}{\Omega'} = \frac{2 l_0^{1/2} \Omega_1 x}{l_1^{3/2} \Omega_0} \exp\left(\frac{x_0^2}{l_0^2}\right) \exp\left(-\frac{2 x_0 x}{l_0^2}\right) \exp\left(-\delta x^2\right) \tag{4.49}$$

where $\delta \equiv l_1^{-2} - l_0^{-2}$ and we define w as

$$w = \frac{\Omega_0 l_1}{2\Omega_1}. \tag{4.50}$$

Applying Eq. (4.6) gives

$$V_{\text{bad}} = \frac{1}{2}\left(\frac{h_{\text{bad}}}{x}\right)^2 \frac{(1 - 2x_0 x/l_0^2 - 2\delta x^2)^2}{(1 + h_{\text{bad}}^2)^2}. \tag{4.51}$$

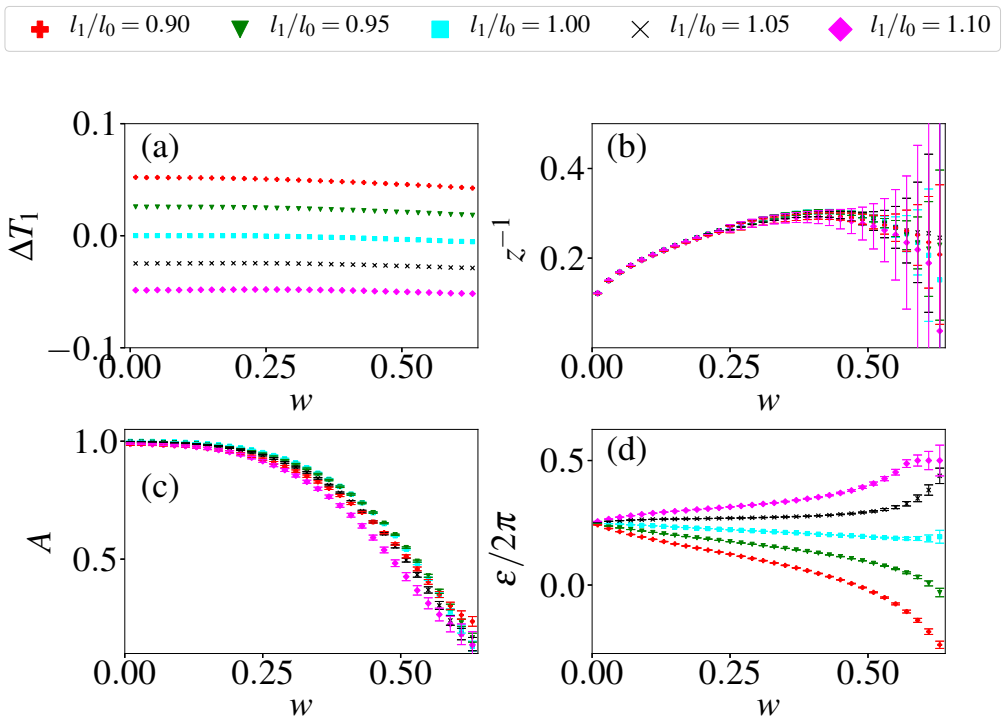

Figure 4.17: The plot shows the data obtained from fitting interferometry response curves for the splitting and subsequent recombination using the velocity-area ratio, α which gives equal splitting for the barrier V_h, with different values of w and l_1/l_0 (the width ratio between the two barriers). (a) shows the change in T_1 relative to that obtained when the ideal values of $x_c = 0$, $l_1/l_0 = 1$. (b), (c) and (d) show the values of z^{-1}, A and ε, respectively.

Note that the ideal case where $V_{\text{bad}} = V_h$ is where $x_c = 0$ and $l_1/l_0 = 1$. Using the above definition of V_{bad}, we can determine the tolerance of the interferometer to situations where $x_c \neq 0$ and $l_1/l_0 \neq 1$ and what effect these have on the system.

Figure 4.16 shows the effect on the interferometry curve of the offset between the two beams, x_c, where $x_c = 0$ corresponds to the ideal case of alignment where the resulting potential barrier splits the incoming soliton into two equally sized outgoing solitons. From Fig. 4.16(d) we can see that the greatest deviation from the ideal case is in the phase imparted by the barrier. However, in the limit where $w \to 0$ the deviation is minimised and the values of $x_c = 0, 0.1, 0.2\&0.3$ all lead to an ideal interferometry curve where $(z^{-1}, A, \varepsilon) \to (0, 1, \pi/2)$. Figure 4.17 shows the effect different widths of the two beams have on the interferometry curve parameters. Similarly to Fig. 4.16, the most signi-

ficant effect is in the phase, ε, which does converge to $\pi/2$ for all l_1/l_0 as $w \to 0$; however, it does this more slowly than for the case of $x_c \neq 0$ shown in Fig. 4.16.

4.8.3 Analysis and numerical results for $g \neq 1$

In order to find the corresponding single component system when $g \neq 1$, one can find how the nonlinearity transforms into the new basis $\{|d\rangle, |+\rangle, |-\rangle\}$ assuming $\Delta = 0$. The following expressions for the atomic basis in terms of the $\{|d\rangle, |+\rangle, |-\rangle\}$ basis will be required

$$\psi_1 = \left(h/\sqrt{1+h^2}\right)\psi_d + \left(1/\sqrt{2(1+h^2)}\right)(\psi_+ + \psi_-), \tag{4.52a}$$

$$\psi_2 = \left(-1/\sqrt{1+h^2}\right)\psi_d + \left(h/\sqrt{2(1+h^2)}\right)(\psi_+ + \psi_-), \tag{4.52b}$$

$$\psi_e = \left(1/\sqrt{2}\right)(\psi_+ - \psi_-), \tag{4.52c}$$

where $h(x)$ is defined in Eq. (4.10).

We can write the nonlinearity in the VGPE (with all scattering lengths other than g_{11} equal and denoted by g) as

$$M = U^\dagger \begin{pmatrix} A & 0 & 0 \\ 0 & B & 0 \\ 0 & 0 & B \end{pmatrix} U, \tag{4.53}$$

where $A \equiv -(|\psi_1|^2 + g|\psi_2|^2 + g|\psi_e|^2)$ and $B \equiv -g(|\psi_1|^2 + |\psi_2|^2 + |\psi_e|^2)$. We find

$$M = \begin{pmatrix} \dfrac{Ah^2+B}{1+h^2} & \dfrac{Ah/\sqrt{2}-Bh/\sqrt{2}}{1+h^2} & \dfrac{Ah/\sqrt{2}-Bh/\sqrt{2}}{1+h^2} \\ \dfrac{Ah/\sqrt{2}-Bh/\sqrt{2}}{1+h^2} & \dfrac{A/2+Bh^2/2}{1+h^2}+\dfrac{B}{2} & \dfrac{A/2+Bh^2/2}{1+h^2}-\dfrac{B}{2} \\ \dfrac{Ah/\sqrt{2}-Bh/\sqrt{2}}{1+h^2} & \dfrac{A/2+Bh^2/2}{1+h^2}-\dfrac{B}{2} & \dfrac{A/2+Bh^2/2}{1+h^2}+\dfrac{B}{2} \end{pmatrix}, \tag{4.54}$$

which is equal to $-(|\psi_1|^2 + |\psi_2|^2 + |\psi_e|^2)I_3$ if $g = 1$. Using Eqs. (4.52) we can rewrite A and B as

$$\begin{aligned} A = -\Big(&\Big|\left[h/\sqrt{1+h^2}\right]\psi_d + \left[1/\sqrt{2(1+h^2)}\right](\psi_+ + \psi_)\Big|^2 \\ &+ g\Big|\left[-1/\sqrt{1+h^2}\right]\psi_d + \left[h/\sqrt{2(1+h^2)}\right](\psi_+ + \psi_-)\Big|^2 \\ &+ g\Big|\left[1/\sqrt{2}\right](\psi_+ - \psi_-)\Big|^2\Big) \end{aligned} \tag{4.55}$$

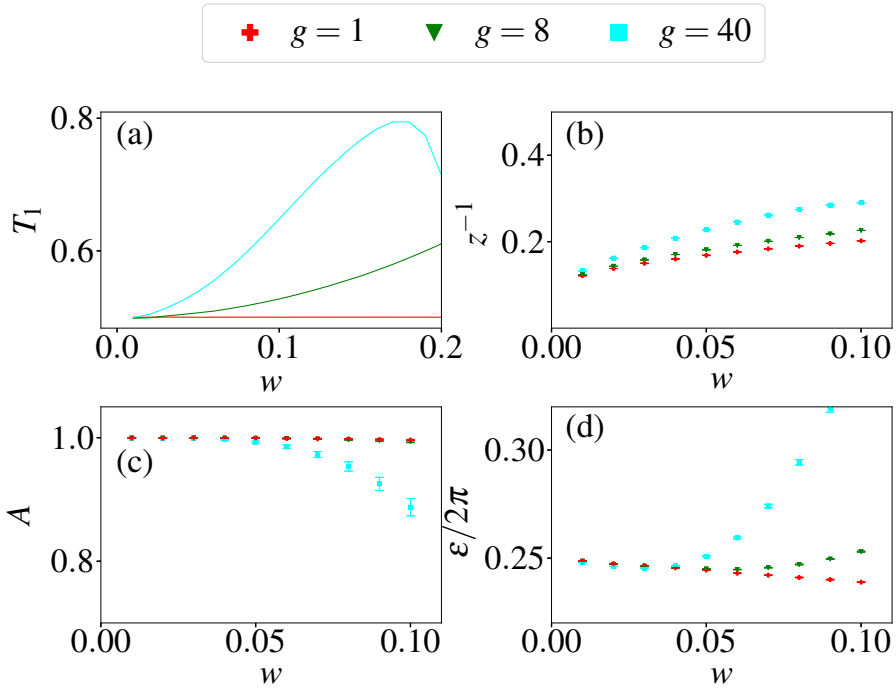

Figure 4.18: The plot shows the data obtained from fitting interferometry response curves to Eq. (4.61) with different values of w and g. (a) shows the proportion of the soliton which passes through the barrier the first time (in a ring trap configuration with a single barrier) for $g = 1$ (which is 1/2 by construction), $g = 8$ and $g = 40$. (b), (c) and (d) show the values of z^{-1}, A and ε, respectively.

$$B = -g(|\psi_d|^2 + |\psi_+|^2 + |\psi_-|^2). \tag{4.56}$$

If we assume $\psi_+ = \psi_- = 0$ then

$$A = -\left[h^2/(1+h^2) + g/(1+h^2)\right]|\psi_d|^2 \tag{4.57}$$

$$B = -g|\psi_d|^2. \tag{4.58}$$

Thus we can find M_{11} as

$$M_{11} = \left[\frac{(h^2+g)h^2}{(1+h^2)^2} + \frac{g}{1+h^2}\right](-|\psi_d|^2), \tag{4.59}$$

which can be rewritten as

$$\begin{aligned} M_{11} &= \left[\frac{h^4+2gh^2+g}{(1+h^2)^2}\right](-|\psi_d|^2) \\ &= \left[1+(g-1)\frac{2h^2+1}{(1+h^2)^2}\right](-|\psi_d|^2). \end{aligned} \tag{4.60}$$

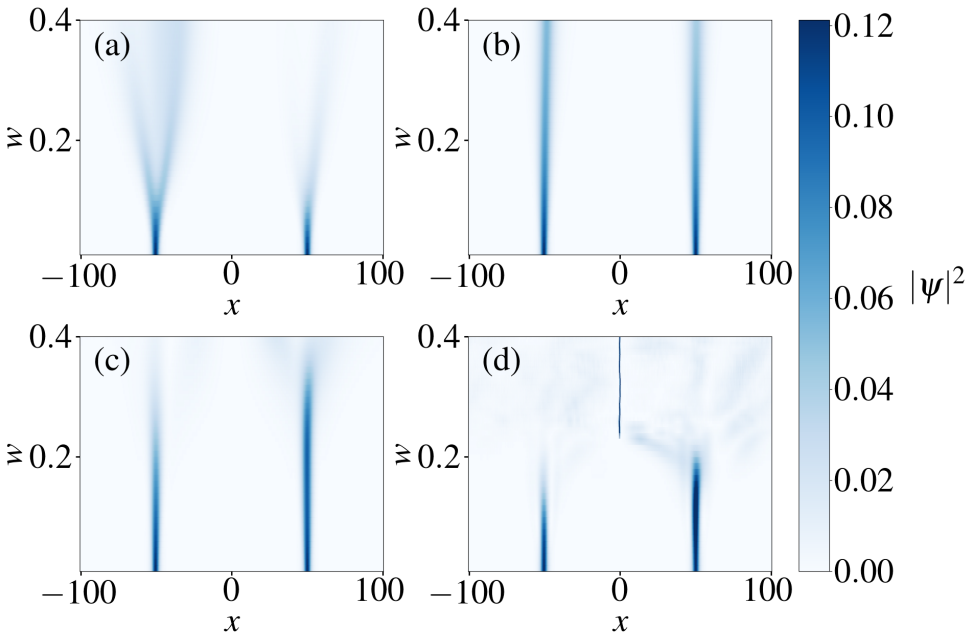

Figure 4.19: The plot shows the final density after splitting on the barrier for different w and g where the velocity is that which gives a transmission of 1/2 for $g = 1$. (a) shows the final density for $g = -40$, (b) $g = 0$, (c) $g = 8$ and (d) $g = 40$.

Therefore, we can express a single component GPE which incorporates the effect of having different scattering lengths in the system as a correctional term taking the form of a spatially dependent nonlinearity. The GPE is then

$$i\partial_t \psi_d = -(1/2)\partial_{xx}\psi_d + V_h\psi_d + \left\{-1-(g-1)\frac{2(x/w)^2+1}{[1+(x/w)^2]^2}\right\}|\psi_d|^2\psi_d. \quad (4.61)$$

Figure 4.18 shows the results of simulations with Eq. (4.61) with different values of w and g. The results are shown similar to in Fig. 4.14 but over a smaller range of w values due to the system breaking down to an extent where it becomes ill-defined to attempt to extract values of A, ε and z^{-1}. Figure 4.18(a) shows how much of the soliton is transmitted through the barrier for $g \neq 1$ where the velocity is that which results in a transmission of 1/2 when $g = 1$. For this plot the limit on the displayed values of w is relaxed as the value of T_1 is the transmission of the soliton after it is split on the barrier and does not rely on a recombination process with a phase-dependence in order to extract a response curve.

Increasing the value of w leads to the soliton being split into many fragments rather than two fragments and the value of T_1 fluctuates.

The fragmentation of the solitons on the barrier with increased g is demonstrated in Fig. 4.19 which shows the final soliton density after passing the barrier (moving in the simulations from position $x = -L/4$ to position $x = +L/4$ with $L = 64\pi$) for increasing values of w and for various values of g in the 1DGPE with the nonlinear potential term, Eq. (4.61). The values of g are: (a) $g = -40$, (b) $g = 0$, (c) $g = 8$ and (d) $g = 40$. Figure 4.19 shows the how the different values of the scattering lengths in the system effect the creation of two coherent solitons. Greater magnitudes of g clearly result in more instability in the outgoing solitons but the effect is diminished for all g as $w \to 0$. Note the trapped portion of the original soliton at $x = 0$ in (d) as a result of the strong attractive nonlinearity (positive g implies negative scattering lengths).

Chapter 5

Conclusions

5.1 Splitting of two-component solitary waves on potential barriers

The aim of this project was to address how coupled solitary waves interact with a single barrier potential and whether they can be separated into individual solitons. An analytical model was presented which assumes a low velocity limit such that the barrier can be treated perturbatively as a δ-function. For the GPE describing a binary BEC, two limiting cases were considered which can be formulated into a set of equations which describe the system in the absence of an external potential. Incorporating the barrier potential as a δ-function and finding the associated energy cost of traversing the barrier, one can devise inequalities which denote the regions where the components should be separated. The numerical study was carried out in order to, firstly, demonstrate agreement between the analytical (perturbative) model and the barrier added into the GPE. The two cases are: the limit where there is no interspecies coupling and one starts off with two uncoupled bright solitons with different populations and the limit where the one of the components has significantly more population such that the nonlinearity of the smaller component can be neglected. Then, simulations were run in the domain where the intitial density profiles used in the analysis are not known and so the perturbation theory cannot be directly applied.

The numerical study found a good agreement with the presented analysis in the

regimes where it is expected to apply (dependent on the relationship between the different parameter values such as ε and f) and beyond these boundaries, maintains a good indication of the regions where the components are partially separated. These results where then used to examine the directly nonlinear effect of varying the parameter g, which controls the interspecies coupling, and cannot be accounted for in the analysis (for the case where f and $1-f$ are comparable). As well as the soliton separation case, the study was extended to model a subsequent second interaction with the barrier, revealing complex interference behaviour. Also modelled was the alternative situation where regions in parameter space were found for which initially separated solitons can be wholly or partially combined on the barrier.

Directions for further research upon what has been presented could be to apply the same methodology to other multiple component systems; such as, considering the effects of additional components and the case where different scattering length signs enable the formation of composite solitons of mixed type (bright and dark). Another directions would be to simulate the soliton motion in the non-polynomial GPE. Note that for the case where the scattering lengths take different values, the non-polynomial GPE analogue for two components takes the form of a set of four coupled nonlinear equations. These can be simulated in order to investigate the difference between motion in the 1D binary GPE and in the non-polynomial binary GPE. The outcome of this would be to gain more understanding of the effects of 3D dynamics on the soliton motion (without simulating the fully 3D GPE).

Another interesting topic for further research would be to incorporate the system into an interferometer scheme. In order to do this, one would have to implement a protocol for conversion between the components (experimentally utilising atomic level transitions). More suited to the case where $f = 0.5$ (equal populations), the premise would be to combine the atomic transitions with the different scattering properties (meaning both low energy quantum scattering properties and the effect on the interaction with the barrier due to the different soliton properties) in order to obtain two solitons which can undergo interference effects on the potential barrier. One could investigate the parameter regimes under which this could work and the effects of the combined protocol on the coherence of the split solitons.

5.2 Splitting on narrow barriers using geometric potentials

In this investigation, the objective was to improve upon the soliton interferometry scheme using a diffraction-limited Gaussian barrier as the beam splitter by replacing it with a geometric potential beam splitter which can produce a subwavelength width barrier. This potential is formed from a non-adiabatic correction term which originates in the kinetic energy term of the Gross–Pitaevskii equation. Using two coupling beams in a Λ-system with a Gaussian and a first order Hermite–Gaussian profile, the form of the barrier obtained is the square of a Lorentzian. A potential disadvantage of this system would be the fixed relationship between the height of the barrier and its area. The advantage, however, is that the amount of tunnelling in the system is constant for increasing areas (in the narrow barrier limit, this means a higher velocity for equal transmitted and reflected outgoing solitons). The degree of tunnelling here means the ratio between the centre-of-mass kinetic energy and the barrier height (at half transmission).

The barrier was compared to various other shapes of barrier of either experimental or theoretical significance in order to improve understanding as well as knowledge of the limits in which interferometry can be enhanced. These barriers were the Gaussian barrier, as it is the closest approximation to a laser beam profile generating a repulsive barrier when blue-detuned; the δ-function barrier which represents a barrier with finite area and infinitesimal width such that the soliton can only pass via tunnelling; and a sech^2 barrier which is a finite width barrier for which an analytical treatment can be given in the high-velocity limit for its transmission.

When considering the three-component system generating the narrow barrier, it is modelled using the VGPE. The ideal system is where all of the scattering lengths are equal (and negative to support a bright soliton). The scattering lengths can be manipulated using the Feshbach resonance technique but there is limited control of the scattering lengths independently. In order to address the departure from the ideal situation, the parameter g was introduced as the ratio between the other scattering lengths and the scattering length of the initial

state in which the soliton exists. It was shown numerically that as the value of w (related to the ratio between the two laser powers) decreases, corresponding to narrower barriers and higher velocities over which the transmission increases from zero to one, the value of g has less impact on the performance of the interferometer.

The other parameter in the three level system which has no counterpart in the single component system interacting with the squared Lorentzian barrier is the value of Ω (proportional to Ω_0) which is the absolute value of the coupling of the Gaussian beam; upon which the parameter characterising the resultant barrier is found as the ratio of the Hermite–Gaussian beam power to this Gaussian beam power. This parameter needs to be significantly large so as to prevent loss into the lower energy $|-\rangle$ state during the barrier passage. A large value of Ω is ideal (at least within the constraints of the model as a large value in an experimental system could result in the breakdown of the three level approximation). The difficulty is in simulations of the system as an extremely small timestep is required to model these dynamics as well as the matrix operations required to execute the time evolution of the non-diagonal terms in the VGPE. The data presented already approached the practical limit of feasible computation duration.

Developments of the research presented could be to consider the case of non-zero detuning and spontaneous emission terms in the simulations. The simulations shown take both of these terms to have a value of zero. In order for the scheme to work as a suitable interferometer, the soliton after the splitting by the barrier has to be wholly in the original ground state of the three-level system ($|g_1\rangle$). We considered values of the coupling frequency (Ω) which fulfill this condition and note that the presence of a decay term could be mitigated with a higher value of Ω. However, simulating increasing values of Ω is constrained by computational limitations. In the ideal operational limit, the timescales of the atomic dynamics (the three-level system) and the soliton dynamics (interactions with the barrier) are disparate which makes them difficult to model in the same simulations. A valid approach could be to utilise the separation of linear and nonlinear dynamics and take the relevant single component GPE system presented in the thesis for the interaction of the soliton with the barrier (including the $g \neq 1$ case) as well as an appropriate linear vector Schrödinger equation

to model the system forming the effective barrier. These two approaches could even be combined by, for example, incorporating a loss term into the soliton dynamical equation with parameters determined using the linear barrier simulations.

Another direction for further work would be to elaborate upon the issue of practical (experimental) implementation. This was partly addressed by considering the effect of beam misalignment on the interferometer sensitivity. Note that the misalignments refers here to different sized beam waists and different beams centres. As we consider the system to inhabit a ring trap, we do not have to account for the issue of an off-centred barrier. If the barrier was off-centred in a harmonic trap, then this would be another possible origin of error. We chose not to consider this as it is also a problem in a single beam soliton-barrier experiment and is not unique to the two-beam barrier we consider here. Further thought could also be given to issues such as noise in the beams and its effect on the system as well as three-dimensional effects arising from the fact that the soliton exists as a 1D limit of a 3D system.

Appendix A

Appendix

A.1 Three level system with a non-zero detuning

The relevant equations describing the atomic system (independent of the non-linearities) can be readily generalised to incorporate a non-zero detuning from the excited state (the two-photon detuning remains zero), however, the expressions become much more involved. Crucially, the form of the resulting potential barrier stays the same. In the following analysis, $\epsilon_\pm$ and $N_\pm$ are defined as

$$\epsilon_\pm = \left(-\tilde{\Delta} \pm \sqrt{\tilde{\Delta}^2 + \bar{\Omega}^2}\right)/\bar{\Omega}, \tag{A.1}$$

$$N_\pm = (1+\epsilon_\pm^2)^{-1/2}. \tag{A.2}$$

It is useful to first note the following derivatives and identities:

$$\begin{aligned}
&\partial_x \bar{\Omega} = \frac{\Omega_\mathrm{c}}{\bar{\Omega}}(\partial_x \Omega_\mathrm{c}) \\
&\partial_x\left(\frac{\Omega_\mathrm{c}}{\bar{\Omega}}\right) = \frac{(\partial_x\Omega_\mathrm{c})}{\bar{\Omega}} - \frac{\Omega_\mathrm{c}}{\bar{\Omega}^2}(\partial_x\bar{\Omega}) = \frac{\Omega^2}{\bar{\Omega}^3}(\partial_x\Omega_\mathrm{c}) \\
&\partial_x\left(\frac{\Omega}{\bar{\Omega}}\right) = \Omega\partial_x\left(\frac{1}{\bar{\Omega}}\right) = -\frac{\Omega}{\bar{\Omega}^2}(\partial_x\bar{\Omega}) = -\frac{\Omega\Omega_\mathrm{c}}{\bar{\Omega}^3}(\partial_x\Omega_\mathrm{c}) \\
&\partial_x\epsilon_\pm = [\pm(\bar{\Omega}^2+\tilde{\Delta}^2)^{-1/2} - \bar{\Omega}^{-1}\epsilon_\pm](\partial_x\bar{\Omega}) \\
&= [\pm(\bar{\Omega}^2+\tilde{\Delta}^2)^{-1/2} - \bar{\Omega}^{-1}\epsilon_\pm]\frac{\Omega_\mathrm{c}(\partial_x\Omega_\mathrm{c})}{\bar{\Omega}} \\
&\partial_x N_\pm = -2^{-1}(1+\epsilon_\pm^2)^{-3/2}2\epsilon_\pm(\partial_x\epsilon_\pm) \\
&= -\epsilon_\pm N_\pm^3[\pm(\bar{\Omega}^2+\tilde{\Delta}^2)^{-1/2} - \bar{\Omega}^{-1}\epsilon_\pm]\frac{\Omega_\mathrm{c}(\partial_x\Omega_\mathrm{c})}{\bar{\Omega}} \\
&N_+^2 + N_-^2 = 1
\end{aligned}$$

$$\epsilon_+^2 N_+^2 + \epsilon_-^2 N_-^2 = 1$$
$$\epsilon_+ N_+^2 + \epsilon_- N_-^2 = 0$$
$$-\epsilon_+\epsilon_- = 1.$$

The unitary matrix, U, is given by

$$U = \begin{pmatrix} -\frac{\Omega}{\bar{\Omega}} & \frac{N_+\Omega_c}{\bar{\Omega}} & \frac{N_-\Omega_c}{\bar{\Omega}} \\ \frac{\Omega_c}{\bar{\Omega}} & \frac{N_+\Omega}{\bar{\Omega}} & \frac{N_-\Omega}{\bar{\Omega}} \\ 0 & N_+\epsilon_+ & N_-\epsilon_- \end{pmatrix}.$$

Therefore, $\partial_x U$ is given by

$$\partial_x U = \begin{pmatrix} \frac{\Omega\Omega_c}{\bar{\Omega}^3}(\partial_x\Omega_c) & \frac{N_+\Omega^2}{\bar{\Omega}^3}(\partial_x\Omega_c) + \frac{\Omega_c}{\bar{\Omega}}(\partial_x N_+) & \frac{N_-\Omega^2}{\bar{\Omega}^3}(\partial_x\Omega_c) + \frac{\Omega_c}{\bar{\Omega}}(\partial_x N_-) \\ \frac{\Omega^2}{\bar{\Omega}^3}(\partial_x\Omega_c) & -\frac{N_+\Omega\Omega_c}{\bar{\Omega}^3}(\partial_x\Omega_c) + \frac{\Omega}{\bar{\Omega}}(\partial_x N_+) & -\frac{N_-\Omega\Omega_c}{\bar{\Omega}^3}(\partial_x\Omega_c) + \frac{\Omega}{\bar{\Omega}}(\partial_x N_-) \\ 0 & (\partial_x N_+)\epsilon_+ + N_+(\partial_x\epsilon_+) & (\partial_x N_-)\epsilon_- + N_-(\partial_x\epsilon_-) \end{pmatrix}$$

$$= \frac{(\partial_x\Omega_c)}{\bar{\Omega}} \begin{pmatrix} \frac{\Omega\Omega_c}{\bar{\Omega}^2} & \frac{N_+}{\bar{\Omega}} - \frac{N_+^3\Omega_c^2}{\bar{\Omega}^3} - \frac{\epsilon_+ N_+^3\Omega_c^2}{\bar{\Omega}^2}(\bar{\Omega}^2+\Delta^2)^{-1/2} & \frac{N_-}{\bar{\Omega}} - \frac{N_-^3\Omega_c^2}{\bar{\Omega}^3} + \frac{\epsilon_- N_-^3\Omega_c^2}{\bar{\Omega}^2}(\bar{\Omega}^2+\Delta^2)^{-1/2} \\ \frac{\Omega^2}{\bar{\Omega}^2} & -\frac{N_+^3\Omega\Omega_c}{\bar{\Omega}^3} - \frac{\epsilon_+ N_+^3\Omega\Omega_c}{\bar{\Omega}^2}(\bar{\Omega}^2+\Delta^2)^{-1/2} & -\frac{N_-^3\Omega\Omega_c}{\bar{\Omega}^3} + \frac{\epsilon_- N_-^3\Omega\Omega_c}{\bar{\Omega}^2}(\bar{\Omega}^2+\Delta^2)^{-1/2} \\ 0 & -\frac{N_+^3\Omega_c}{\bar{\Omega}}\left[(\bar{\Omega}^2+\Delta^2)^{-1/2} - \frac{\epsilon_+}{\bar{\Omega}}\right] & \frac{N_-^3\Omega_c}{\bar{\Omega}}\left[(\bar{\Omega}^2+\Delta^2)^{-1/2} + \frac{\epsilon_-}{\bar{\Omega}}\right] \end{pmatrix}.$$

Then, one can find an expression for $A = iU^\dagger(\partial_x U)$

$$A = \frac{i(\partial_x\Omega_c)}{\bar{\Omega}} \begin{pmatrix} -\frac{\Omega}{\bar{\Omega}} & \frac{\Omega_c}{\bar{\Omega}} & 0 \\ \frac{\Omega_c}{\sqrt{2}\bar{\Omega}} & \frac{\Omega}{\sqrt{2}\bar{\Omega}} & \frac{1}{\sqrt{2}} \\ \frac{\Omega_c}{\sqrt{2}\bar{\Omega}} & \frac{\Omega}{\sqrt{2}\bar{\Omega}} & -\frac{1}{\sqrt{2}} \end{pmatrix} \bullet$$
$$\begin{pmatrix} \frac{\Omega\Omega_c}{\bar{\Omega}^2} & \frac{N_+}{\bar{\Omega}} - \frac{N_+^3\Omega_c^2}{\bar{\Omega}^3} - \frac{\epsilon_+ N_+^3\Omega_c^2}{\bar{\Omega}^2}(\bar{\Omega}^2+\Delta^2)^{-1/2} & \frac{N_-}{\bar{\Omega}} - \frac{N_-^3\Omega_c^2}{\bar{\Omega}^3} + \frac{\epsilon_- N_-^3\Omega_c^2}{\bar{\Omega}^2}(\bar{\Omega}^2+\Delta^2)^{-1/2} \\ \frac{\Omega^2}{\bar{\Omega}^2} & -\frac{N_+^3\Omega\Omega_c}{\bar{\Omega}^3} - \frac{\epsilon_+ N_+^3\Omega\Omega_c}{\bar{\Omega}^2}(\bar{\Omega}^2+\Delta^2)^{-1/2} & -\frac{N_-^3\Omega\Omega_c}{\bar{\Omega}^3} + \frac{\epsilon_- N_-^3\Omega\Omega_c}{\bar{\Omega}^2}(\bar{\Omega}^2+\Delta^2)^{-1/2} \\ 0 & -\frac{N_+^3\Omega_c}{\bar{\Omega}}\left[(\bar{\Omega}^2+\Delta^2)^{-1/2} - \frac{\epsilon_+}{\bar{\Omega}}\right] & \frac{N_-^3\Omega_c}{\bar{\Omega}}\left[(\bar{\Omega}^2+\Delta^2)^{-1/2} + \frac{\epsilon_-}{\bar{\Omega}}\right] \end{pmatrix}$$
$$= \frac{i\Omega(\partial_x\Omega_c)}{\bar{\Omega}^2} \begin{pmatrix} 0 & \frac{1}{\sqrt{2}}\sqrt{\frac{\bar{\Omega}\epsilon_+}{\sqrt{\bar{\Omega}^2+\Delta^2}}} & \frac{1}{\sqrt{2}}\sqrt{\frac{-\bar{\Omega}\epsilon_-}{\sqrt{\bar{\Omega}^2+\Delta^2}}} \\ -\frac{1}{\sqrt{2}}\sqrt{\frac{\bar{\Omega}\epsilon_+}{\sqrt{\bar{\Omega}^2+\Delta^2}}} & 0 & \frac{\Delta\Omega_c\bar{\Omega}}{2(\bar{\Omega}^2+\Delta^2)\Omega} \\ -\frac{1}{\sqrt{2}}\sqrt{\frac{-\bar{\Omega}\epsilon_-}{\sqrt{\bar{\Omega}^2+\Delta^2}}} & -\frac{\Delta\Omega_c\bar{\Omega}}{2(\bar{\Omega}^2+\Delta^2)\Omega} & 0 \end{pmatrix}$$

$$= \frac{i\Omega(\partial_x \Omega_c)}{\bar{\Omega}^2} \begin{pmatrix} 0 & N_+ & N_- \\ -N_+ & 0 & C \\ -N_- & -C & 0 \end{pmatrix},$$

where

$$C = \frac{\Delta \Omega_c \bar{\Omega}}{2(\bar{\Omega}^2 + \Delta^2)\Omega},$$

and

$$N_\pm = \frac{1}{\sqrt{2}} \sqrt{\frac{\pm \bar{\Omega} \epsilon_\pm}{\sqrt{\bar{\Omega}^2 + \Delta^2}}}.$$

The potential barrier is given by the $A^2/2$ term acting on the dark state. $A^2/2$ takes the form

$$\frac{A^2}{2} = \frac{1}{2}\left(\frac{\Omega \partial_x \Omega_c}{\bar{\Omega}^2}\right)^2 \begin{pmatrix} 1 & -CN_- & CN_+ \\ -CN_- & N_+^2 + C^2 & N_+ N_- \\ CN_+ & N_+ N_- & N_-^2 + C^2 \end{pmatrix}. \tag{A.3}$$

Bibliography

[1] L. Morel, Z. Yao, P. Cladé, and S. Guellati-Khélifa, Nature **588** (2020).

[2] A. Shayeghi, P. Rieser, G. Richter, U. Sezer, J. H. Rodewald, P. Geyer, T. J. Martinez, and M. Arndt, Nat. Commun. **11** (2020).

[3] A. Griesmaier, J. Stuhler, T. Koch, M. Fattori, T. Pfau, and S. Giovanazzi, Phys. Rev. Lett. **97**, 250402 (2006).

[4] A. Griesmaier, J. Werner, S. Hensler, J. Stuhler, and T. Pfau, Phys. Rev. Lett. **94**, 160401 (2005).

[5] M. Lu, N. Q. Burdick, S. H. Youn, and B. L. Lev, Phys. Rev. Lett. **107**, 190401 (2011).

[6] J. Sabbatini, W. H. Zurek, and M. J. Davis, Phys. Rev. Lett. **107**, 230402 (2011).

[7] B. Sundar, M. Thibodeau, Z. Wang, B. Gadway, and K. R. A. Hazzard, Phys. Rev. A **99**, 013624 (2019).

[8] J. A. Blackmore, R. Sawant, P. D. Gregory, S. L. Bromley, J. Aldegunde, J. M. Hutson, and S. L. Cornish, Phys. Rev. A **102**, 053316 (2020).

[9] A. Koetsier, D. B. M. Dickerscheid, and H. T. C. Stoof, Phys. Rev. A **74**, 033621 (2006).

[10] S. Zhang and A. J. Leggett, Phys. Rev. A **79**, 023601 (2009).

[11] S. N. Bose, Z. Phys. **26**, 178 (1924).

[12] A. Einstein, Sitzungsber. K. Preuss. Akad. Wiss. Phys. Math. Kl. , 261 (1924).

[13] A. Einstein, Sitzungsber. K. Preuss. Akad. Wiss. Phys. Math. Kl. , 3 (1925).

[14] A. Einstein, Sitzungsber. K. Preuss. Akad. Wiss. Phys. Math. Kl. , 18 (1925).

[15] L. Tisza, Phys. Rev. **72**, 838 (1947).

[16] N. N. Bogolyubov, J. Phys. U.S.S.R. **11**, 23 (1947).

[17] O. Penrose and L. Onsager, Phys. Rev. **104**, 576 (1956).

[18] D. M. Eagles, Phys. Rev. **186**, 456 (1969).

[19] E. Rutherford, The London, Edinburgh, and Dublin Philosophical Magazine and Journal of Science **21**, 669 (1911).

[20] H. G. J. Moseley, The London, Edinburgh, and Dublin Philosophical Magazine and Journal of Science **27**, 703 (1914).

[21] H. Deng, G. Weihs, C. Santori, J. Bloch, and Y. Yamamoto, Science **298**, 199 (2002).

[22] D. Snoke, Science **298**, 1368 (2002).

[23] J. Kasprzak, D. D. Solnyshkov, R. André, L. S. Dang, and G. Malpuech, Phys. Rev. Lett. **101**, 146404 (2008).

[24] J. Klaers, J. Schmitt, F. Vewinger, and M. Weitz, Nature **468**, 545 (2010).

[25] M. Randeria, Nat. Phys. **6**, 561 (2010).

[26] T. Nikuni, M. Oshikawa, A. Oosawa, and H. Tanaka, Phys. Rev. Lett. **84**, 5868 (2000).

[27] E. Inonu and E. P. Wigner, Proceedings of the National Academy of Sciences **39**, 510 (1953).

[28] F. Wilczek, Phys. Rev. Lett. **49**, 957 (1982).

[29] D.-H. Lee and M. P. A. Fisher, Phys. Rev. Lett. **63**, 903 (1989).

[30] L. Chomaz, D. Petter, P. Ilzhöfer, G. Natale, A. Trautmann, C. Politi, G. Durastante, R. M. W. van Bijnen, A. Patscheider, M. Sohmen, M. J. Mark, and F. Ferlaino, Phys. Rev. X **9**, 021012 (2019).

[31] L. Tanzi, E. Lucioni, F. Famà, J. Catani, A. Fioretti, C. Gabbanini, R. N. Bisset, L. Santos, and G. Modugno, Phys. Rev. Lett. **122**, 130405 (2019).

[32] H. T. C. Stoof, K. B. Gubbels, and D. B. M. Dickersheid, *Ultracold Quantum Fields* (Springer, 2009).

[33] D. G. Fried, T. C. Killian, L. Willmann, D. Landhuis, S. C. Moss, D. Kleppner, and T. J. Greytak, Phys. Rev. Lett. **81**, 3811 (1998).

[34] M. H. Anderson, J. R. Ensher, M. R. Matthews, C. E. Wieman, and E. A. Cornell, Science **269**, 198 (1995), https://science.sciencemag.org/content/269/5221/198.full.pdf .

[35] K. B. Davis, M. O. Mewes, M. R. Andrews, N. J. van Druten, D. S. Durfee, D. M. Kurn, and W. Ketterle, Phys. Rev. Lett. **75**, 3969 (1995).

[36] C. C. Bradley, C. A. Sackett, J. J. Tollett, and R. G. Hulet, Phys. Rev. Lett. **75**, 1687 (1995).

[37] C. J. Myatt, E. A. Burt, R. W. Ghrist, E. A. Cornell, and C. E. Wieman, Phys. Rev. Lett. **78**, 586 (1997).

[38] T. Hänsch and A. Schawlow, Optics Communications **13**, 68 (1975).

[39] J. Söding, D. Guéry-Odelin, P. Desbiolles, G. Ferrari, and J. Dalibard, Phys. Rev. Lett. **80**, 1869 (1998).

[40] M. D. Barrett, J. A. Sauer, and M. S. Chapman, Phys. Rev. Lett. **87**, 010404 (2001).

[41] T. Weber, J. Herbig, M. Mark, H. C. Nägerl, and R. Grimm, Science **299**, 232 (2003).

[42] N. Friedman, A. Kaplan, and N. Davidson, Adv. At. Mol. Opt. Phys. **48**, 99 (2002).

[43] H. Moritz, T. Stöferle, K. Günter, M. Köhl, and T. Esslinger, Phys. Rev. Lett. **94**, 210401 (2005).

[44] T. P. Billam, S. A. Wrathmall, and S. A. Gardiner, Phys. Rev. A **85**, 013627 (2012).

[45] Y. Kawaguchi and M. Ueda, Physics Reports **520**, 253 (2012).

[46] L. Allen and H. Eberly, J, *Optical Resonance and Two-Level Atoms* (Dover, 1987).

[47] P. S. Julienne, F. H. Mies, E. Tiesinga, and C. J. Williams, Phys. Rev. Lett. **78**, 1880 (1997).

[48] J. P. Burke, J. L. Bohn, B. D. Esry, and C. H. Greene, Phys. Rev. A **55**, R2511 (1997).

[49] H. E. Nistazakis, Z. Rapti, D. J. Frantzeskakis, P. G. Kevrekidis, P. Sodano, and A. Trombettoni, Phys. Rev. A **78**, 023635 (2008).

[50] S. Manakov, Zh. Eksp. Teor. Fiz. **65**, 505 (1973).

[51] B. A. Malomed and R. S. Tasgal, Phys. Rev. E **58**, 2564 (1998).

[52] L. C. Zhao, Phys. Rev. E **97**, 062201 (2018).

[53] D. Luo, Y. Jin, J. H. V. Nguyen, B. A. Malomed, O. V. Marchukov, V. A. Yurovsky, V. Dunjko, M. Olshanii, and R. G. Hulet, Phys. Rev. Lett. **125**, 183902 (2020).

[54] T. M. Bersano, V. Gokhroo, M. A. Khamehchi, J. D'Ambroise, D. J. Frantzeskakis, P. Engels, and P. G. Kevrekidis, Phys. Rev. Lett. **120**, 063202 (2018).

[55] L. Salasnich, A. Parola, and L. Reatto, Phys. Rev. A **65**, 043614 (2002).

[56] J. Cuevas, P. G. Kevrekedis, B. A. Malomed, P. Dyke, and R. G. Hulet, New J. Phys. **15**, 063006 (2013).

[57] L. Salasnich and B. A. Malomed, Phys. Rev. A **74**, 053610 (2006).

[58] S. Giovanazzi, A. Görlitz, and T. Pfau, Phys. Rev. Lett. **89**, 130401 (2002).

[59] H. T. C. Stoof and M. J. Bijlsma, J. Low Temp. Phys. **124**, 431 (2001).

[60] N. P. Proukakis, N. G. Parker, C. F. Barenghi, and C. S. Adams, Phys. Rev. Lett. **93**, 130408 (2004).

[61] S. Choi, S. A. Morgan, and K. Burnett, Phys. Rev. A **57**, 4057 (1998).

[62] M. Ueda, *Fundamentals and New Frontiers in Bose–Einstein condensates* (World Scientific Publishing, 2010).

[63] N. Manikandan, R. Radhakrishnan, and K. Aravinthan, Phys. Rev. E **90**, 022902 (2014).

[64] P. Pedri and L. Santos, Phys. Rev. Lett. **95**, 200404 (2005).

[65] D. Mihalache, D. Mazilu, F. Lederer, B. A. Malomed, L.-C. Crasovan, Y. V. Kartashov, and L. Torner, Phys. Rev. A **72**, 021601 (2005).

[66] H. Saito and M. Ueda, Phys. Rev. Lett. **90**, 040403 (2003).

[67] L. D. Carr and Y. Castin, Phys. Rev. A **66**, 063602 (2002).

[68] L. Salasnich, A. Parola, and L. Reatto, Phys. Rev. A **66**, 043603 (2002).

[69] N. G. Parker, S. L. Cornish, C. S. Adams, and A. M. Martin, J. Phys. B **40**, 3127 (2007).

[70] B. Eiermann, T. Anker, M. Albiez, M. Taglieber, P. Treutlein, K.-P. Marzlin, and M. K. Oberthaler, Phys. Rev. Lett. **92**, 230401 (2004).

[71] S. Becker, C.and Stellmer, S. Soltan-Panahi, P.and Dörscher, M. Baumert, E. Richter, K. Kronjäger, J.and Bongs, and K. Sengstock, Nat. Phys. **4**, 496 (2008).

[72] N. G. Parker, A. M. Martin, S. L. Cornish, and C. s. Adams, J. Phys. B: At., Mol. and Opt. Phys. **41**, 045303 (2008).

[73] T. P. Billam, S. L. Cornish, and S. A. Gardiner, Phys. Rev. A **83**, 041602(R) (2011).

[74] K. E. Strecker, G. B. Partridge, A. G. Truscott, and R. G. Hulet, New. J. Phys. **5**, 73 (2003).

[75] K. E. Strecker, G. B. Partridge, A. G. Truscott, and R. G. Hulet, Nature **417**, 150 (2002).

[76] L. Khaykovich, F. Schreck, G. Ferrari, T. Bourdel, J. Cubizolles, L. D. Carr, Y. Castin, and C. Salomon, Science **296**, 1290 (2002), https://science.sciencemag.org/content/296/5571/1290.full.pdf .

[77] S. Lepoutre, L. Fouché, A. Boissé, G. Berthet, G. Salomon, A. Aspect, and T. Bourdel, Phys. Rev. A **94**, 053626 (2016).

[78] S. L. Cornish, S. T. Thompson, and C. E. Wieman, Phys. Rev. Lett. **96**, 170401 (2006).

[79] G. D. McDonald, C. C. N. Kuhn, K. S. Hardman, S. Bennets, P. J. Everitt, P. A. Altin, J. E. Debs, J. D. Close, and N. P. Robins, Phys. Rev. Lett. **113**, 013002 (2014).

[80] O. J. Wales, A. Rakonjac, T. P. Billam, J. L. Helm, S. A. Gardiner, and S. L. Cornish, Comm. Phys. **3**, 51 (2020).

[81] T. Mežnaršič, T. Arh, J. Brence, J. Pišljar, K. Gosar, i. c. Gosar, R. Žitko, E. Zupanič, and P. Jeglič, Phys. Rev. A **99**, 033625 (2019).

[82] A. D. Bandrauk and H. Shen, J. Phys. A: Math. Gen. **27**, 7147 (1994).

[83] J. Javanainen and J. Ruostekoski, J. Phys. A: Math. Gen. **39**, L179 (2006).

[84] J. Helm, S. Rooney, C. Weiss, and S. A. Gardiner, Phys. Rev. A **89**, 033610 (2014).

[85] J. Holmer, J. Marzuola, and M. Zworski, Commun. Math. Phys. **274**, 187 (2007).

[86] S. C. Li and F. Q. Dou, Europhys. Lett. **111**, 30005 (2015).

[87] M. O. D. Alotaibi and L. D. Carr, arXiv e-prints , arXiv:1804.10339 (2018), arXiv:1804.10339 [cond-mat.quant-gas] .

[88] C. M. Savage and J. Ruostekoski, Phys. Rev. Lett. **91**, 010403 (2003).

[89] Y. S. Kivshar and G. P. Agrawal, *Optical Solitons* (Academic Press, San Diego, 2003).

[90] Q. H. Park and H. J. Shin, Phys. Rev. E **59**, 2373 (1999).

[91] X. B. Wang and B. Han, Journal of the Physical Society of Japan **89**, 124003 (2020).

[92] J. Sanz, A. Frölian, C. S. Chisholm, C. R. Cabrera, and L. Tarruell, "Interaction control and bright solitons in coherently-coupled Bose-Einstein condensates," (2019), arXiv:1912.06041 [cond-mat.quant-gas] .

[93] S. K. Adhikari, Phys. Rev. A **73**, 043619 (2006).

[94] S. K. Adhikari and L. Salasnich, Phys. Rev. A **76**, 023612 (2007).

[95] A. L. Marchant, T. P. Billam, T. P. Wiles, M. M. H. Yu, S. A. Gardiner, and S. L. Cornish, Nat. Comm. **4**, 1865 (2013).

[96] J. L. Roberts, N. R. Claussen, J. P. Burke, C. H. Greene, E. A. Cornell, and C. E. Wieman, Phys. Rev. Lett. **81**, 5109 (1998).

[97] C. L. Blackley, C. R. Le Sueur, J. M. Hutson, D. J. McCarron, M. P. Köppinger, H. W. Cho, D. L. Jenkin, and S. L. Cornish, Phys. Rev. A **87**, 033611 (2013).

[98] M. Höfer, L. Riegger, F. Scazza, C. Hofrichter, D. R. Fernandes, M. M. Parish, J. Levinsen, I. Bloch, and S. Fölling, Phys. Rev. Lett. **115**, 265302 (2015).

[99] S. B. Papp, J. M. Pino, and C. E. Wieman, Phys. Rev. Lett. **101**, 040402 (2008).

[100] S. Tojo, Y. Taguchi, Y. Masuyama, T. Hayashi, H. Saito, and T. Hirano, Phys. Rev. A **82**, 033609 (2010).

[101] M. Theis, G. Thalhammer, K. Winkler, M. Hellwig, G. Ruff, R. Grimm, and J. H. Denschlag, Phys. Rev. Lett. **93**, 123001 (2004).

[102] F. K. Fatemi, K. M. Jones, and P. D. Lett, Phys. Rev. Lett. **85**, 4462 (2000).

[103] D. M. Bauer, M. Lettner, C. Vo, G. Rempe, and S. Dürr, Nat. Phys. **5**, 339 (2009).

[104] Y. S. Kivshar and B. A. Malomed, Rev. Mod. Phys **61**, 763 (1989).

[105] H. Sakaguchi and B. A. Malomed, New J. Phys. **18**, 025020 (2016).

[106] O. V. Marchukov, B. A. Malomed, V. A. Yurovsky, M. Olshanii, V. Dunjko, and R. G. Hulet, Phys. Rev. A **99**, 063623 (2019).

[107] M. Yan, B. J. DeSalvo, B. Ramachandran, H. Pu, and T. C. Killian, Phys. Rev. Lett. **110**, 123201 (2013).

[108] A. Bandrauk and H. Shen, J. Phys. A **27**, 7147 (1994).

[109] J. Javanainen and J. Ruostekoski, J. Phys. A **39**, L179 (2006).

[110] N. Veretenov, Y. Rozhdestvensky, N. Rosanov, V. Smirnov, and S. Federov, Eur. Phys. J. D. **42**, 455 (2007).

[111] F. K. Abdullaev and V. A. Brazhnyi, J. Phys. B: At. Mol. Opt. Phys. **45**, 085301 (2012).

[112] B. Gertjerenken and C. Weiss, J. Phys. B: At. Mol. Opt. Phys. **45**, 165301 (1012).

[113] A. D. Martin and J. Ruostekoski, New J. Phys. **14**, 043040 (2012).

[114] J. L. Helm, T. P. Billam, and S. A. Gardiner, Phys. Rev. A **85**, 053621 (2012).

[115] Y. Kageyama and H. Sakaguchi, J. Phys. Soc. Japan **81**, 033001 (2012).

[116] B. Gertjerenken, Phys. Rev. A **88**, 053623 (2012).

[117] J. Polo and V. Ahufinger, Phys. Rev. A **88**, 053628 (2013).

[118] J. Helm, S. L. Cornish, and S. A. Gardiner, Phys. Rev. Lett. **114**, 134101 (2015).

[119] J. Satsuma and N. Yajima, Suppl. Progr. Theor. Phys. **55**, 284 (1974).

[120] A. Sacchetti, J. Comput. Phys. **227**, 1483 (2007).

[121] M. Łącki, M. A. Baranov, H. Pichler, and P. Zoller, Phys. Rev. Lett. **117**, 233001 (2016).

[122] F. Jendrzejewski, S. Eckel, T. G. Tiecke, G. Juzeliūnas, G. K. Campbell, L. Jiang, and A. V. Gorshkov, Phys. Rev. A **94**, 063422 (2016).

[123] W. Ge and M. S. Zubairy, Phys. Rev. A **101**, 023403 (2020).

[124] S. Subhankar, P. Bienias, P. Titum, T.-C. Tsui, Y. Wang, A. V. Gorshkov, S. L. Rolston, and J. V. Porto, New J. Phys. **21**, 113058 (2019).

[125] P. Bienias, S. Subhankar, Y. Wang, T.-C. Tsui, F. Jendrzejewski, T. Tiecke, G. Juzeliūnas, L. Jiang, S. L. Rolston, J. V. Porto, and A. V. Gorshkov, Phys. Rev. A **102**, 013306 (2020).

[126] T.-C. Tsui, Y. Wang, S. Subhankar, J. V. Porto, and S. L. Rolston, Phys. Rev. A **101**, 041603 (2020).

[127] F. Wilczek and A. Zee, Phys. Rev. Lett. **52**, 2111 (1984).

[128] J. Ruseckas, G. Juzeliūnas, P. Öhberg, and M. Fleischhauer, Phys. Rev. Lett. **95**, 010404 (2005).

[129] B. A. Malomed and R. S. Tasgal, Phys. Rev. E **58**, 2564 (1998).

[130] R. Dum and M. Olshanii, Phys. Rev. Lett. **76**, 1788 (1996).

[131] P. A. Ruprecht, M. J. Holland, K. Burnett, and M. Edwards, Phys. Rev. A **51**, 4704 (1995).

[132] J. L. Roberts, N. R. Claussen, S. L. Cornish, E. A. Donley, E. A. Cornell, and C. E. Wieman, Phys. Rev. Lett. **86**, 4211 (2001).

[133] P. Virtanen, R. Gommers, T. E. Oliphant, M. Haberland, T. Reddy, D. Cournapeau, E. Burovski, P. Peterson, W. Weckesser, J. Bright, S. J. van der Walt, M. Brett, J. Wilson, K. J. Millman, N. Mayorov, A. R. J. Nelson, E. Jones, R. Kern, E. Larson, C. J. Carey, İ. Polat, Y. Feng, E. W. Moore, J. VanderPlas, D. Laxalde, J. Perktold, R. Cimrman, I. Henriksen, E. A. Quintero, C. R. Harris, A. M. Archibald, A. H. Ribeiro, F. Pedregosa, P. van Mulbregt, and SciPy 1.0 Contributors, Nature Methods **17**, 261 (2020).

[134] L. D. Carr and J. Brand, Phys. Rev. Lett. **92**, 040401 (2004).